

UNIVERSITA' DEGLI STUDI DI NAPOLI "FEDERICO II"



DEPARTMENT OF CHEMICAL, MATERIALS AND PRODUCTION  
ENGINEERING (DICMAPI)

PHD IN "INDUSTRIAL PRODUCT AND PROCESS ENGINEERING"  
XXXIII CYCLE

**"LAB ON CHIP FOR CELL SEPARATION "**

**Supervisor**

Ch.mo Prof. Filippo Causa

Ch.mo Prof. Paolo Antonio Netti

**Coordinator**

Ch.mo Prof. Andrea D'Anna

**PhD Student**

Mariarosaria Telesco

January 2018 - May 2021



## *Table of contents*

---

<b>Chapter 1 .....</b>	<b>6</b>
<b>Aim of work .....</b>	<b>6</b>
<b>1 Introduction .....</b>	<b>9</b>
<b>1.1 Cell separation technique .....</b>	<b>9</b>
1.1.1 Immunomagnetic cell separation .....	9
1.1.2 Fluorescence-activated cell sorting.....	9
1.1.3 Density gradient centrifugation.....	10
1.1.4 Immunodensity cell separation .....	10
1.1.5 Sedimentation.....	11
1.1.6 Adhesion .....	11
<b>1.2 Microfluidic device for cell separation .....</b>	<b>12</b>
<b>2 Theoretical background .....</b>	<b>14</b>
<b>2.1 Non-dimensional numbers.....</b>	<b>14</b>
<b>2.2 Flow-induced forces .....</b>	<b>15</b>
2.2.1 Inertial lift force .....	15
2.2.2 Elastic lift force .....	16
2.2.3 Dean Drag force .....	17
<b>2.3 Active microfluidic cell sorting systems .....</b>	<b>18</b>
2.3.1 Acoustic radiation force .....	18
2.3.2 Dielectrophoresis microfluidics .....	19
2.3.3 Magnetic microfluidics .....	20
2.3.4 Optical microfluidics.....	22
<b>2.4 Passive microfluidic system .....</b>	<b>22</b>
2.4.1 Inertial separation.....	23
2.4.2 Viscoelastic separation.....	30
2.4.3 Filtration.....	35
<b>2.4.3.1 Hydrodynamic filtration.....</b>	<b>35</b>

2.4.3.2	<b>Hydrophoretic filtration</b> .....	<b>36</b>
2.4.4	Deterministic lateral displacement.....	37
2.4.5	Trilobite.....	38
2.4.6	Transient cellular adhesion .....	40
2.4.7	Cellular immobilization .....	41
<b>3</b>	<b>Materials and methods</b> .....	<b>43</b>
<b>3.1</b>	<b>Design Principle</b> .....	<b>43</b>
<b>3.2</b>	<b>Device fabrication</b> .....	<b>48</b>
<b>3.3</b>	<b>Rheological analysis of suspending fluid</b> .....	<b>50</b>
<b>3.4</b>	<b>Preparation of the particle suspensions</b> .....	<b>52</b>
<b>3.5</b>	<b>Blood separation</b> .....	<b>53</b>
3.5.1	Peripheral blood mononuclear cell collection.....	53
3.5.2	Lymphocytes and monocytes collection .....	55
3.5.3	RBC and neutrophils collection .....	56
<b>3.6</b>	<b>Preparation of the blood cell suspensions</b> .....	<b>57</b>
<b>3.7</b>	<b>Other cell lines</b> .....	<b>57</b>
<b>3.8</b>	<b>Brightfield microscopy observations</b> .....	<b>58</b>
<b>3.9</b>	<b>Experimental setup and data analysis</b> .....	<b>60</b>
<b>3.10</b>	<b>Droplet generation</b> .....	<b>63</b>
3.10.1	Materials.....	63
3.10.2	Synthesis of hydrogel.....	64
3.10.3	Rheological characterization.....	65
3.10.4	Synthesis of functionalized microparticles .....	66
3.10.5	Flow data collection and analysis .....	68
3.10.6	Network properties of PA particles.....	68
3.10.7	Swelling characterization .....	70
<b>3.11</b>	<b>Holografy</b> .....	<b>70</b>
<b>4</b>	<b>Results</b> .....	<b>72</b>
<b>4.1</b>	<b>Device calibration and fluid flow testing</b> .....	<b>73</b>
<b>4.2</b>	<b>Glycerol Measurement</b> .....	<b>82</b>

<b>4.3</b>	<b>Particle investigation in channel C .....</b>	<b>84</b>
<b>4.4</b>	<b>Hydrogel Characterization.....</b>	<b>85</b>
<b>4.5</b>	<b>Swelling characterization.....</b>	<b>87</b>
<b>4.6</b>	<b>Rheological properties of hydrogel.....</b>	<b>89</b>
<b>4.7</b>	<b>Hydrogel investigation channel C and D.....</b>	<b>90</b>
<b>4.8</b>	<b>Cell separation .....</b>	<b>92</b>
<b>4.9</b>	<b>AR analysis of cell lines.....</b>	<b>97</b>
<b>4.10</b>	<b>Peripheral blood cell investigations .....</b>	<b>100</b>
<b>4.11</b>	<b>Digital holography microscope outcomes .....</b>	<b>103</b>
<b>5</b>	<b>Conclusions and future perspectives.....</b>	<b>106</b>
	<b>Supplementary materials .....</b>	<b>110</b>
	<b>Reference.....</b>	<b>115</b>



# *Chapter 1*

## *Aim of work*

Cells are the basic functional units of human life, which led researcher in molecular biology, biochemistry, and biotechnology focus their skills to obtain efficient and cost-effective methods for cell enrichment, isolation, and handling. For instance, the main problem of biochemical, pharmaceutical, and clinical studies is the requirement of homogenous cell populations, which consist of a single cell type. Unfortunately, many real-life cell samples are highly heterogeneous (in structure, function, and characteristics) or at the other hand consist of a low concentration of the searched for target cells. In particular, in many cancer and prenatal diagnosis applications the development of specific cell separation tools is required.[1], [2] The more stringent the requirements for a specific and precise cell separation, the higher the degree of accuracy and reproducibility which will be required in the technology that underlies the separation method.[3], [4]

In general, many bio-physical or -chemical cell characteristics can be used for cell sorting, such as size, shape, density, and arrays of surface molecules. For example, red blood cells (RBCs) (cell employed to deliver the oxygen to the tissues) (relatively small, (6-8  $\mu\text{m}$  in diameter), and flexible, with the highest density of any cell type in our blood) can be separate from white blood cells (WBCs). Instead, in the case of the sickle-cell disease, a genetic blood disorder triggers the RBCs to assume an abnormal, rigid, sickle shape.

Cancer is a another well-known example of such biophysical cell changes.[5] Benign tumor cells grow slowly, in contrast, malignant tumor cells grow rapidly [6] and have an irregular shape compared to benign cells. [7], [8] In general, cancer is detected and diagnosed based on bio-physical changes present in tissues and cells. For instance, nuclear changes such as an increase in size, deformation or change of the

internal organization are among the most universal criteria for detecting malignancy. [9], [10]

Despite great successes in the last decade, cell sorting performance remain challenging and therefore an active area of research. In addition to sensitivity and specificity requirements, an ideal sorting technique should not be labour intensive, should be automated and quantitative, the results should predict clinical outcomes, and help the physician personalize therapeutic options.

For instance, microfluidic technologies are a group of techniques and processes that use devices to precisely control and manipulate fluid in geometrically small channels (sub- to few hundred- micrometres in size). The developing of device with biological utility requires the integration of knowledge from the fields of engineering, biology, physics, and chemistry. Such microfabricated devices are used to study biological systems and to generate new insights into how these systems work. Conversely, the biological knowledge gained through micro/nano-scale analyses can lead to further improvements in device design. In general, they possess several advantages such as increased efficiency, portability, environmental compatibility at a reduced cost of samples and operation and better overall process control, as well as the capability to integrate multiple steps and to achieve massive parallelization on-chip. However, most of these devices (employed for cell separation) have been tested with only particles suspended in aqueous buffer solutions that are Newtonian fluids presenting a constant viscosity. As a matter of fact, many of the real chemical (e.g., colloidal suspensions and polymer solutions) [9,10] and biological (e.g., blood, saliva and DNA solutions) [11], [12] samples exhibit non-Newtonian characteristics such as shear thinning and viscoelasticity. [13], [14] Hence, there has recently been a growing interest in the fundamental and application studies of microfluidic particle manipulations in non-Newtonian fluids. [15], [16]

For these reasons, the aim of this work is to develop a microfluidic platform to study the influence of fluid, particle, and cell properties on the separation efficiency. To obtain that, we have designed, fabricated, and tested a novel microfluidic device, that

exploit the effect of viscoelastic fluid properties on biophysical cell properties to separate different cell types in-flow. To achieve cell-size separation, First, we calibrate our microfluidic platform using polystyrene latex particles with different dimensions (diameter of 7, 10, 15 and 20  $\mu\text{m}$ ). Subsequently, we produced, characterized, and tested in our microfluidic device hydrogel particles with different deformability rates. In addition, we applied our findings on cell lines of healthy, invasive and highly invasive tumour cells as well as with different types of peripheral human blood cells. Final tests on mixed cell sample show the performance of our resented microfluidic platform.

Up to now, the most part of microfluidic studies are based on the difference of particle size, while comparatively little on separation of particles based on shape or deformability can be found in literature, especially for viscoelastic fluids. We hope that this work will bring deeper inside in cell separation phenomena and be a starting point for further investigations.

# ***1 Introduction***

## ***1.1 Cell separation technique***

Cell separation is a process to detach one or more specific cell types from a sample with heterogeneous mixture of cells. Several methods can be used for cell isolation, such as: immunomagnetic cell separation[17], fluorescence-activated cell sorting [18], density gradient centrifugation[19], immunodensity cell separation[20], sedimentation [21], adhesion [22], microfluidic cell separation[23] and other techniques. A cell separation method should be chosen according to the cell line that should be isolated and the existing equipment and knowhow.

### ***1.1.1 Immunomagnetic cell separation***

For instance, the immunomagnetic cell separation[17] is a technique that use magnetic particles to isolate target cells from heterogeneous mixture. Here the target cells are bound to magnetic particles by specific cell surface proteins via antibodies, enzymes, lectins, or streptavidin. Then an electromagnetic field can be applied to the sample, so the labelled cells move towards the wall of a falcon tube for example, while the unlabelled cells remain in the supernatant creating a physical separation within the sample.

### ***1.1.2 Fluorescence-activated cell sorting***

Fluorescence-activated cell sorting [18](FACS) method utilizes flow cytometry and fluorescent probes to sort heterogeneous mixtures of cells. Target cells are bound to fluorophore-tagged antibodies using specific antigens. After labelling,

the flow cytometer converges the cells into a uniform stream of single cells. Then, a set of lasers is used to excite the cell-bound fluorophores, causing fluorescent emissions. Based on the specific wavelength produced by each passing cell, target cell will be deflected into collection tubes or fall into the waste chamber.

### ***1.1.3 Density gradient centrifugation***

Another cell isolation techniques is based on density gradient centrifugation [19], which depends on the varying densities of biophysical cell properties. In general, such ans technique uses a density gradient medium in which each cell type will sediment in function of its intrinsic density. Briefly, the sample is layered on top of a density gradient medium before being centrifuged. There are many different types of density medium, which can be chosen according to the biophysical properties of the target cell type that, which should be isolated.

### ***1.1.4 Immunodensity cell separation***

Another way for cell isolation is the immunodensity cell separation[17], which is a negative selection method that uses a mixture of antibody-based labelling and density gradient centrifugation. For instance, antibodies are added to a whole blood sample, labelling the unwanted cells, and cross-link them. These aggregates are much denser than non-linked cells allowing to isolate them by centrifugation using a density gradient medium, where the unwanted cells pellet, leaving the target cells in suspension.

### ***1.1.5 Sedimentation***

For the sedimentation[21] technique, gravity causes cell separation, which can be larger for more denser components than cells or particles that are smaller or less dense. For example, after centrifugation with a low force, the largest and densest components in a heterogeneous cell sample can be collected in a pellet due to their higher rate of sedimentation. The supernatant can then be centrifuged again to isolate further elements.

### ***1.1.6 Adhesion***

Furthermore, the unique characteristics of different cell types can be used to split target cells from heterogeneous populations. By choosing suitable growth factors and cell culture plates to selectively favour or inhibit adhesion. For instance, adherent cells can be separated from cells in suspension. Another example are Macrophages, which can be isolated from the whole blood by adhesion[22]. Otherwise, suspended cells can be isolated through culturing the heterogeneous cell population in plates with an ultra-low attachment. Without a surface to adhere to, adherent cells will fail to survive, and the target cells will remain in the suspension.

However, all these techniques for cell sorting present several significant and persistent limitations including limited sample throughput and processing speeds that would make processing clinical-scale samples (>500 million cells) unfeasible, loss of functionality or viability caused by the operating pressures, bulky equipment, and technical expertise necessary for using complex machinery, and increased risk of sample contamination and safety. These limitations must be overcome to permit more efficacy clinical application and

commercialization. Microfluidic cell separation is a new category of cell isolation methods that was born to overcome all these limitations. It uses microfluidic chips that are commonly known as "lab-on-a-chip" devices. These devices have several advantages, including: the smaller volumes of samples and reagents required for use (i) faster sorting rates, (ii) equal or improved accuracies, (iii) ability to process native biological fluids, (iv) ability to process diverse cell types, (v) enhanced capabilities for multiplexed sorting, (vi) simpler operating procedures enabling fully automated systems, (vii) reduced cost, and (viii) reduced size for operational convenience and portability. In general, microfluidic devices can be divided into active and passive systems. Such systems can use external fields (e.g., acoustic, electric, magnetic, or optical) to impose forces which can displace cells for sorting applications and are called active sorting systems, whereas passive systems mostly use inertial and viscoelastic forces, filters, and adhesion mechanisms to separate cell types. These methods can also be classified by the presence or absence of cell labelling; although some methods utilize labelling cells with antibodies, most methods are known for being label-free. Microfluidic devices are a proven technology for cellular handling as they can offer precise spatial and temporal control in a greatly miniaturized platform. These devices can be easily microfabricated, with a lower cost and simplified commercialization. In addition, microfluidics can be used to detect, focus, mix, count, lyse, and analyse individual cells on an integrated platform for complete lab-on-a-chip applications.

## ***1.2 Microfluidic device for cell separation***

Microfluidic devices have been widely used in the past for manipulations of particles (beads, cells, vesicles, drops, etc.) such as focusing [24], trapping/concentration [25]

[26] and separation [27] in different biomedical applications. such a manipulation can be based on the differences in the intrinsic, physical, and/or biochemical properties of various cell types. In particular, cell properties such as size, morphology, shape, deformability, magnetic properties, electrical properties, and compressibility can be used to design a robust, accurate, and high-throughput microfluidic platform for selective isolation of cells [28]. Furthermore, microfluidic platforms offer various advantages and greater control over cell size distribution compared with conventional cell separation methods such as filtration, density gradient separation, and adhesion-based methods. Therefore, this technology paves the way to the development of cost-effective, portable microscale separation devices for both point-of-care and point-of-need clinical diagnostics.

## 2 Theoretical background

### 2.1 Non-dimensional numbers

The motion of particles in microchannel is often characterized by the following dimensionless numbers. In general, the inertial effect on fluid and particle motions is measured by the (channel) Reynolds number,  $Re$ , and the particle Reynolds number,  $Re_p$ .

$$Re = \frac{\rho D_h v}{\mu} \quad Eq. 2.1-1$$

$$Re_p = \beta^2 Re \quad Eq. 2.1-2$$

$$\beta = \frac{a}{D_h} \quad Eq. 2.1-3$$

where  $\rho$  is the fluid density,  $v$  is the average fluid velocity,  $a$  is the particle diameter,  $D_h$  is the channel's hydraulic diameter,  $\mu$  is the zero-shear viscosity of fluid, and  $\beta$  is the dimensionless particle blockage ratio given by ratio of particle diameter and  $D_h$ . On the contrary, the viscoelastic effect on fluid and particle motions is measured by the Weissenberg number,  $Wi$ , which compares the elastic force to viscous force,

$$Wi = \lambda \dot{\gamma} = \lambda \frac{2v}{D_h} \quad Eq. 2.1-4$$

where  $\lambda$  is the relaxation time of the fluid and  $\dot{\gamma}=2v/D_h$  the average fluid shear rate over the channel cross-section. Another often used dimensionless number for viscoelastic effect is the Deborah number,  $De$ , which is defined as the ratio of the fluid relaxation time to the characteristic time of an experimental observation,  $t_p$  [15,16], i.e.,

$$De = \frac{\lambda}{t_p} \quad Eq. 2.1-5$$

These two non-dimensional numbers are of the same order in magnitude and sometimes considered interchangeable in the literature [66]. In addition, the viscoelastic effect can also be characterized by the elasticity number,  $El$ , which is

the ratio of the Weissenberg number (or Deborah number) to Reynolds number, or equivalently the ratio of the elastic force to inertial force, and hence independent of flow kinematics,

$$El = \frac{Wi}{Re} = \frac{2\lambda\mu}{\rho D_h} \quad \text{Eq. 2.1-6}$$

## 2.2 Flow-induced forces

In fluid flow in a channel with particles, many forces are presents due to the action of shear stress and pressure on particle surface. In the paragraphs 2.2.1, 2.2.2, 2.2.3 we explained principal forces present in a particles flow.

### 2.2.1 Inertial lift force

The inertial lift force can be separated in two components. The wall-induced inertial lift,  $F_{iL,w}$ , is a result of vorticity around a near-wall particle, which increases the fluid pressure in the particle-wall gap pushing the particle away from the wall. Consequently it decreases when particle goes away from wall [13, 14]. On the other side, the shear gradient induced inertial lift,  $F_{iL,s}$ , is a result of the shear rate, which directs a particle away from the channel centre and increases from zero at the channel centre (Fig. 1) [31]. The dominant inertial lift  $F_{iL}$  (given by sum of this forces) scales as: [16–18].

$$F_{iL} = F_{iL,w} + F_{iL,s} = C_{il}\rho a^4 \dot{\gamma}^2 \quad \text{Eq. 2.2-1}$$

Where the non-dimensional inertial lift coefficient,  $C_{il}$ , is a function of the normalized particle position over the channel cross-section and  $Re$ , where  $\rho$  is the density of fluid and  $\dot{\gamma}$  is the average fluid shear rate over the channel cross-section. In general, the effect of  $F_{iL}$  is only present when the particle  $Re$  is about 1 [21–25]. For instance, the scaling of  $F_{iL}$  for a particle near the wall or the centreline of a straight square microchannel is studied from Di carlo *et al.* [74]. Indeed, Liu *et al.* [75] have proposed fitting formulae to the direct numerical simulation (DNS) data

of Eq. 1.3-7 for spheres in straight rectangular microchannels [79]. Other weaker inertial lift forces that are less studied in the literature include the rotation-induced Magnus force and the slip-induced Saffman force [76–78]. They are usually much smaller than the dominant inertial lift,  $F_{iL}$ , for this reason in our work we do not take them under consideration.

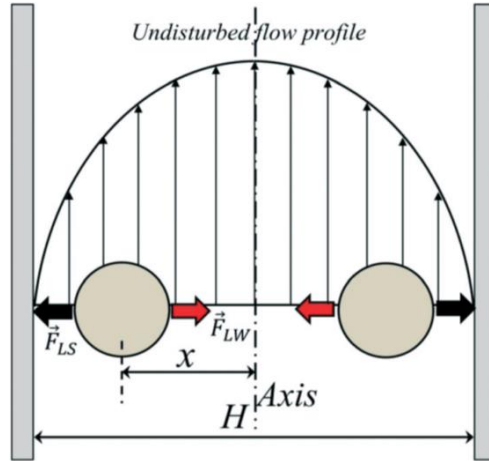


*Fig. 1 Schematic Illustration of inertial forces in a microfluidic channel with  $Re \approx 1$ . Reproduced from ref.31.*

### 2.2.2 Elastic lift force

In general, a viscoelastic fluid generates on a particle and elastic lift force due to non-uniform normal stress differences [80,81]. The first normal stress difference,  $N_1 = \tau_{11} - \tau_{22}$ , generates an extra tension along fluid streamlines in the translational direction of flow [55]. the second normal stress difference,  $N_2 = \tau_{22} - \tau_{33}$ , creates a secondary flow over the channel cross-section [82], in the velocity gradient direction and rotational direction of flow. For most viscoelastic polymer solutions, the magnitude of  $N_2$  is much smaller than that of  $N_1$  [83,84], To evaluate  $N_1$  [60], we use the Oldroyd-B model as a constitutive equation:

$$N_1 = -2\eta_p \lambda \dot{\gamma}^2 \tag{Eq. 2.2-2}$$

where  $\eta_p$  is the polymeric contribution to the solution viscosity.  $N_1$ , becomes smallest at the centre in the cylindrical channel while at both the center and the four

corners in the square-shaped channel. When the magnitude of  $N_2$  is negligible as compared to that of  $N_1$ , the lateral flow-induced elastic lift,  $F_{eL}$ , which can be assumed solely proportional to the variation of  $N_1$  over the size of a particle [87,88], i.e.,

$$F_{eL} = C_{eL} a^3 \nabla N_1 = -2C_{eL} a^3 \eta_p \lambda \nabla \dot{\gamma}^2 \quad \text{Eq. 2.2-3}$$

where  $C_{eL}$  is the non-dimensional elastic lift coefficient, and  $F_{eL}$  points toward the region with a smaller shear rate.  $F_{eL}$  alone drives the particle toward the centreline in the cylindrical channel or both the centreline and the four corners in the square one (Fig. 2) [35].

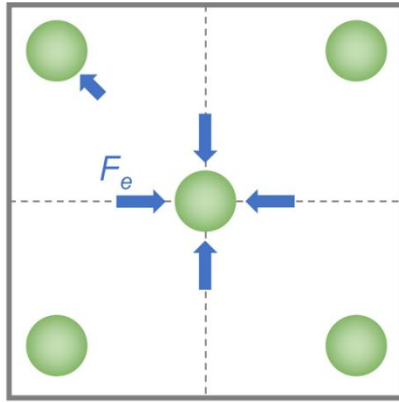


**Fig. 2** Schematic Illustration of viscoelastic forces in a microfluidic channel with  $Re \ll 1$  and  $Wi > 0$ . Reproduced from ref.35.

### 2.2.3 Dean Drag force

Drag force arises from the secondary fluid flow in the channel cross section. The secondary fluid flow can be induced by either the streamline curvature [89] or  $N_2$  of the fluid [82]. In curving channels and straight channels with expansions and contractions, fluid inertia produces counter-rotating vortices in the channel cross section (Dean flow) (Fig. 3) [90]. In general, Dean number,  $D_n$  characterize the strength of this flow:

$$D_n = Re \sqrt{\frac{D_h}{2R}} \quad \text{Eq. 2.2-4}$$

where  $R$  is the radius of curvature of the path of the channel. In addition, the non-zero  $N_2$  in a strongly elastic fluid (e.g., polyacrylic acid PAA solution) has been demonstrated to cause a rotational secondary fluid flow in the cross section of even a straight microchannel [64,82,36].

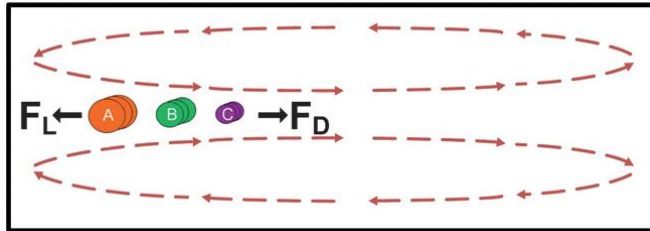


**Fig. 3** Schematic Illustration of Dean drag forces in a microfluidic channel with  $Re \approx 1$ . Reproduced from ref. [36].

## 2.3 Active microfluidic cell sorting systems

As already mentioned, the selection of an appropriate microfluidic technique is crucial to recover specific cell types. Therefore, various microfluidic active techniques were developed such as acoustic microfluidics (a mode of separation based on acoustic radiation force), dielectrophoretic microfluidics (based on inhomogeneous electric field), magnetic microfluidics (based on intrinsic magnetic property) and optical microfluidics (in which light is used to manipulate and separate particles), for cell separation and sorting.

### 2.3.1 Acoustic radiation force

Sorting of particles using acoustic radiation force (ARF) has been demonstrated based on differences in the speed of sound and the mass density between particles and the surrounding fluid [19, 20]. For example, a particle that is stiffer and denser than the suspending medium (i.e., positive acoustic contrast factor) will migrate to

the nearest pressure node in a standing wave, while one that has a negative acoustic contrast factor will be trapped at the pressure antinode. Shi *et al.* used a central sheath flow and two lateral inlet and separate particles in function of their size (see Fig. 4). This technique induced larger axial acoustic forces on the particles of larger volume, repositioning them closer to the wave pressure node at the centre of the channel. [39]

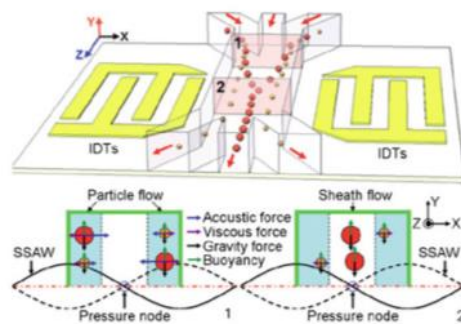


**Fig. 4** Schematic of the separation mechanism showing particles beginning to translate from the sidewall to the centre of the channel due to axial acoustic forces applied to the particles when they enter the working region of the SSAW (site 1). The differing acoustic forces cause differing displacements, repositioning larger particles closer to the channel centre and smaller particles farther from the centre (site 2). Reproduced from ref.37

This leads to particles of different types collecting in different stable locations. Therefore, particle sorting based on size can be achievable using ARFs, but typically all polystyrene particles (PS) with a higher density and stiffness than the suspended medium moves towards the pressure nodes. Hence, to achieve sorting in this case, it is necessary to stop the manipulation prior to all particles arriving at the node; in this way, sorting can be achieved based on the speed of migration towards the node [40].

### 2.3.2 Dielectrophoresis microfluidics

Another active sorting technique is the dielectrophoresis (DEP). The term coined by Pohl *et al.* [41], is the motion of an object under forces resulting from electric field gradients. The applications of DEP are based on differentiation of dielectric and conducting properties of objects to allow their separation and identification. DEP has

been demonstrated to be useful for separating polydisperse particle suspensions into homogeneous subpopulations, manipulating and concentrating biologically relevant molecules, distinguishing dead and living cells or ill and healthy cells, assembling carbon nanotubes, etc. [42], [43]. Holmes *et al.* constructed a microfluidic device (see Fig. 5) with two consecutive arrays of microelectrodes, one to focus the particles into a sheet and the second to separate them using a combination of positive (the particle moves in the direction of increasing electric field) and negative (particle moves away from the increasing electric field) DEP [42].

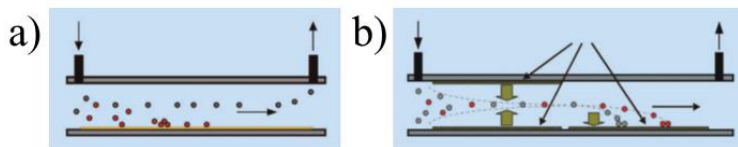


**Fig. 5** Schematic diagram of one mechanism of dielectrophoretic separation over a long array of interdigitated electrodes. Particles flow through the device, some collecting on the electrodes through positive DEP, while others are repelled into the middle of the channel and are removed by the fluid flow. b). Schematic diagram of the dielectrophoretic separator. The first section of the device has two interdigitated electrode arrays at top and bottom of the channel, which focus the particles into the centre of the channel by negative DEP. The second section contains a single electrode array, which differentially pulls the focused particles from the fluid flow by positive DEP, separating them into distinct bands. Reproduced from ref.40.

Moreover, undesired effects like electro-convection and Joule heating can be suppressed in tiny microfluidic devices.

### 2.3.3 Magnetic microfluidics

The main objective of magnetic microfluidic separation is to attract or repel particles or cells from their regular trajectory in a fluid flow, and to guide them to a specific outlet for collection using a magnetic force. The main challenge in designing a microfluidic device for this purpose is achieving both high efficiency and throughput [44]. Han *et al.* recently showed the continuous separation of RBCs in a microfluidic device by passing whole blood (see Fig. 6). The researchers observed that RBCs were concentrated into the high magnetic flux regions after 20 min.

Remarkably this effect was observed using whole blood that had not been reduced to its deoxygenated, paramagnetic state [45].

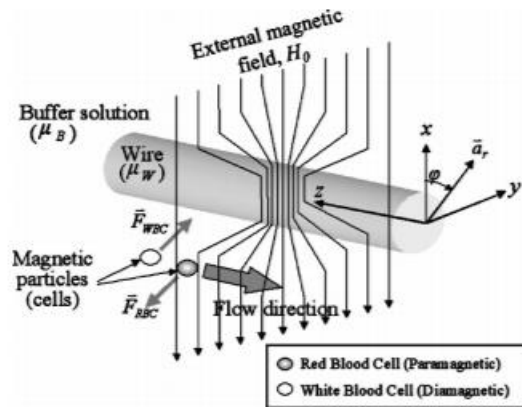


**Fig. 6** Cylindrical coordinates of a magnetic particle with respect to a circular ferromagnetic wire in a uniform external magnetic flux. Reproduced from ref.43.

Castillo-Torres *et al.* developed a microfluidic magnetic separation ( $\mu$ FMS) device (see Fig. 7) capable detects bacterial targets of interest (using 1.5- $\mu$ m-diameter magnetic microdisc), such as Escherichia coli, in drinking and recreational water quality monitoring. This system is able to filter 100 mL samples in less than 15 min [46].

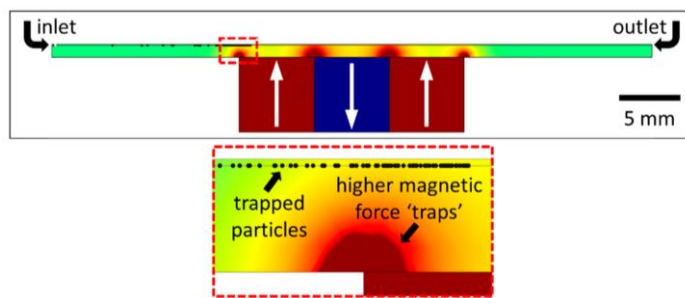


**Fig. 7** COMSOL geometry used for simulations of the  $\mu$ FMS device, isolating ‘microdisc’ particles. Reproduced from ref.44

Various techniques have been applied to improve the magnitude of magnetic force relative to other forces.

### 2.3.4 Optical microfluidics

Light has been used to manipulate and separate particles depending on their optical polarizability, a microfluidic optical technique that has been widely used for the popular optical trapping method. For sorting, demonstration of this technique using interferometric patterns of light for separations based on size (protein microcapsules) and refractive index (separating polymer from silica spheres) has been accomplished (see **Fig. 8**) [47]. MacDonald *et al.* demonstrate an optical sorter for microscopic particles that exploits the interaction of particles biological or otherwise with a three-dimensional optical lattice. The strength of this interaction with the lattice sites depends on the optical polarizability of the particles, giving tuneable selection criteria. They demonstrate both sorting by size (of protein microcapsule drug delivery agents) and sorting by refractive index (of other colloidal particle streams).

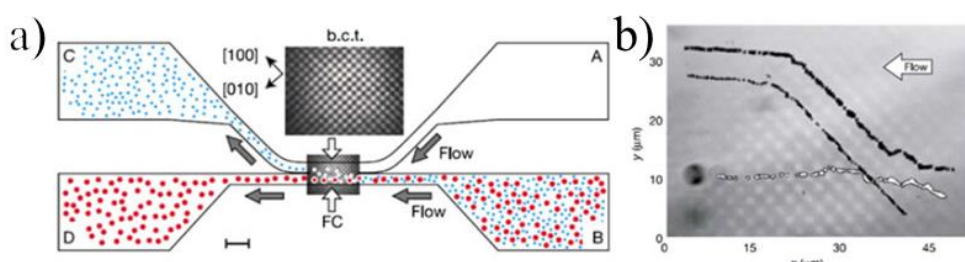


**Fig. 8** a) The particle mixture introduced through chamber B passes through a 3D optical lattice in the fractionation chamber (FC) where strong optical interactions selectively generate separate flow paths. b) Separation of 2  $\mu\text{m}$  (black crosses) and 4  $\mu\text{m}$  (white crosses) diameter capsules in an optical lattice. Reproduced from ref.45

## 2.4 Passive microfluidic system

Passive systems consist of a variety of methods that do not rely on external forces to separate cells. Instead, these methods rely on the inherent differences in cellular morphology (biophysical properties) between cell groups (e.g., size, shape, compressibility, and density) and can sort cells using inertial and viscoelastic forces,

hydrodynamic spreading, deterministic lateral displacement, filtration, transient cellular adhesion, and cellular immobilization[48].

### 2.4.1 Inertial separation

Inertial separation is based on the properties of a Newtonian fluid to generate a lateral migration perpendicular to the main flow direction, when the Re is to the order of 1 [33]. When  $Re \ll 1$ , The dominant force is that viscous one and particles follow the fluid streamlines. When Re is above 1, inertial lift forces become dominant, and particles migrate across the fluid streamlines [49].

In function of different geometry, the equilibrium positions of particles are different (see **Fig. 9**) [50].

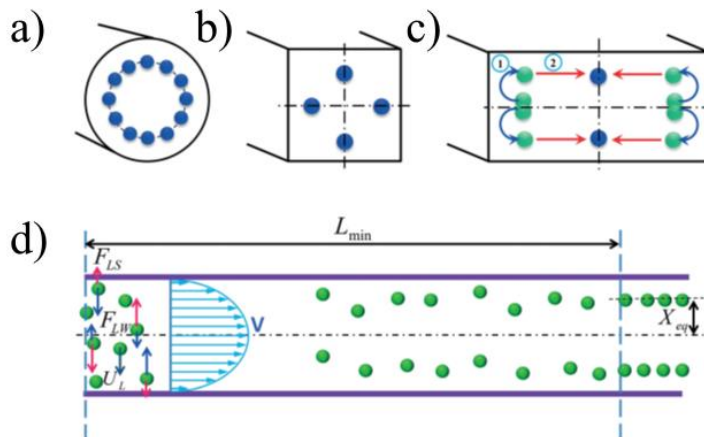


**Fig. 9** Inertial equilibrium positions in a straight channel with different cross sections: a) circular cross section; b) square cross section, and c) rectangular cross section with low aspect ratio ( $\approx 0.5$ ). (d) The lateral migration speed  $UL$  and minimum channel length for particle focusing  $L_{min}$ .. Respectively adapted with permission from Ref. [48]

#### 2.4.1.1 Straight channel

In a straight channel with a circular cross section, the randomly distributed particles migrate laterally to a narrow annulus at about 0.6 times of the channel radius from the axis, [51], [52] as depicted in Fig. 6a. However, in a straight channel with a square

cross section ( $AR = H/W = 1$ ) particles normally focus to face the centre of each wall (see Fig. 6b [53]). In rectangular section ( $AR \approx 0.5$ ), the particle equilibrium positions are reduced to two, at the centre of long walls with a distance away about 0.2 times height from them (see Fig. 6c) [50], [54]. Inertial lift force (see *Eq. 2.1-1*) is affected on the diameter of particles so, larger particles migrate faster than smaller particles to reach equilibrium position in the channel. In addition, larger cells are closer to the channel centre, and smaller cells are closer to the channel walls. Based on different velocity to reach equilibrium position, Mach and Di Carlo [55] reported a parallelized microfluidic device to separate pathogenic bacteria from diluted blood (see Fig. 7b). Hur *et al.* [56] purify adrenal cortical progenitor from digestions of murine adrenal glands utilizing hydrodynamic inertial lift forces in a channel ( $W = 40$  mm,  $H = 90$  mm and  $L = 4.5$  cm, where  $L$  is the length of channel) (see Fig. 7a). Later, Zhou and colleagues [57] used a device with two stages (see Fig. 7c). In the first stage, randomly distributed particles focus on half of the channel height near two sidewalls. Then the channel expands and so the equilibrium flow positions is modified to the centre of the top and bottom walls. Smaller particles alter weakly their lateral position because low lift force, *vice-versa* larger particles migrate quickly at their equilibrium position. Zhou *et al.* reach an efficiency of 99% and a purity of 90%.

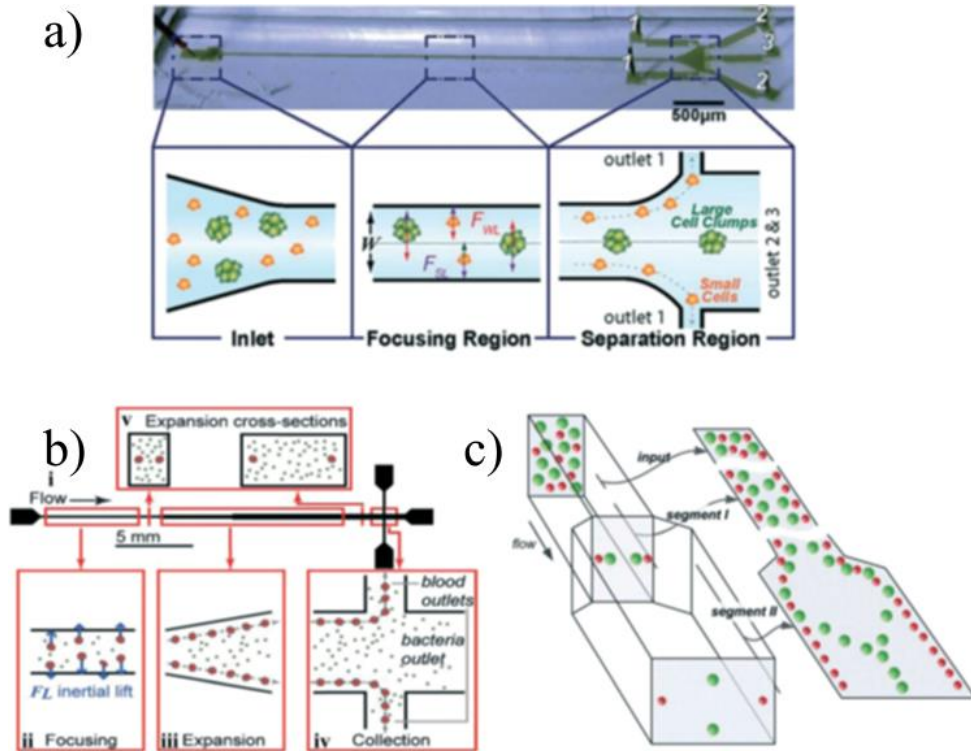


**Fig. 10** a). Label free isolation of adrenal cortical progenitor cells by size-based differential inertial focusing in a straight channel. Reproduced from ref.54. b). Separation of pathogenic bacteria from diluted blood in a series-connected straight channel which utilizes a unique differential transit time by size-dependent inertial lift forces. Reproduced from ref.53 c). Complete separation of particles in a cascaded channel with two straight segments with different aspect ratios (ARs). Reproduced from ref.55.

#### 2.4.1.2 Spiral channel

A secondary flow is a relatively minor flow perpendicular to the primary. The magnitude and form of generated secondary flow be controlled by the well-designed channel structure, such as spiral microchannel, contraction–expansion channel, micro-orifice microchannel or disturbance obstacle. A secondary flow is generated from different velocity in the central and near-wall regions. Indeed, at the curvature, there is a transverse pressure gradient, which provides the centripetal force for the fluid elements to change direction. The fluid elements near the channel centreline have a larger inertia and would tend to flow outward around a curve due to the centrifugal force, creating a pressure gradient in the radial direction within the

channel. In a fully bounded channel, due to the centrifugal pressure gradient, relatively stagnant fluid near the walls recirculates inward, finally forming two symmetric circulating vortices (see Fig. 8a,b) [58].

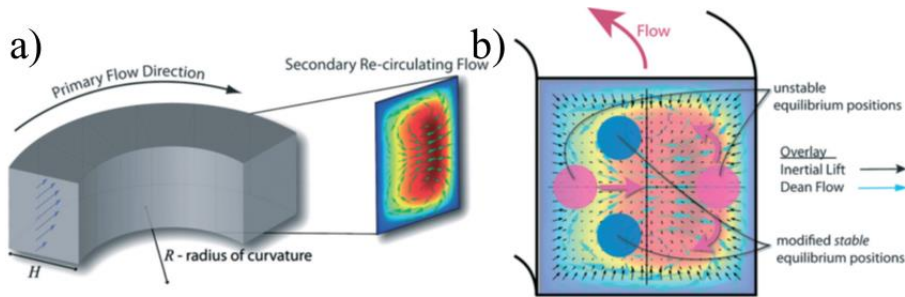


Fig. 11 a) Dean flow with two counter-rotating vortices is created in curved channels. Reproduced from ref.35. (b) Superposition of inertial lift force and Dean flow in a curved channel modifies the number and position of the inertial equilibrium positions. Reproduced from ref.56.

Particles of different dimension are influenced differently from the secondary flow and inertial lift forces to separate cells. Bhagat and colleagues [59] separate particles of  $7.32\ \mu\text{m}$  and  $1.9\ \mu\text{m}$  of diameter in a 5-loop spiral microchannel (see Fig. 9a). Hou *et al.* [60] employed a spiral channel to isolate circulating tumour cell (CTCs) from blood by using sheath flow with a recovery rate about of 85% (see Fig.9 b). In the spiral microchannel Yousuff and Hamid (see Fig. 9c) separate  $7\ \mu\text{m}$ ,  $10\ \mu\text{m}$  and  $15\ \mu\text{m}$  fluorescent beads for the flow rate of  $1800\ \mu\text{m}/\text{min}$  [61]. Instead, Ghadami *et al.* [62] (see Fig.9 d) proposed a spiral microchannel with a stair-like cross section to separate before particles of  $7\ \mu\text{m}$  and  $20\ \mu\text{m}$  in diameter (to test the device potential, obtaining a separation distance of  $260\ \mu\text{m}$  between particles) , and then human umbilical vein endothelial cells (HUVEC) and fibroblast cells (L929 cells). Spiral microchannels have been used also for separation of continuous CTCs from blood cells [63]. Son *et al.* [64] revealed that the separation behaviour of sperm cells is like  $3\ \mu\text{m}$  beads and smaller ones. Yuan *et al.* [65] studied the influence of symmetric serpentine structure on particle focusing. They used  $13\ \mu\text{m}$  dyed fluorescent polystyrene microspheres suspended in Newtonian and viscoelastic

liquids. It was concluded that there is an optimum value for the flow rate in which the separation efficiency is maximum.

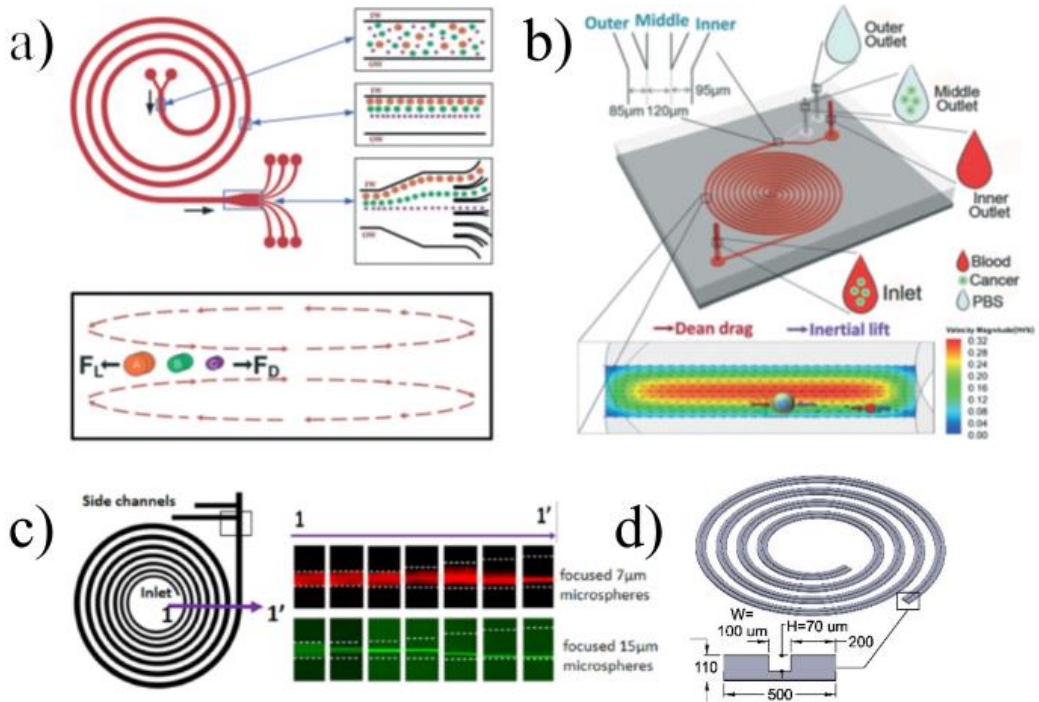


Fig. 12 a) Continuous triplet-particle separation in a spiral channel. Reproduced from ref.57. b) Double spiral microchannel for tumour cell separation and enrichment. Reproduced from ref.58. c) Spiral microchannel to separate particle of 7  $\mu\text{m}$ , 10  $\mu\text{m}$  and 15  $\mu\text{m}$  fluorescent beads. Reproduced from ref.59. d) spiral microchannel with a stair-like cross section for particle and cell separation. Reproduced from ref.60

### 2.4.1.3 Contraction–expansion channel

As mentioned, many geometries, can induce a secondary flow. For instance, in a specific range of flow rate expansion–contraction array presents, a balance between secondary flows and inertial lift forces on the suspended particles. Park *et al.*, reported a separation between polystyrene beads of 4  $\mu\text{m}$  and 10  $\mu\text{m}$  in diameter [66], blood plasma from RBCs [67] and cancer cells from whole blood [68] with contraction–expansion array (CEA) channels, in this device the contraction-

expansion channels are asymmetrical as showed in Fig. 10a . They used a sheath flow to focused particles along sidewall 1 (S1) (see Fig. 10a). Various forces act on the particles, such as shear-induced, wall-induced lift forces, and Dean drag forces. Under the influence of Dean drag forces and inertial forces, the equilibrium position of particles is formed at the position greater than 0.2 times H from S1. Consequently, when the magnitude of the inertial lift forces is larger than that of the Dean drag forces, the particles migrate toward sidewall 1 and occupy their equilibrium position where the sum of these forces becomes zero. In an opposite magnitude of these forces, the particles migrate toward sidewall 2, following the Dean flows. In another work, the contraction–expansion array patterned on two sides of the channel is used to Park *et al.* [69] to separate particles of 7  $\mu\text{m}$  and 15  $\mu\text{m}$  of diameter (see Fig. 10b). At the contrary Park’s work with asymmetrical device, this symmetrical contraction-expansion array does not present a sheath flow. Based on this separation technique there is the combination of inertial lift force and momentum-change-induced inertial force generated in the contraction–expansion region. The trajectory mismatch between particles and fluid elements around the contraction–expansion region induces the lateral drift of the equilibrium position. The extent of this lateral drift is variable according to particle size and flow rate, so particles of 15  $\mu\text{m}$  of diameter are focused at the center on channel, at the contrary of particles of 7  $\mu\text{m}$  of diameter. The effect of expansion geometry was studied from Liu *et al.* [70] that introduced four distinct focusing configurations with different particle sizes to separate plasma, RBCs, and cancer cells from blood. They found that the circle chamber has higher separation efficiency than a high-rectangle channel, low-rectangle one, and streamline channel (see Fig. 10c).

Instead, Moon *et al.* [71] combined a contraction-expansion array with DEP techniques to separate human breast cancer cells (MCF-7) from a spiked blood sample (see Fig. 10d). This technique has the advantage to generate a high-throughput filtration of blood cells to further enhance the separation efficiency and purity.

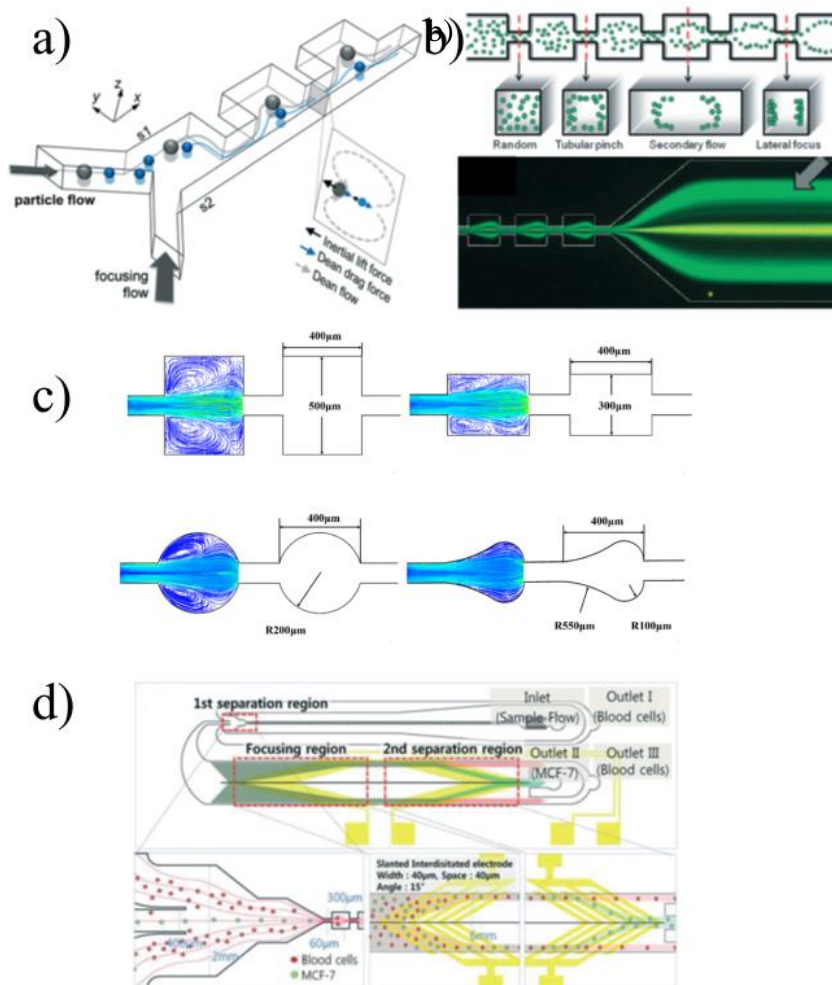


**Fig. 13** a) Inertial separation of particles by size in a CEA channel under the assistance of a sheath flow. Reproduced from ref.64. b) Continuous inertial separation in a multi-orifice microchannel according to the size-dependent lateral migration. Reproduced from ref.67 c) The schematic view of the channels: the High-rectangle channel, the low-rectangle channel, the circle channel, and the streamline channel. Reproduced from ref.68. d) Continuous high-throughput separation of human breast cancer cells (MCF-7) from blood cells by a combination of CEA and dielectrophoresis (DEP). Reproduced from ref.69.

#### 2.4.1.4 Other geometries

Kwak *et al.* [72] proposed a fishbone-shaped microchannel to separate 2  $\mu\text{m}$ , 6  $\mu\text{m}$ , and 13  $\mu\text{m}$  microparticles correspond to platelets, RBCs, and leukocytes of human breast cancer cells, respectively. They revealed that two smaller particles migrate toward the sidewalls, and the larger one focuses on the channel centreline. Micro-

pillars or herringbones are used in in the microchannels to affect particle behaviour. In this case, inertial and Dean drag forces result in particle separation. Zhao *et al.* [73] used a straight microchannel with arc-shaped groove arrays to induce a secondary flow in the channel's cross-section to separate 4.8  $\mu\text{m}$  and 13  $\mu\text{m}$  fluorescent polystyrene microparticles with the inlet flow rate of 1000  $\mu\text{l}/\text{min}$  (see Fig. 11).

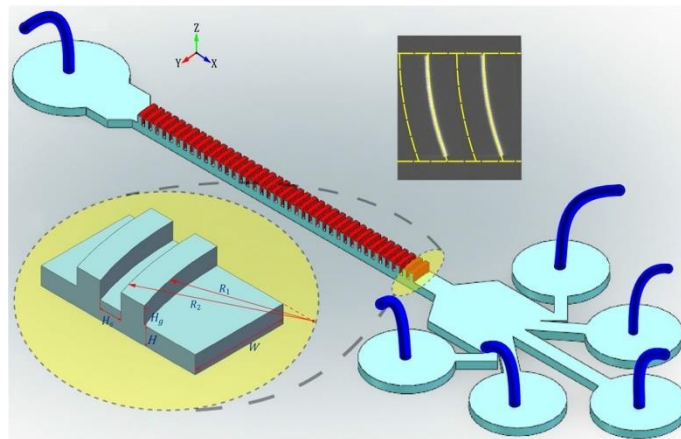


**Fig. 14** Microchannel with arc-shaped groove arrays. Reproduced from ref.71.

### 2.4.2 Viscoelastic separation

Viscoelastic fluid properties can generate a lateral migration of particles in function of viscoelastic forces. As already mention in section 2.2.2, this force,  $F_{eL}$ , acting on a particle, results from the non-uniform normal stress differences in viscoelastic fluid flows [74], [75] . It depends on shear rate, particle dimension and relaxed time of non-Newtonian fluid. In function of geometry, the balance between Drag force, viscoelastic force and inertial force can generate different equilibrium particle position.

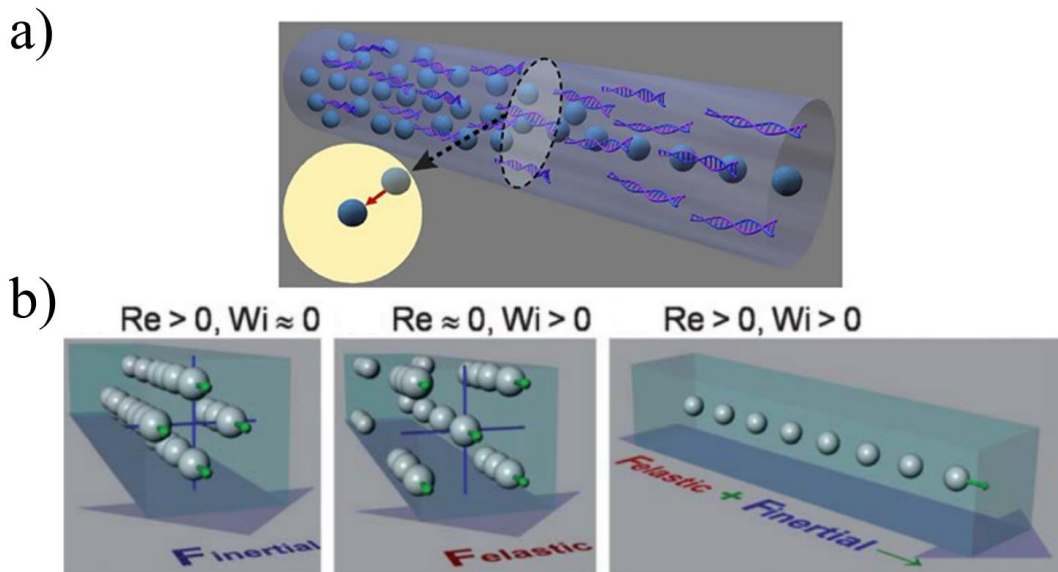


**Fig. 15** a) Schematic illustration for particle focusing, in a viscoelastic flow, through a cylindrical microchannel in presence of elasto-inertial forces. Reproduced from ref.74 b) Schematic illustration of the particle alignment: right, by inertia dominant flow, center by elastic dominant flow and left ‘Elasto-Inertial Particle Focusing’. Reproduced from ref.75.

Indeed, as showed in Fig.12, when viscoelastic forces are predominant, in the cylindrical channel, the particle moves toward the centreline (see Fig. 12a), while in a square channel, particles migrate also in the four cross-section corners (see Fig 12b-central) [76], [77]. However, at increased flow rate also inertial effect contributes to the equilibrium particle position. For example, for a square channel it has been demonstrated that the equilibrium particle position can be reduced to the central one of channel, due to the increasing role of the wall-induced inertial lift forces (see Fig. 12b-right) [77], [78]. Regarding this, many studies were carried out about cell separation using viscoelastic fluid properties. For instance, Nam *et al.* [79] separates particles of 1  $\mu\text{m}$  and 5  $\mu\text{m}$  diameter in 500 ppm polyethylene oxide (PEO) solution through a straight square microchannel (see Fig. 13a). They used three inlet channels, the central channel without particles was used to create a sheath flow to push particles to the sidewall of the channel. Then, particles migrate towards at the

centre of the straight channel depending on their size using by combination of elastic force and inertial lift forces. The authors achieved a more than 99.8% purity of platelets separation from dilute whole blood. Lim *et al.* [80] studied the difference between two viscoelastic fluid, 100 ppm PAA and 500 ppm PEO solutions This fluid presents different effect of second normal stress difference in a straight microchannel. They mixed particles with 1  $\mu\text{m}$  and 10  $\mu\text{m}$  of diameter. In both cases, larger particles reached the centreline at the outlet, however the smallest one presented different behaviour. In the mention PAA solutions, particles of 1  $\mu\text{m}$  of diameter spread across the entire cross section, while in PEO solution particles were focused to the centre or to the wall in function of the position of sheath flow (see Fig. 13b). This effect was due to rotational secondary flow. Indeed, the rotational secondary flow was more significant for small particles.

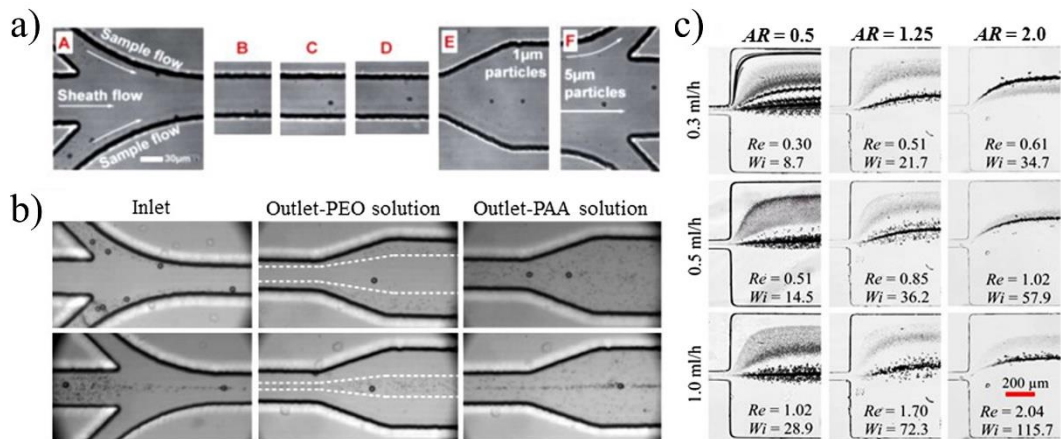


**Fig. 16** a) Illustration of lateral displacement of sheath flow-focused 1  $\mu\text{m}$  and 5  $\mu\text{m}$  diameter particles in 500 ppm PEO solution at different axial locations of a straight 2.5 cm long, 50  $\mu\text{m}$  wide square microchannel. Reproduced from ref.77. b) Snapshot images comparing the lateral displacement of 1  $\mu\text{m}$  and 10  $\mu\text{m}$  diameter particles in 500 ppm PEO (middle column) and 100 ppm PAA (right column) solutions when the particle mixture is initially focused toward the sidewalls (top row) and centerline (bottom row) of a straight 100  $\mu\text{m}$  wide, 50  $\mu\text{m}$  deep microchannel. Reproduced from ref.78 c) Stacked images illustrating the effect of channel aspect ratio (AR) on the separation of 3  $\mu\text{m}$  and 10  $\mu\text{m}$  diameter particles in 1000 ppm PEO solution via eiPFF in 100  $\mu\text{m}$ , 40  $\mu\text{m}$  and 25  $\mu\text{m}$  (from left to right) deep microchannels, respectively, with a fixed 50  $\mu\text{m}$  width. Reproduced from ref. 80.

Another similar structure was used in pinched flow fractionation (PFF) [81], Lu and Xuan [82] studied multiple effect dimensionless numbers (Re, Wi, El, AR and the sheath to particle flow rate ratio) in elasto-inertial pinched flow fractionation (eiPFF). The authors of this study found that different AR can permit different lateral displacement of 10  $\mu\text{m}$  diameter particles from the wall comparing them to 3  $\mu\text{m}$  particles diameter in 1000 ppm PEO solution (see Fig. 13c). Interestingly, particles of 3  $\mu\text{m}$  of diameter migrates from the sidewall more than particles of 10  $\mu\text{m}$  of diameter with an AR 2 (i.e., 50  $\mu\text{m}$  W and 25  $\mu\text{m}$  H) at low flow rate, while at high flow rates the position of particles are inverted. This phenomenon was not observed in the devices with both AR 0.5 and AR 1.25. To the best of our knowledge, there are no other studies regarding these outcomes in literature.

However, in 2011 the first study of particle separation without sheath flow in a non-Newtonian fluid was made by. Yang *et al.* [77] in a single straight square microchannel. They used 250 ppm PEO solution to separate particles of 5.9  $\mu\text{m}$  and 2.4  $\mu\text{m}$  of diameter (see Fig. 14d). Based on this concept, Ahn *et al.* [83] examine different factor: the upper limit for the polymer concentration, to avoid shear thinning effect, optimal flow rates for the separation and particle-particle interaction. In particular, the concentration of particles plays an important role in the purity of separated particles, when concentration is high the purity decrease (see Fig. 14a).

Differently, Nam *et al.* [84] proposed a two-stage device using viscoelastic fluid flow. In the first stage particles are focused at the centre of channel due to elasto-inertial forces (see Fig. 14c). Then the central channel is divided into symmetric channel in which elastic lift is dominant. They used a highly elastic solution (8% polyvinylpyrrolidone PVP solution) with a very low flow rate to separate particles of 5  $\mu\text{m}$  and 10  $\mu\text{m}$  of diameter. The optimization of microfluidic device was made in the following works to separate, at first tumour cells from leukocytes using a weakly elastic 0.1% hyaluronic acid (HA) with a throughput of  $4 \times 10^5$  cells/min [85] and then malaria parasites from a lysed blood in 0.1% HA solution at a flow rate of 400 ml/min with over 90% recovery rate and purity [86].

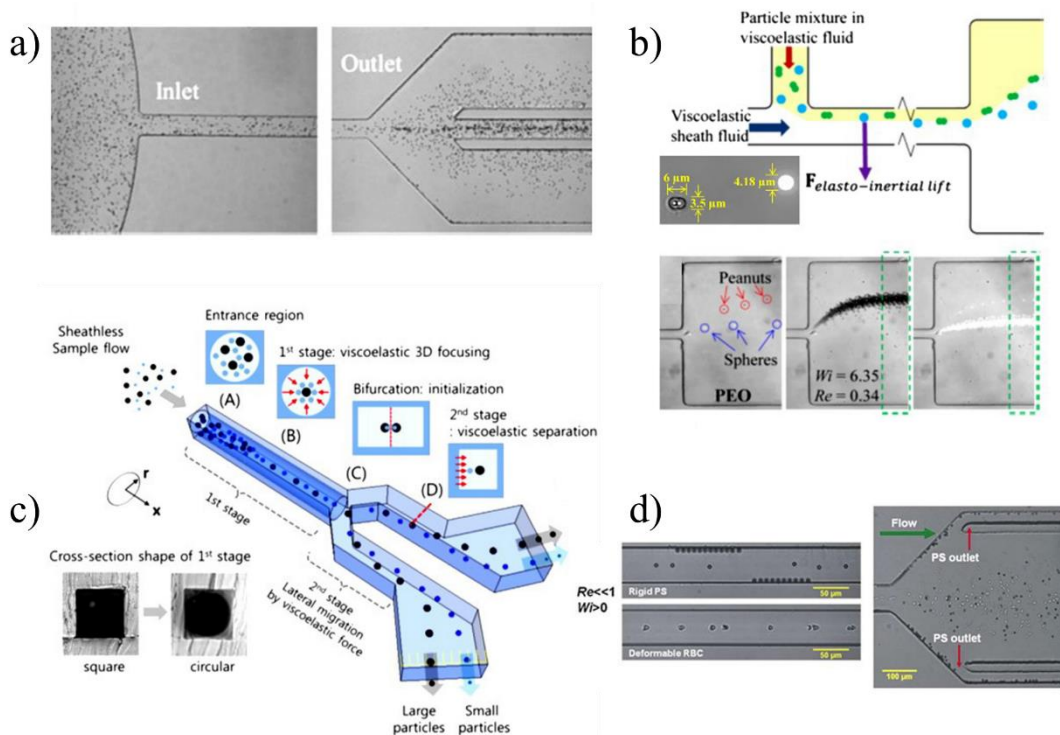


**Fig. 17** a) Snapshot images showing the size-based enrichment of 4.5 μm diameter PS particles from 2.3 μm ones in the flow of 250 ppm PEO solution through a straight square microchannel. Reproduced from ref.81 b) Schematic illustration (top row) and experimental images (bottom row) for sheath-flow separation of peanut and spherical PS particles of equal volume (inset image) via eiPFF in 1000 ppm PEO solution through a straight rectangular microchannel. Reproduced from ref.85 c) Schematic illustration of a two-stage microfluidic device for sheath-less focusing and size-based separation of particles in viscoelastic fluid flows. Reproduced from ref.82 . d) Snapshot images for the elastic focusing (left) of rigid 6 μm diameter PS particles and their elastic separation (right) from deformable RBCs (stained in the right image) in 6.8 wt.% PVP solution flows through straight square microchannels under negligible inertia. Reproduced from ref.86.

All these studies are based on the difference of particle size, while comparatively little on separation of particles based on shape or deformability can be found in literature for viscoelastic fluids. Lu and Xuan [87] used the eiPFF to separate spherical and peanut shaped polystyrene particles of nearly equal volume. They achieve the separation between 5 μm spheres of diameter and 3.5 μm diameter and 6 μm long peanuts in 1000 ppm PEO solution in a channel with an AR 0.5, obtaining 95% efficiency and purity (see Fig. 14b). In their work, they demonstrate a strong dependence of shape in the flow-induced elasto-inertial lift correlate with the rotational effects of non-spherical particles. However, the sheath-less shape-based

particle separation is strongly influenced by the flow rate ( $Re$ ), PEO concentration ( $Wi$ ) and channel geometry ( $AR$ ). Yang *et al.* [88] performed a separation of RBCs from the WBCs -in a diluted whole blood- in an inertia-less flow, due to the dominant cell deformability-induced lift over the elastic lift near the channel corners using a 6.8 wt% polyvinylpyrrolidone (PVP) solution. The authors utilized these phenomena to separate polystyrene particles from RBCs, and as well less deformable WBCs from diluted whole blood with a high enrichment ratio (see Fig. 14d).

### **2.4.3 Filtration**

#### *2.4.3.1 Hydrodynamic filtration*

Hydrodynamic filtration uses multiple branches outlet in which fluid and particles go through the side channels [89] according to the flow rate. In function of dimension of particles, they will be next to or more distant from the wall. Particles in proximity of sidewalls flow in the outlet when relative volume flow rate of the that outlet is higher than a specific value. In literature, it was found a critical diameter value that can be determined using the definition of the virtual width ( $w$ ) of the flow entering the side channel. Therefore, the diameter of particles in a specific outlet can be calculated in according to volume flow rate of that branch, so the particle with a diameter smaller than the than  $w/2$ , will go out in that outlet (Fig. 18b) [90]. Using this theory, Chiu *et al.* [91] separate polystyrene microparticles with 2.7 and 10.6  $\mu\text{m}$  diameters by sheath flow focusing (see Fig. 15a). The sheath flow consents a focusing of particles along the sidewall. This device reached a purity of  $99.2\pm 0.4\%$  and  $97.9\pm 0.5\%$  for the small and large particles, respectively, at a sample throughput of 10  $\mu\text{l}/\text{min}$ . Hydrodynamic filtration was used for the separation of RBCs from plasma [92] and blood cell classification [93]. In some cases, hydrodynamic filtration is combined with a magnetic focusing to enhance the throughput of separation of blood cell, human lymphocyte cell line [94], and paramagnetic particles with 5 and 11  $\mu\text{m}$  diameters [95].

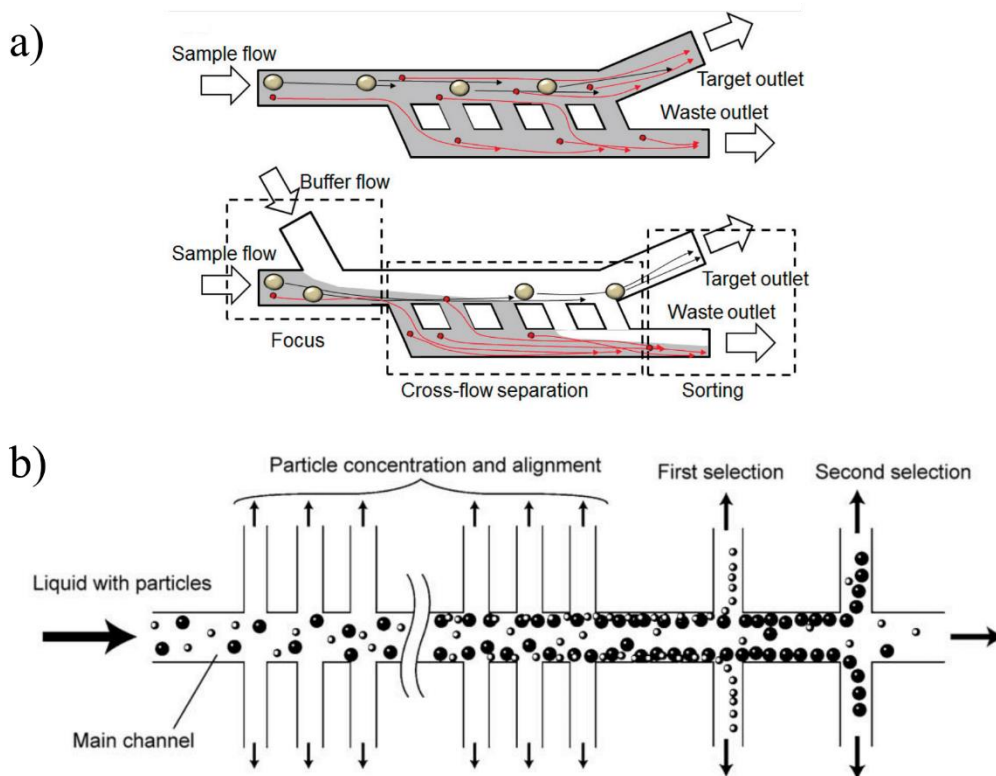


**Fig. 18** a). Schematic of typical crossflow filtration and separation mechanism Reproduced from ref.89 b) Schematic diagram showing particle concentration and classification in a microchannel having multiple branch points and side channels. Reproduced from ref.88.

### 2.4.3.2 Hydrophoretic filtration

Ridge-induced hydrophoretic filtration relies on the formation of a lateral pressure gradient within a microfluidic channel due to flow-altering micropatterns. A successive array of slanted obstacles on the microchannel floor and ceiling induces a pressure gradient across the width of the channel to focus cells to precise locations within the generated local pressure field according to type and then separates those cells [96]. Using this phenomenon, Choi *et al.* developed a device that exploits differences in both the size and deformability of cells for passive sorting (Fig. 19) [97].

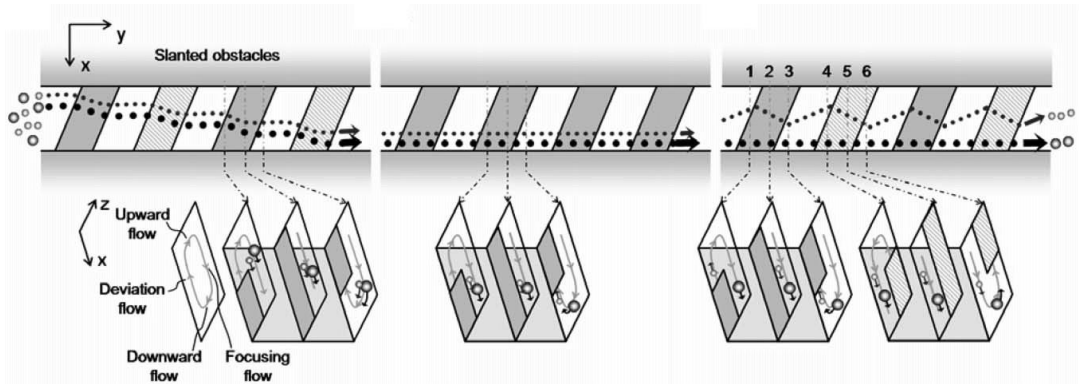


**Fig. 19** Hydrophoretic separation principle. Shaded- and lined-areas denote lower and upper slanted obstacles, respectively. A flow direction is along the y-axis. Reproduced from ref.95.

#### 2.4.4 Deterministic lateral displacement

Deterministic lateral displacement (DLD) is a technique in which cells migrate in a microfluidic channel influenced by the presence of micropattern (e.g., posts, ridges, groves, ratchets). In these systems, control over migration is given by the layout of the array such that cells, smaller than a critical diameter  $D_c$  ( $a < D_c$ ), move with the convective flow and cells larger than a critical diameter ( $a > D_c$ ) move in a direction dictated by the arrays (see Fig. 17a) [98]. In other words,  $D_c$  is defined to describe the motion of particles through the pillar gap. Indeed, Huang *et al.* use an array of microposts (with a periodic distance between posts) displaying that smallest cell could more easily traverse between obstacles than larger cells, permitting their separation [99]. In another work, Inglis *et al.* fractionate undiluted whole blood to isolate cancer cells, studying the critical dimensions of cells and microposts [100], [101]. All these separations are based on dimension, Beech *et al.* demonstrated that this technique was a useful tool to isolate cells with a different shape and deformability [27]. In other works, different pillar shapes were used such as triangle [102], airfoil [103], I-shaped [104], L-shaped [105], asymmetric shape [106], and optimized shape [107] instead of cylindrical one. The particle placed in the pillar gap may follow the initial streamline and move in the zigzag path or displaces to the next

streamline laterally (displacement mode) depends on its size. Zhang *et al.* [108] (see Fig. 17b) developed a general equation for critical diameter:

$$D_c = \alpha G \varepsilon \beta \quad \text{Eq. 2.4-1}$$

where  $\alpha$  and  $\beta$  are dimensionless geometric coefficient for different shapes of pillars, using circular, diamond, square, and triangular structures,  $\varepsilon$  is the row-shift fraction defined as  $\varepsilon = \Delta\lambda/\lambda$  (where  $\lambda$  is post centre-to-centre distance and  $\Delta\lambda$  is row shift) and  $G$  is the distance post gap. They separate rigid and deformable RBC revealing that it could not be possible to determine a critical size for deformable particles.

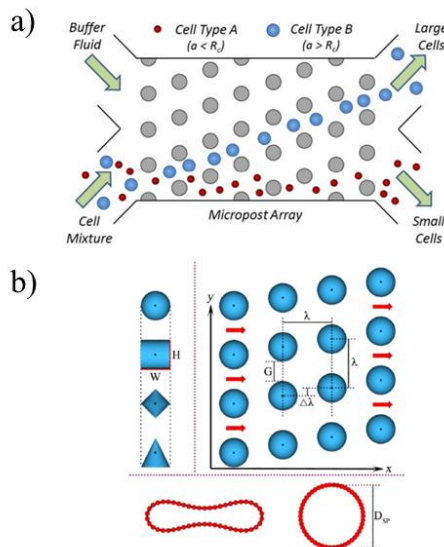


**Fig. 20** Cell sorting by deterministic lateral displacement. Large cells (depicted in blue) migrate away from the small cells (depicted in red) in the initial streamline due to the engineered size and spacing of the microposts in the microfluidic channel. Reproduced from ref.75. b) Schematic illustration of the geometry and structures of simulated DLD systems. Reproduced from ref.85.

### 2.4.5 Trilobite

Recently, a new type of separation microfluidic device (called Trilobite) was developed by Dong *et al.* [109]. This special device uses streamlined turbine blade-like micropillars based on the counter-flow principle (see Fig 18). During fluid flow, the elliptical cylinder generates a local pressure difference, so the smaller particles are withdrawn from the main flow in the penetrate channel. Contrary to the case of

cross-flow microfilters, the angle  $\alpha$ , is the angle between the main flow and penetrating flow, which should be greater than  $90^\circ$  [109].

Dong *et al.* [109] also develop a counter-flow units with a honeycomb structure, demonstrating that the particle concentration performance depends on the volume flow rate of the main flow. Another shape of counter-flow units was studied from Hönsvall *et al.* [110]. They present a rectangular arrangement of counter-flow units to concentrate microalgae and revealed that rigid particles are concentrated more easily than deformable ones.

Mossige *et al.* [111] concentrate their work on understanding how inlet and outlet conditions affect the operational modes of the microchip using permeate (penetrating) and concentrate (main) flows, the saddle point, and permeate layer thickness,  $T_p$ , (see Fig. 18b). In more detail,  $T_p$  varies little and decreases with  $Re$  for the downstream and upstream saddle points, respectively. When  $T_p$  is smaller than the pore size of the permeable wall (for the upstream saddle point), a clog-free pattern is determined. In another work, Mossige *et al.* [112] filtrate rigid spherical particles without clogging obtaining a high throughput of 29 ml/min and reaching the purity of 96%. They explain that the optimal position of the saddle point is that one posterior of the counter-flow unit, so when saddle point moves toward the upstream of this position, the device is clogging free. Different types of separation were performed, live algae cells, sphere-like, rod-like, and disk-shaped cells [113]. In a specific case of algal cells, the flow rate should be higher than synthetic microspheres to obtain clogging free.

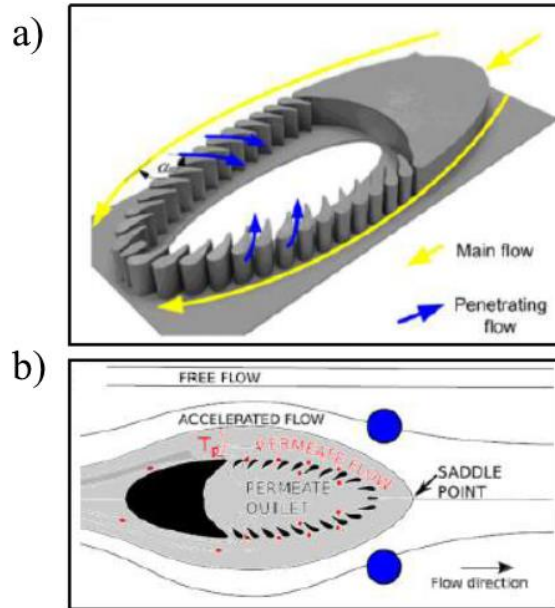


**Fig. 21** a) Schematic of the Trilobite separator. b) Hydrodynamic filtration principle of the Trilobite-shaped separator. Reproduced from ref.109.

## 2.4.6 Transient cellular adhesion

Different studies have concentrated their attention on microfluidic devices that consent the impermanent adhesion of a specific class of cells to a surface [114]. In function of this, Lee *et al.* [115] implemented a device in which a flat surface containing a striated pattern of P-selectin (type -1 transmembrane protein that functions as a cell adhesion molecule (CAM) on the surfaces of activated endothelial cells) permits the adhesion of HL60 cells thanks to high affinity between the PSGL-1 ligand (P-selectin glycoprotein ligand-1 (PSGL-1) is a glycoprotein found on white blood cells and endothelial cells that binds to P-selectin) and P-selectin. The isolation of neutrophils from blood was performed by Bose *et al.* with high enrichment without cellular agitation [116].

Another type of device uses cell rolling to study the surface interaction. Indeed Choi *et al.* displayed a device in which multiple ridges along the floor can induce cellular collisions for sorting (Fig. 22) [117]. They modify the device surface with a

P- selectin to stimulate an interaction with target cells. In this case, target cells were push toward one side of device while non target cells migrate towards other side [117], [118].

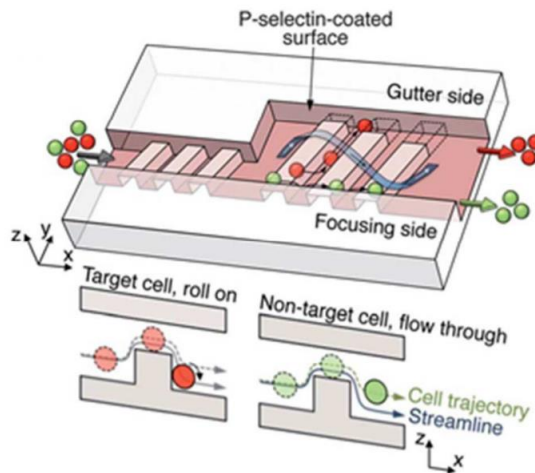


**Fig. 22** Cell sorting by deterministic cell rolling. Target cells (red) interact with the surface, roll across the ridges, and laterally displace toward the gutter side whereas non-target cells (green) flow over the ridges, not interacting with the surface, and exit on the focusing side. Reproduced from ref.115.

### 2.4.7 Cellular immobilization

Other techniques that do not depend on the size, density, or charge of the cells is the cellular immobilization. It is a technique that investigate the non-transient capture, or immobilization, of cells on surfaces or in columns. The affinity chromatography [119], [120] is the earliest method to fractionate cell populations due to interaction between cell-surface receptors and immobilized ligands (**Fig. 23**). This technique can be used with different types of matrices [121]. Indeed, many studies use antibodies for cell-specific isolation [122], [123]. For example, Hyun *et al.* used a microfluidic device coated with antibodies for the enrichment of CTCs [124].

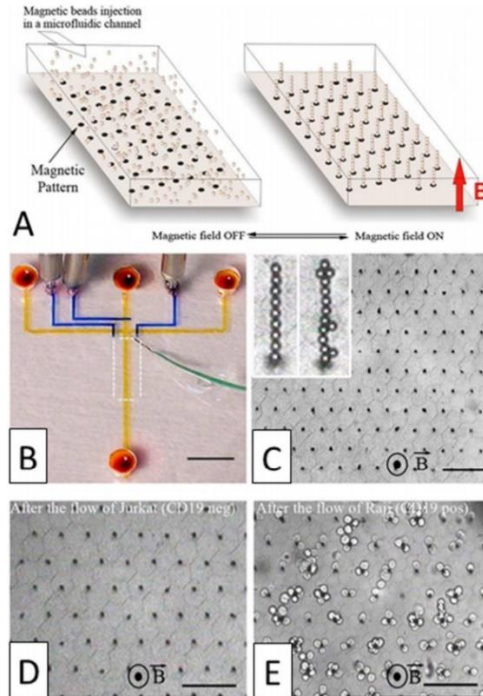


**Fig. 23** Magnetic self-assembly of biofunctional magnetic beads for isolating rare cells. A) Schematic of a hexagonal array of magnetic ink (left) can guide the self-assembly of magnetic beads conjugated antibody in the presence of a vertical magnetic field (right). B) Photograph of the microfluidic device. Optical micrographs of the columns after C) the assembly of magnetic beads, D) the passage of 1,000 Jurkat cells (antibody negative), and E) the passage of 400 Raji cells (antibody positive) (scale bar: 80 μm). Reproduced from ref.101.

### 3 Materials and methods

#### 3.1 Design Principle

The design of our device (Fig. 24) is divided into 5 parts: inlet capillary ( $C_A$ ), first observation channel ( $C_B$ ), second observation channel ( $C_C$ ), expansion channel ( $C_D$ ) and outlet channels  $E$  with subsequent sample collection reservoirs. The migration of particles suspended in a viscoelastic fluid is strongly dependent on flow conditions. Thus, it is important to define non-dimensional numbers to compare the effect of different forces on the particle migration. The viscoelastic and inertial effects were measured using  $Wi = \dot{\gamma}\lambda$  and  $Re = \rho vL/\eta$ . Low Reynolds number values assure that inertia is irrelevant. In the capillary, particles of different sizes migrate toward the equilibrium position at the centre induced by fluid viscoelasticity.

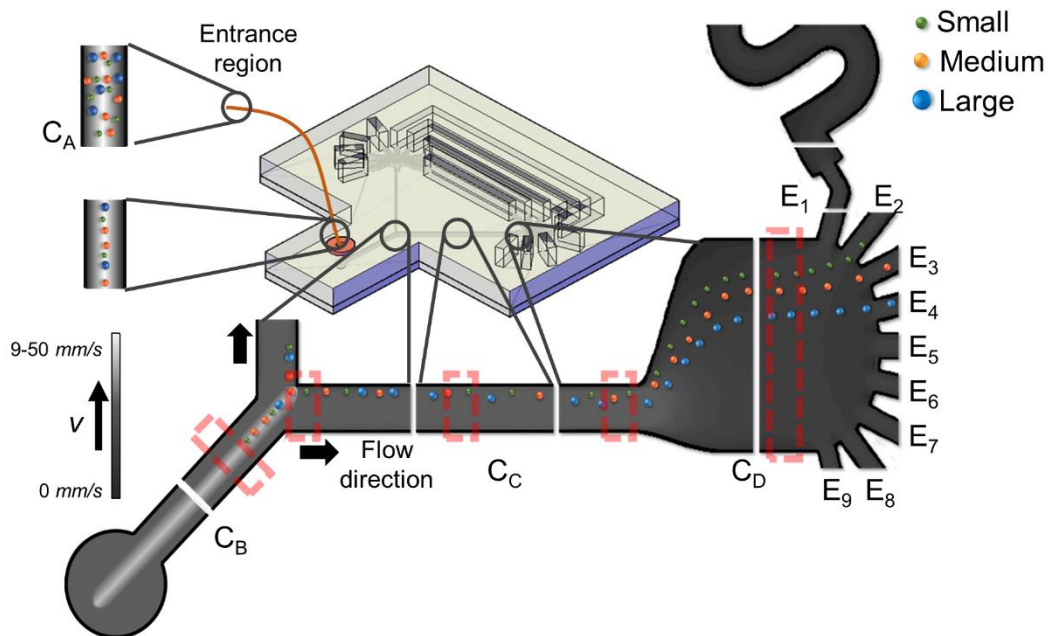


**Fig. 24** Schematic illustration of the concept of microfluidic device on the right viscoelastic 3-D focusing into capillary was shown. Then a top view of microfluidic device is presented. and a schematic illustration of microfluidic device,  $C_B$  bifurcation region for the initialization,  $C_C$  channel for particle separation in function of size,  $C_D$  amplification of particle separation and  $E_1...E_9$  the outlet channel. The red zones are the section that are analysed in the results, in particular 0 mm (first red square of  $C_C$ ), 12,5 mm (second red square of  $C_C$ ) and 25 mm (third red square of  $C_C$ ). Dimensions are not in scale.(red line)

Indeed, 3D particle focusing can be achieved along the centreline (see sec. 2.2.2)) by utilizing first normal stress difference ( $N_1$ ) of a viscoelastic fluid. In particular, the length and inner radius of the inlet capillary was established using the non-dimensional alignment parameter  $\theta$  [125]:

$$\theta \approx \dot{\gamma} \lambda \cdot \frac{\beta^2 L}{D} > -\ln(3.5\beta) \sim 1 \quad \text{Eq. 3.1-1}$$

where  $\beta$  is blockage ratio ( $a/D$ , where  $a$  is the particle diameter and  $D$  is the channel diameter) and  $L$  is the capillary length. This Eq. 3.1-1 is valid for  $\beta \leq 0.1$ ,  $Re \ll 1$  and  $De \ll 1$  [1]. The alignment of particle in  $C_B$  is maintained from  $C_A$  (in which  $\theta$  is evaluated), because we have no other significant effects which disturb our previous ( $C_A$ ) alignment, for this reason  $\theta$  can be neglected for the length of  $C_B$ . PSL 20 is the largest particle used in our work, for this reason the width of  $C_A$  and  $C_B$  has been chosen of 200  $\mu\text{m}$ , respecting the  $\beta$  condition of circa 0.1. The design concept considered the device dimensions since the flow rate and the elastic property of the suspending medium can easily be varied during the experiment in the range of PEO 0,4 to PEO 0,2 and 5 mm/s to 50 mm/s respectively (see sec. 4.1). The length of  $C_A$  was chosen to permit the alignment of all particles PSL7, PSL10, PSL15 and PSL20 using PEO 0,4 (see Table 1). The length of the  $C_C$  was chosen such that only larger particles (PSL20) can be focused along the centerline, which could maximize the difference in the lateral displacement between PSL7 and PSL20.

**Table 1**  $\theta$  value for PEO 0,4 for PSL7, PSL10, PSL15 and PSL20 in  $C_A$  and  $C_C$ .

	$-\ln(3.5\beta)$	$\theta_{C_A}$	$\theta_{C_C}$
<b>PSL7</b>	1.81	1.92	0.18
<b>PSL10</b>	1.45	2.3	0.36
<b>PSL15</b>	1.05	4.6	0.81
<b>PSL20</b>	0.762	8	1.44

In this device, the particles are aligned at the center of  $C_A$  ( $W_A = 0.15 \text{ mm}$ ,  $L_A = 350.0 \text{ mm}$  and  $H_A = 0.15 \text{ mm}$ ), then, particles enter  $C_B$  ( $W_B = 0.2 \text{ mm}$ ,  $L_B = 2.0 \text{ mm}$  and  $H_B = 0.15 \text{ mm}$ ) maintaining the alignment position of  $C_A$  in the channel centreline. At the end of  $C_B$ , a symmetric bifurcation connected the channel to two equal designed  $C_C$  sections. The bifurcation allows particles or cells to get close to the inner wall of  $C_C$  (wall<sub>1</sub> Fig. 25), defined as initial particle position (called 0 mm, Fig. 25). In  $C_C$  ( $W_C = 0.2 \text{ mm}$ ,  $L_C = 25.0 \text{ mm}$  and  $H_C = 0.15 \text{ mm}$ ) elastic forces ( $F_{El}$ ) act on the particles is proportional to the cube of particle diameter, so larger particle will migrate faster to the equilibrium position (centre line of the channel), while smaller particles will require larger distances (Fig. 24).

$$F_{El} \propto a^3 \eta \lambda_t \nabla \dot{\gamma}^2 \quad \text{Eq. 3.1-2}$$

where  $C_{el}$  is the non-dimensional elastic lift coefficient. At the expansion region ( $W_D = 0.9 \text{ mm}$ ,  $L_D = 1.2 \text{ mm}$  and  $H_D = 0.15 \text{ mm}$ ), the difference in lateral displacements of the particles is maximized and different particle types are collected in separated outlet channels (data shown in results section). Note that we have designed five output channels for particle collection while other four channels were added to balance the hydraulic resistances of the microfluidic outputs and to collect the remaining fluid (name them with the name  $E_1, \dots, E_9$  Fig. 25)).

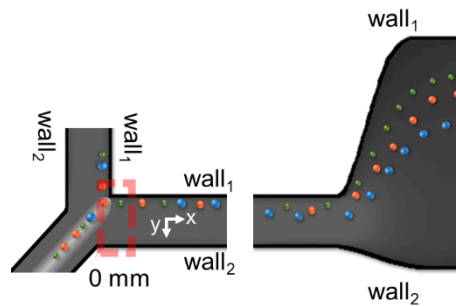


**Fig. 25** Schematic illustration of microfluidic device.

To simulate velocity profile and shear rate of our device, we used the commercial CFD COMSOL Multiphysics vers 5. Reference pressure was considered at channel outlets ( $p = 0 \text{ Pa}$ ) and no slip condition was adopted at the walls. Laminar flow with

different average velocities ( $V_{\text{media}}$  9.2 mm/s, 25 mm/s and 49 mm/s) were set at the inlet. The fully developed velocity profile and the shear rate were evaluated by 3D finite element simulations. Fig. 26 Velocity profile ( $V_{\text{media}}$  4.5 mm/s, 12.5 mm/s and 24.5 mm/s). In Fig. 27 instead, the shar rate profile is showed. The velocity in  $C_C$  is lower than velocity in  $C_B$  due to the presence of bifurcation. When flow rate increase, also the shar rate at the wall increase.

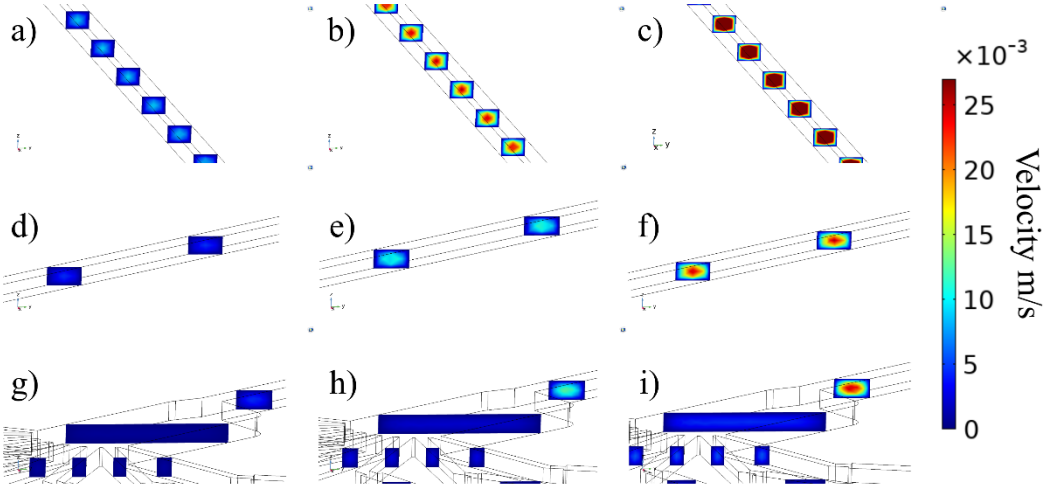


**Fig. 26** Velocity profile at the average velocity of 4.5 mm/s in a)  $C_B$ , d)  $C_C$  and g)  $C_D$ , 12.5 mm/s in d)  $C_B$ , e)  $C_C$  and h)  $C_D$  and 24.5 mm/s e)  $C_B$ , f)  $C_C$  and i)  $C_D$ .

In Fig. 28 the simulation of lateral displacement of PSL7, PSL10, PSL15 and PSL20 are showed. In these simulations, we have used the combination of two physics, laminar flow and particle tracing for fluid flow.

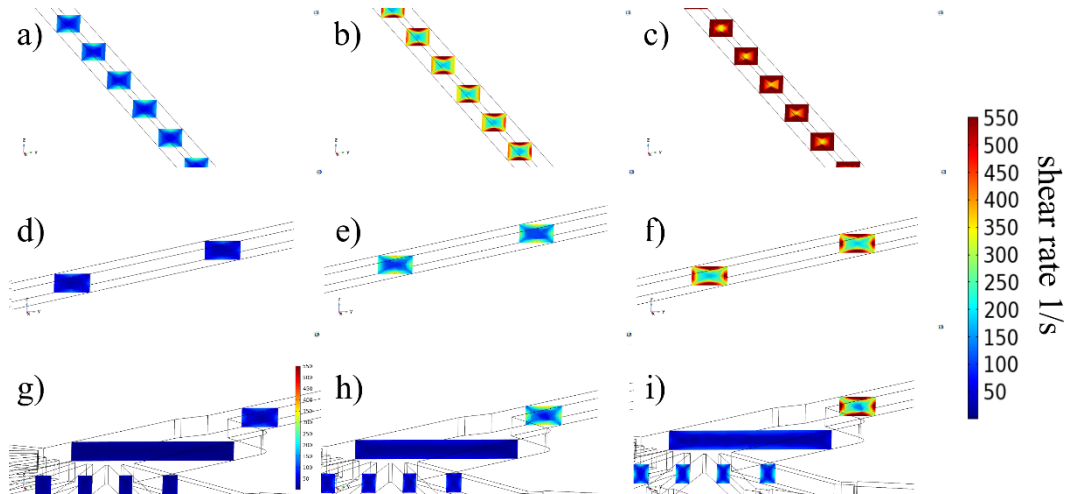


**Fig. 27** Velocity profile at the average velocity of 4.5 mm/s in a)  $C_B$ , d)  $C_C$  and g)  $C_D$ , 12.5 mm/s in d)  $C_B$ , e)  $C_C$  and h)  $C_D$  and 24.5 mm/s c)  $C_B$ , f)  $C_C$  and i)  $C_D$ .

In particle tracing for fluid flow, we imposed two types of forces, drag force and a force directed in  $y$  direction ( $F_y$ ). The initial position of particles was set at  $z$ -direction between 73 and 77  $\mu\text{m}$  and  $y$ -direction from 0 to 30  $\mu\text{m}$ .

Afterwards, we estimate the magnitude of acting forces using Eq. . The considered force is an estimation of force to result in a lateral displacement of investigated particles. In Fig. 28  $L_p$  of PSL7, PSL10, PSL15 and PSL20 at  $V_{B,\text{max}}$  22 mm/s using PEO 0,2 (Fig. a) and PEO 0,4 (Fig. b) with forces of  $F_y \propto 10^{-12}\text{N}$ ,  $F_y \propto 10^{-12}\text{N}$ ,  $F_y \propto 10^{-11}\text{N}$  and  $F_y \propto 10^{-11}\text{N}$  for PEO 0,4 and  $F_y \propto 10^{-13}\text{N}$ ,  $F_y \propto 10^{-13}\text{N}$ ,  $F_y \propto 10^{-12}\text{N}$ , and  $F_y \propto 10^{-12}\text{N}$  for PEO 0,2, respectively. In Fig. 28c the image of simulation of PSL20 at  $V_{B,\text{max}}$  22mm/s is showed.

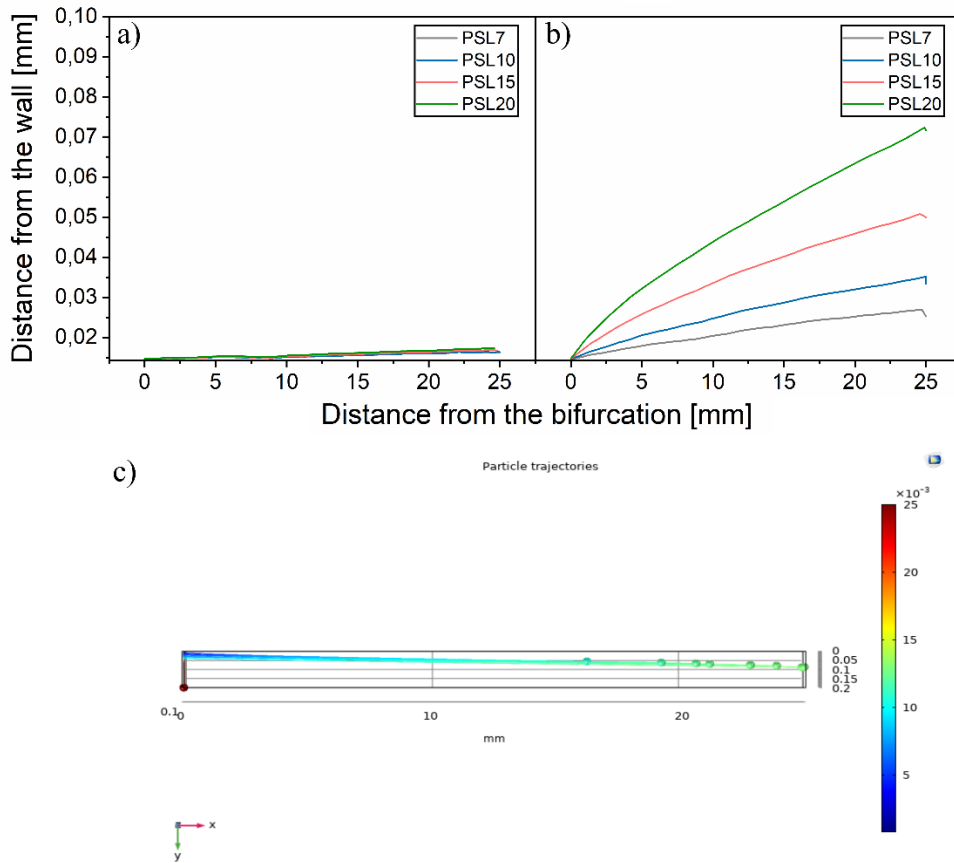


**Fig. 28** Simulation of PSL7, PSL10, PSL15 and PSL20 using a) PEO 0,2 and b) PEO 0,4 at  $V_{B,max}$  22mm/s. c) Comsol image of PSL20  $L_p$ .

### 3.2 Device fabrication

The device was fabricated with a double replica molding technique. Briefly, the device was realized in Poly methyl methacrylate (PMMA, GOODFELLOW) of 3 mm thickness using a standard micromilling machine (Fig. 29a).

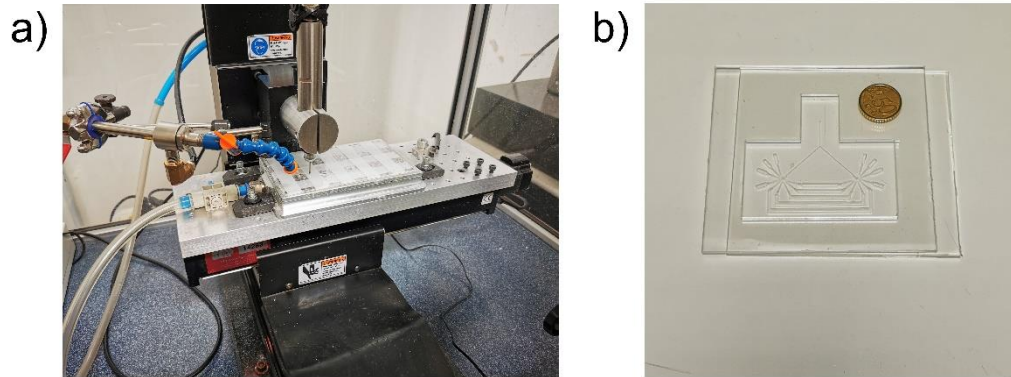


**Fig. 29** a) Photo of standard micromilling machine. b) Photo of master in PMMA of microfluidic device.

A first replica (Master) in polydimethylsiloxane (PDMS) using 14,3% cross linker (Sylgard 184, Mascherpa) was realized baking and curing at 80°C for 1 hour (Fig. 30Fig. 29b). After the curing, a silanisation process was made for 1 hour at 100°C to assure the separation from the other replicas (Fig. 30c). Then, a positive replica in PDMS was realized from the master using 14.3% cross linker and the reservoir was cut, while the inlet was realized using a punch of 1 mm (Fig. 30d). The bottom of the device was realized with PDMS sheet of 3 mm using again 14.3% cross linker and both substrates were bonded with a plasma treatment of 50W for 1 min (Plasma Femto, DIENER). The inlet capillary is glued on the device with a biphasic glue and stick together with a PDMS seal (Fig. 30e).

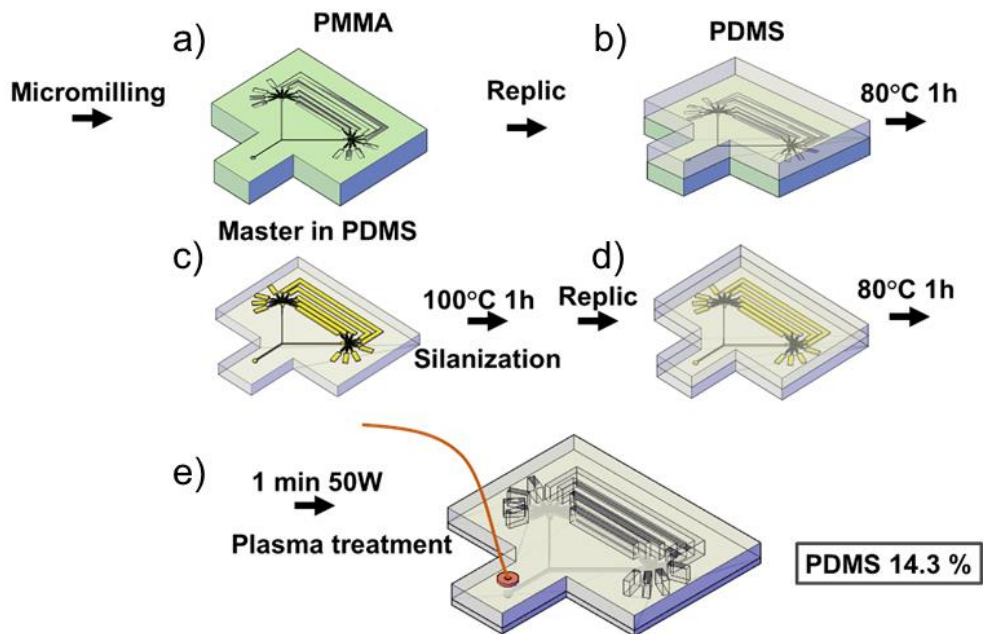


**Fig. 30** Schematic illustration of device fabrication. a) the device realized in PMMA using a standard micromilling machine. b) A first replica (Master) in PDMS. c) Silanisation process for 1 hour at 100°C. d) A positive replica in PDMS realized from the master. e) Positive replica and substrate bonded with a plasma treatment.

### 3.3 Rheological analysis of suspending fluid

The suspending liquids used in this work are phosphate-buffered saline (PBS, EUROCLONE) solutions with Polyethylene oxide (PEO, SIGMA-ALDRICH, UK,  $M_w$  4MDa) of different concentration (0.1, 0.2, 0.3 and 0.4 wt%) and 70 v/v% PBS solution of Glycerol (Gly, SIGMA-ALDRICH, UK).

Before each measurement, we filtered (0.45  $\mu\text{m}$  pore size) and degassed the experimental solutions for optimal sample homogenization. In addition, we tested the rheological fluid properties of the different solutions using a standard stress-controlled rheometer (MCR 302, ANTON PAAR) using a double gap geometry (Fig. 31a).

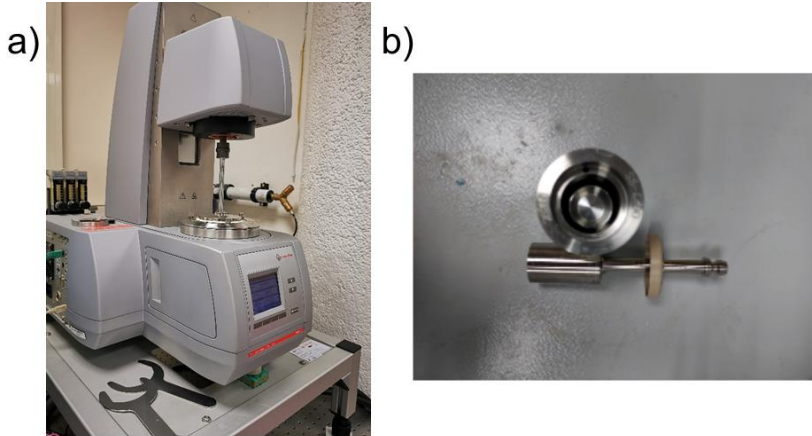


*Fig. 31 a) rheometer MCR 302, ANTON PAAR. b) Top view of double gap geometry.*

In more detail, the PEO solution viscosities ( $\eta$ ) were investigated for a wide range of shear-rates ( $\dot{\gamma}$ ), where the PEO 0.1 wt% (PEO 0,1) and PEO 0.2 wt% (PEO 0,2) displayed a near constant-viscosity in the whole range of investigated shear rates (see Fig. 31b). PEO 0.3 wt% (PEO 0,3), PEO 0.4 wt% (PEO 0,4) and PEO 0,5 wt% (PEO 0,5) presented a constant-viscosity region at low shear rates, and then displayed shear-thinning features above a critical value of shear rate. Our experiment showed a near constant-viscosity in the whole range of investigated shear rates.

Afterwards, we measured the fluid relaxation times ( $\lambda$ ) of each investigated PEO solution analysing obtained flow curves with the Bird-Carreau fitting approach (see Table 1). Briefly, the Bird-Carreau model conveniently describes non-Newtonian fluids as a function of the velocity field, given by:

$$\eta(\dot{\gamma}) = \eta_{\infty} + (\eta_0 - \eta_{\infty})[1 + (\lambda\dot{\gamma})^2]^{\frac{(n-1)}{2}} \quad \text{Eq. 3.3-1}$$

with  $\eta_0$  the zero-shear viscosity,  $\eta_{\infty}$  the infinite-shear viscosity, in the power-law index,  $\lambda$  the relaxation time constant [126].

The obtained longest relaxation time value was  $\lambda = 0.25$  ms for PEO 0.5.

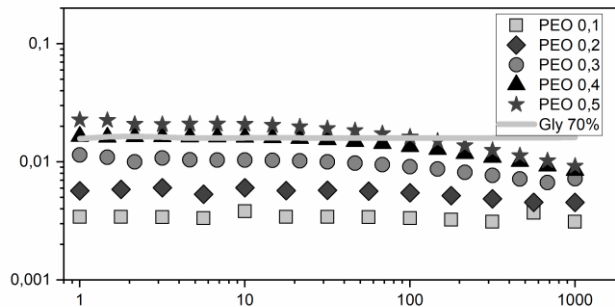
**Table 2** Values of fluid relaxation times and viscosity of each investigated PEO solution and viscosity of Gly 70%.

<b>PEO</b> [wt%]	<b><math>\eta</math></b> [Pa*s]	<b><math>\lambda</math></b> [ms]
0.50	0.0197	0.25
0.40	0.0155	0.19
0.30	0.0101	0.13
0.20	0.0054	0.07
0.10	0.0034	0.03

<b>Gly</b> [v/v%]	<b><math>\eta</math></b> [Pa*s]
70	0.0160

Additionally, a Glycerol in PBS solution with similar viscosity of PEO 0.4 (Fig. 32) was produced to compare the lateral displacement of particles in Newtonian versus non-Newtonian fluids. The viscosity of Gly 70% and PEO 0,4% are 0,016 Pa·s and 0,0154 Pa·s, respectively. At the shear rate of  $150 \text{ s}^{-1}$  the viscosity of the two fluids are not similar indeed, the viscosity of PEO 0,4 is lowered to 0,0128 Pa·s.



**Fig. 32** Shear viscosity  $\eta$  as a function of the shear rate  $\dot{\gamma}$  for PEO 0,5 (dark grey star), PEO 0,4 (black squares), PEO 0,3 (grey triangles), PEO 0,2 (black diamonds), PEO 0,1 (light grey circles). And Gly 70% (light grey line).

### 3.4 Preparation of the particle suspensions

To calibrate our microfluidics device, different fluorescent polystyrene particles (PSL) were investigated in flow, having a nominal diameter  $a_{nom}$  of 7.3, 9.9, 14.6

and 20.0  $\mu\text{m}$  (PSL7, PSL10, PSL15, PSL20 respectively), with green (Bangs Laboratories –  $a_{\text{nom-7}}$ ), orange (Invitrogen -  $a_{\text{nom-10}}$ ), red (Bangs Laboratories -  $a_{\text{nom-15}}$ ) and yellow (Polysciences –  $a_{\text{nom-20}}$ ) fluorescence, respectively.

The volume fractions of particles in the suspension were  $x_7 = 0.275$ ,  $x_{10} = 0.275$ ,  $x_{15} = 0.45$ ,  $x_{20} = 0.275$ . PSL were sonicated for 5 minutes and vortexed for 30 seconds before each measurement to assure the absence of particle agglomerates.

### ***3.5 Blood separation***

#### ***3.5.1 Peripheral blood mononuclear cell collection***

Peripheral blood mononuclear cells (PBMC) have been extracted from fresh whole blood according to a self-made protocol starting from standard density gradient centrifugation. Such a principle is widely used in routinely hematologic procedure to enrich blood cell population out from fresh blood samples [127]. For lymphocytes and monocytes extraction a neutral, high-mass and hydrophilic polysaccharide having a density of 1.077 g/dL is used, called Ficoll (Sigma Aldrich). Blood separation on Ficoll gives the opportunity to perform a separation between PBMC (corresponding to the a-granulocytic population, i.e lymphocytes and monocytes) and cells with polymorphic nucleus, i.e. granulocytic populations. This method has a significant drawback, because of the high platelet contamination can be found after the separation. Platelets, in fact, have a density like the one of a-granulocyte cells, resulting in a similar behaviour when centrifuged at a density separation. In general, many platelets can be found in the collected sample of PBMC [128], [129]. Platelets presence generates non-homogeneity of the extracted population, resulting in a non-pure collection sample. Due to their small diameters, in fact, platelets can produce a widespread background signal. Following instructions represent the final protocol used for the PBMC collection.

A minimum of 12 mL of human blood samples from healthy adult donors were withdrawn with a standard venepuncture procedure. All samples were taken after

obtaining informed consent from all donors, or their legal guardians in accordance with relevant guidelines and regulations. The experimental protocol was approved by a licensing committee (EU clinical trial register - EudraCT Number: 2007-004270-43). All patients gave informed consent to publish identifying information. All blood samples were stored in standard, K2EDTA tubes (BD Vacutainer) to prevent coagulation. Within 1 hour from collecting, the blood sample is treated for the cell extraction. The whole blood volume is diluted with PBS medium in 1:1 proportion and gently laid on a volume of density gradient media equal to the volume of blood (see Fig. 33a). It is very important, at this step, not to mix density media and blood sample. If this happens, extraction yield is severely compromised.

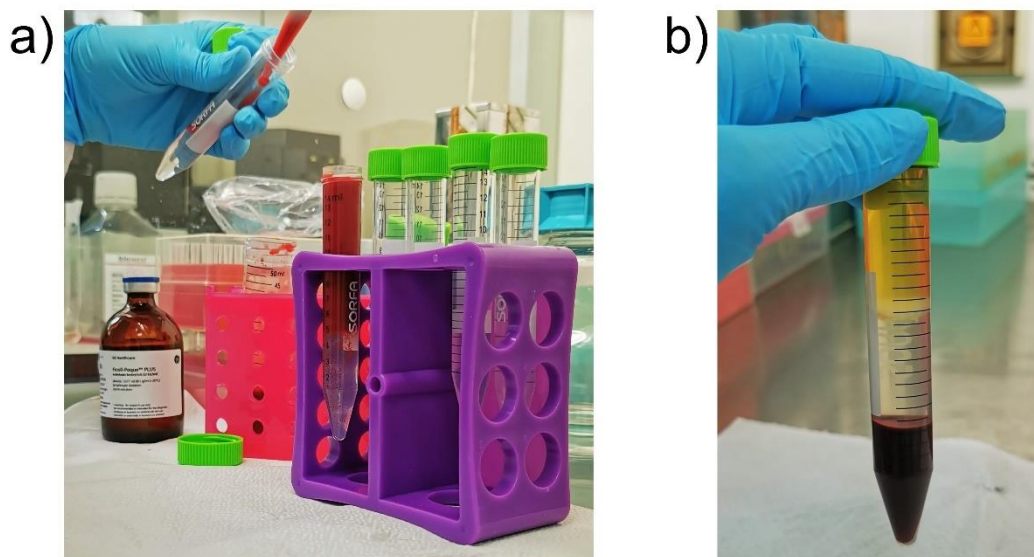


**Fig. 33** a) The whole blood volume is diluted with PBS medium in 1:1 proportion and gently laid on a volume of density gradient media equal to the volume of blood. b) blood sample after centrifugation, it is possible distinguish at the bottom of the tube all the RBC, at the upper part plasma and at the interface between Ficoll and plasma a ring containing all the PBMC.

Afterwards, the sample is centrifuged for 30 minutes,  $200 \vec{g}$  using minimum acceleration and no machine brake. It has been noted that low spin velocity to  $200 \vec{g}$  instead of the generally used  $600 \vec{g}$  founded in literature, helps to increase purity of the separation, reducing platelet presence in the final sample. Slowing down the

spinning velocity also significantly decreases the final number of recovered PBMC [130]. After this centrifugation step, the blood sample is found to be separated in four different zones. At the bottom of the tube all the RBC are present. Above them is laid the density media and the plasma. At the interface between Ficoll and plasma a ring containing all the PBMC is present (see Fig. 33b).

The upper plasma is gently removed from the sample. Afterwards, the PBMC ring is collected using a plastic pasteur and transferred to a new tube. The obtained PBMC are washed in a self-made RBC lysis solution, to eliminate possible RBC contamination.

RBC contamination can occur when overlaying of blood sample on Ficoll density media generates some mixing and, in general, is not properly performed. It can also depend on RBC anomalous high concentrations, infection status or generic plasma disorder. RBC lysis solution is made as follow:

- 155 mM NH<sub>4</sub>Cl
- 10 mM KHCO<sub>3</sub>
- 0.1 mM EDTA

The washed cells are centrifuged for 10 minutes, 200  $\bar{g}$  and the supernatant is discarded. As last step the collected PBMC are then resuspended in a desired volume of PBS, ready to be used. Depending on the results, nevertheless, additional step of purification can be added.

### ***3.5.2 Lymphocytes and monocytes collection***

According to cell class needing, several protocols can be used to select and isolate a single cell population. For lymphocytes: B- and T-lymphocytes isolation through selective adhesion of monocytes. After isolation, PBMC can be resuspended in standard Roswell Park Memorial Institute medium (RPMI- 1640, SIGMA ALDRICH) supplemented with 1% of penicillin/streptomycin and 10% of fetal bovine serum (FBS). RPMI-1640 with penicillin/streptomycin and 10% of fetal bovine serum (FBS) is defined as "complete RPMI". Cells are placed in an incubator

at 37°C, 5% of CO<sub>2</sub>. After 24 hours, monocytes adhere on the surface of the plastic plate, while lymphocytes remain in the RPMI-1640 solution. Such a way it is possible to select lymphocytes and/or monocytes from the whole PBMC sample. Monocytes negative selection through magnetic beads is a method by which cells are attached on the surface of magnetic beads (Dynabeads Magnetic Separation Technology - INVITROGEN) thanks to the interaction with specific membrane Ab. This attachment permits to selectively retain cells of interest using a magnetic structure in which the sample tube is accommodated. Magnetic beads selection can be "positive" or "negative". A positive selection is performed when cells are retained by beads surfaces and then released on the final solution, in which cells of interest as well as magnetic beads are present. A negative selection is performed when all the unwanted cells are retained by magnetic beads and then discarded. Protocol of negative selection for monocytes follows: PBMC collected are resuspended in a specific isolation buffer (IB, made of PBS, FBS 2%, EDTA 2:0 mM), and an antibody mix is added. Antibody mix for negative selection is composed of Ab selectively recognizing all the unwanted cells of the PBMC pool. Monocytes are bound by Ab anti-CD 14; Ab mix for monocities negative selection is made of CD 3 and CD 19. After incubation at 4°C for 20 minutes, cells are washed with IB and then centrifuged, in order to discard the supernatant filled with unwanted debris. Magnetic beads are added, the sample is well mixed and incubated at room temperature for 20 minutes. After cells are attached to the beads, tube is placed between the magnets for 2 minutes to permits the retaining on the tube surfaces of the beads attached to the unwanted cells. Desired untouched cells are collected, washed with IB and resuspended in a desired volume of measurement medium.

### ***3.5.3 RBC and neutrophils collection***

The neutrophils (Neutr) isolation was performed using the same sample for PBMC collection: the bottom layer obtained from centrifugation, containing RBC and

neutrophils, was diluted with a 10mL of RBC lysis solution. This step was repeated until RBC were completely absent (typically 2-3 times). RBC were available immediately after blood collection: some microliters of pure blood (containing 99% of RBC) were directly diluted in PEO solution and ready to test RBC.

### ***3.6 Preparation of the blood cell suspensions***

To evaluate first the single cell position in the expansion region of our microfluidic device a cell sample with only one type of cell was used. In each possible cell type case the concentration of cells in the measurement sample was circa  $2 \times 10^4$  cell/ml. Such a cell concentration was chosen low to avoid possible particle-particle interaction during the experimental measurements. Furthermore, two different mixture of cell types were prepared to investigate the separation performance of our microfluidic device. The first mixture MIX1 is composed from neutrophils and RBC (where neutrophils were stained with a unique nuclear dye HOECHST 488), while the second mixture MIX2 is composed from monocytes cell/ml and lymphocytes  $2 \times 10^4$  cell/ml (where monocytes were stained with a unique nuclear dye HOECHST 488).

### ***3.7 Other cell lines***

We investigated MCF-10A (MCF10a), MCF-7 (MCF7) and MDA-MB-231 (MDA) cell lines, where MCF-10A was donated by S. Piccolo (Istituto FIRC di Oncologia Molecolare, IFOM, Milan, Italy) and cultured in the mammary epithelial basal medium (MEBM) supplemented with the mammary epithelial growth media (MEGM) BulletKit (Lonza). The MCF-7 and MDA-MB-231 cell lines were kindly donated by Daidone's group and Dr P.F. Cammarata (Institute of Molecular Bioimaging and Physiology, IBFM-CNR, Cefalù (PA), Italy), respectively. The MCF-7 cells were cultured in Eagle's minimum essential medium (EMEM, Sigma-

Aldrich) containing 10% FBS, 100  $\mu\text{g ml}^{-1}$  L- glutamine and 100 U  $\text{ml}^{-1}$  penicillin/streptomycin. The MDA-MB-231 cells were cultured in a 1:1 mixture of Dulbecco's modified essential medium (DMEM, Euroclone) and Ham's F-12 medium (Microtech) supplemented with 10% FBS, 1% non-essential amino acid mixture and 100 U  $\text{ml}^{-1}$  penicillin/streptomycin. Finally, each investigated cell line is diluted in 1000  $\mu\text{l}$  of viscoelastic medium to reach a final cell concentration of circa  $2 \times 10^4$  cells per ml. In Fig. 35, the distribution of diameters of MCF7, MDA and MCF10a is showed.

### ***3.8 Brightfield microscopy observations***

Brightfield microscopy (BMF) has been widely used in this work, to establish experimental parameters like cell size, for instance. An inverted microscope (IX81, OLYMPUS) has been used to evaluate cell migration and alignment in flow using a 10X or 20X objective, while for cell size investigations in quiescent condition a 100X oil immersion objective has been used. Optical resolution of images allowed us to evaluate morphological cell shape and vitality. Sufficiently detailed membrane structures are visible, assuring us no damage on the cell surface (see Fig. 34).

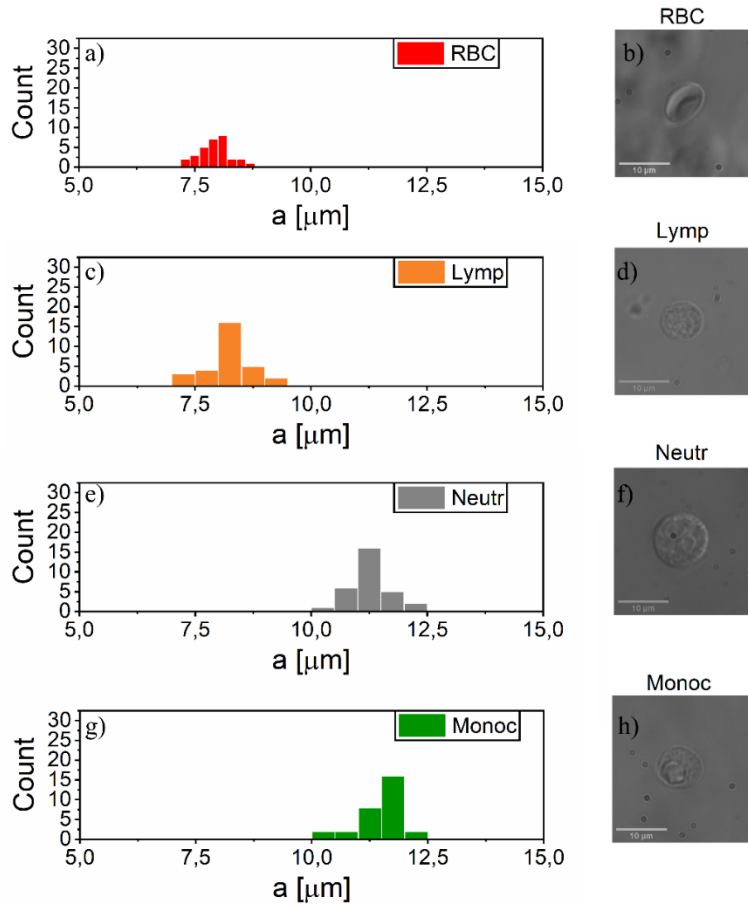


**Fig. 34** Cell diameter distributions and image in brightfield of a),b) RBC c),d) Lymp and e),f) Neutr and g),h) Monoc, respectively.

In Fig. 34 an image of Lymp, Monoc, Neutr and RBC is showed. In Fig. 35a,c,e the diameter distribution of MCF7, MDA and MCF10a is showed with an image in brightfield.

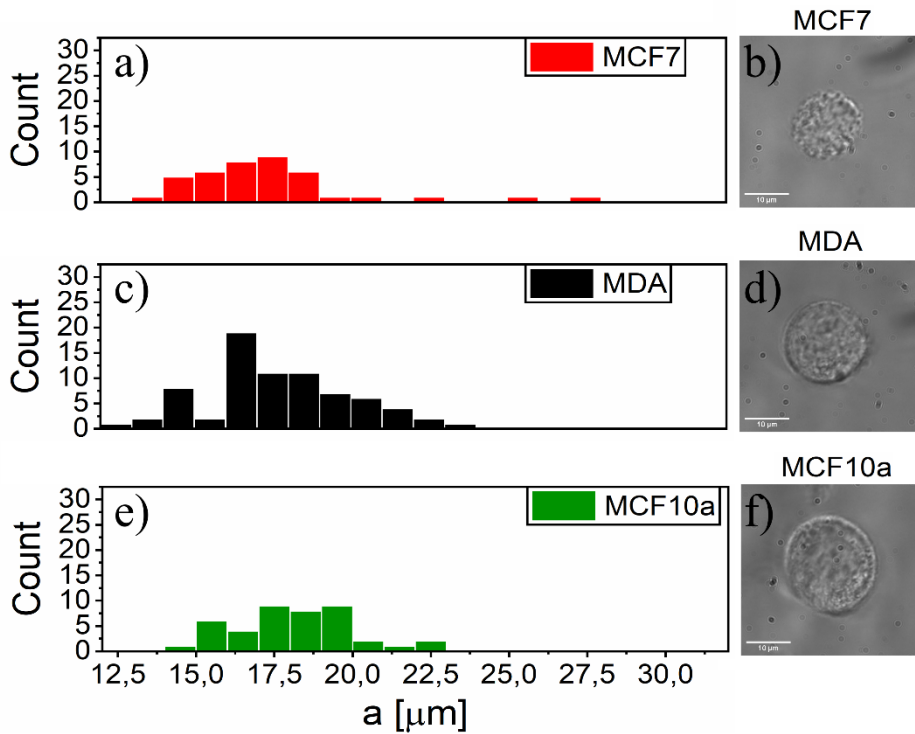


**Fig. 35** Cell diameter distributions and image in brightfield of a),b) MCF7 c),d) MDA and e),f) MCF10a, respectively.

### 3.9 Experimental setup and data analysis

The particle or cell suspensions are added in a vial and the vial is added in pressure chamber of pressure pump. The particles flowing in the microfluidic device were observed using fluorescent microscope combined with a CMOS Camera (Olympus - X81 and Hamamtsu - Orca Flash 4.0 with  $6.5 \mu\text{m}/\text{px}$ ,  $1 \text{ ms} < \text{ET} < 4 \text{ ms}$ ,  $20 < \text{fps} < 300$  depending on flow rate). From the recorded videos, particle positions were monitored using a self-written MATLAB (Mathworks Inc.) routine in  $C_B$  (Fig.24 red square), in  $C_C$  at different distances  $L_x = 0\text{mm}, 5\text{mm}, 15\text{mm}$  and  $25\text{mm}$  from the bifurcation and in  $C_D$  (Fig.24 red square). In Fig. 36 a picture of microfluidic setup-up is showed.

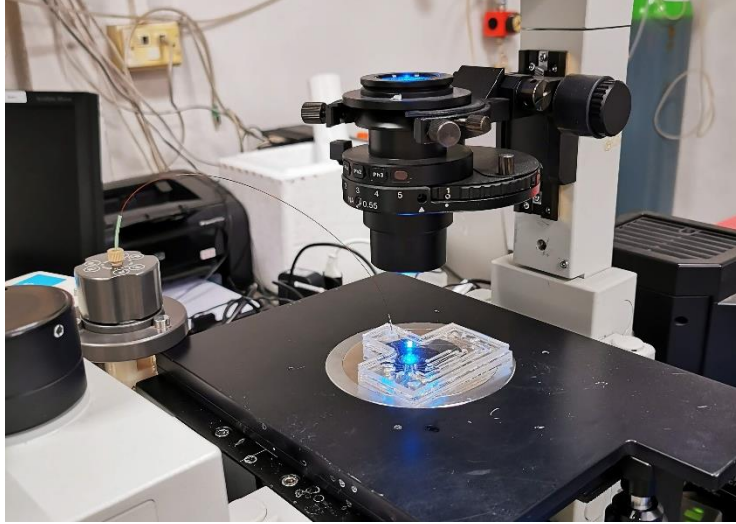


**Fig. 36** Photo of microfluidic setup.

The capillary was connected to a pressure pump (DOLOMITE - P-pump), operating in the range of pressure drops  $150 < \Delta p < 3200$  mbar, the relation between the flow rate and the pressure drop in a straight tube can be written as:

$$\Delta p = R_{tot}Q \quad \text{Eq. 3.9-1}$$

Where the  $R_r$  is the *hydraulic resistance for rectangular channel cross-section*:

$$R_r = \frac{12\eta L}{1 - 0.63 \frac{H}{W}} \left[ \frac{1}{H^3 W} \right] \quad \text{Eq. 3.9-2}$$

while for circular channel cross-section:

$$R_c = \frac{8}{\pi} \eta L \frac{1}{a^4} \quad \text{Eq. 3.9-3}$$

Then using the conservation of flow-rate we can assume that for two straight channels in parallel the resistance is given by:

$$R_{12} = \frac{R_1 R_2}{R_1 + R_2} \quad \text{Eq. 3.9-4}$$

While for two straight channels in series the resistance is given by:

$$R_{12} = R_1 + R_2 \quad \text{Eq. 3.9-5}$$

The experimental setup employed here was made of:  $C_C$  in series with  $C_D$  (called  $C_{CD}$ ), two parallel  $C_{CD}$  in series with  $C_B$  and  $C_A$ , therefore, the total resistance was given by:

$$R_{CD} = R_C + R_D \quad R_{eqCD} = \frac{R_{CD}R_{CD}}{R_{CD}+R_{CD}} \quad Eq. 3.9-6$$

$$R_{tot} = R_A + R_B + R_{eqCD} \quad Eq. 3.9-7$$

where  $R_A$  is the resistance of circular channel  $C_A$ ,  $R_B, R_C, R_D$  and  $R_{CD}$  are the resistances of rectangular channels  $C_B, C_C, C_D$  and  $C_{CD}$ , respectively.

Since the flow rate  $Q$  is constant it is possible to write:

$$Q = \frac{\Delta p}{R_{tot}} \quad Eq. 3.9-8$$

for our measurements we assume that particle and fluid velocities at the centerline are equal.

Non-dimensional numbers,  $Re$  and  $Wi$ , were calculated in the fully developed flow region of  $C_B$  (see sec. 4.1).

The fluid flow is represented in Fig. 37 along the  $x$  axis, while the lateral displacement in  $C_C$  and in  $C_D$  are represented along the  $y$  axis. The lateral displacement ( $L_p$ ) is defined as the distance between wall<sub>1</sub> and particle centre (Fig. 37).

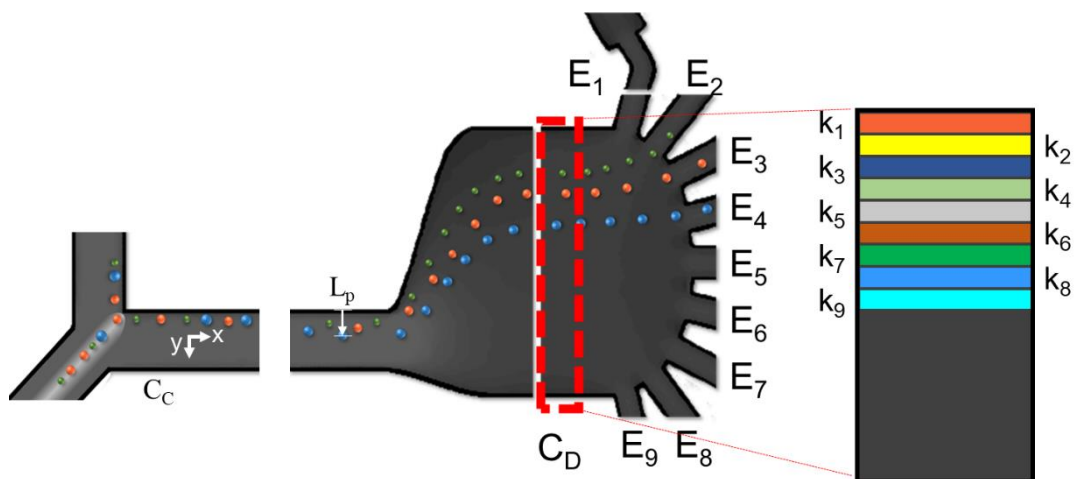


**Fig. 37** Schematic configuration of microfluidic device, in which definition of lateral displacement  $L_p$  and the division of  $C_D$  in bands are showed ( $k_1, \dots, k_9$ ).

Videos were collected and analysed by a MATLAB routine to track and investigate  $L_p$  of particles and cells in flow and to obtain particle dimension. To quantify the particle position, we divide half  $C_D$  in 18 bands of 50  $\mu\text{m}$  width and evaluate the fraction of particles passing in a specific band ( in Fig. 37 are showed only 9 bands for simplicity).

Our self-written routine, apply a bandpass filter to suppress pixel noise, then recorded grayscale images from the camera sensor were converted into binary image to identify round shaped object coordinates in-flow and we have considered the coordinate  $y$  as lateral displacement of particle or cell. From the recorded videos, maximum particle velocities at the center of  $C_B$  (Fig. 3B red square) and measurement efficiency ( $E$ ) at the output of the device were measured using Image-J and using MATLAB routine, respectively. In particular, we carried out the ratio between the number of target cells collected in one specific channel output  $C_E$  with the total number of target cells collected in all  $C_E$  outputs.

$$E = \frac{N_{j,i}}{\sum_i N_{j,i}} \quad \text{Eq. 3.9-9}$$

Where  $i$  is the counter of the exits, while  $j$  is the counter of cells or particles. Purity, on the other hand, has been defined as the ratio of the number of target cells in a certain output and the total number of cells collected in that output.

$$P = \frac{N_{j,i}}{\sum_j N_{j,i}} \quad \text{Eq. 3.9-10}$$

The experiments conducted for each type of sample is repeated for three times.

### ***3.10 Droplet generation***

#### ***3.10.1 Materials***

We used acrylamide  $\geq 99\%$  (Aam) and N,N'-methylene bis acrylamide (BIS)  $\geq 99\%$  powder, light mineral oil (LMO), Spans 80, Polyethylene glycol sorbitan monolaurate (TWEEN 20), ethanol and diethyl ether, Atto 488 maleimide (ATTO)

( $\lambda_{\text{ex}}$  501 nm;  $\lambda_{\text{em}}$  523 nm in 0.1 M phosphate pH 7.0) (purchased from SIGMA ALDRICH). Furthermore, we used a crosslinking reagent 2-Hydroxy-2-methylpropiophenone (DAROCUR 1173) for the droplet generation (purchased from CIBA). We prepared two stock solution, 40% *wt%* and 2% *wt%* respectively of Aam and BIS.

### ***3.10.2 Synthesis of hydrogel***

Polyacrylamide (PA) gels are three-dimensional networks of acrylamide reacted with the bifunctional reagent BIS via a free-radical initiated vinyl polymerization mechanism. The polymerization reaction creates a gel because of the added BIS, which form cross-links between two acrylamide molecules. One of the advantages of polyacrylamide gels is that they are biologically inert. As a result, we can tune the stiffness of PA gels by adjusting the concentrations of Aam and BIS, which affects the density of the PA network, but does not influence the biochemical property of the gels itself. By varying the concentrations of acrylamide and bisacrylamide, the range of stiffness can cover that of most soft human tissues.[131] The bulk-hydrogels were synthesized using a UV free radical photopolymerization. The process involves three basic steps.

First, a free radical must be formed through the initiation step. For the Aam-BIS system used in this work, the initiator is DAROCUR, which forms a free radical under UV light. The next step is known as propagation, where the free radical from the initiator meets the end of an Aam molecule and reacts with the carbon-carbon double bond in the acrylate functional group. This step produces a second free radical species, which can go on to react with more AAm polymers propagating the crosslink. The final step in the process of this polymerization is the termination of the crosslinking, which occurs when two radical species meet and a bond form between them. Different pre-gel solutions were prepared by varying the total monomer concentration  $C_T$  defined as:

$$C_T = \frac{AAm (g) + BIS (g)}{\text{total volume (mL)}} 100\% \quad \text{Eq. 3.10-1}$$

Ranging from 5.9 to 11.8%, but maintaining the cross-linker to monomer ratio concentration C:

$$C = \frac{BIS (g)}{Aam (g) + BIS (g)} \quad \text{Eq. 3.10-2}$$

constant at C = 3.25%.

### **3.10.3 Rheological characterization**

Rheological characterization of hydrogels was carried out in order to calculate the Young modulus of hydrogel polymer at different concentrations. The mechanical properties of PA substrates were evaluated by small-amplitude oscillatory shear experiments that allowed measurement of the response of the samples and hence of their linear viscoelastic properties [132]. The tests were performed by using a stress-controlled rheometer (MCR 302, ANTON PAAR) equipped with a parallel plate geometry (25 mm of diameter). Dynamic frequency sweeps were performed in a range of frequency of  $10^{-1}$ -10 Hz with strain amplitude of 0,1. PA gels were attached to slide (MENZEL GmbH) of 25 mm of diameter. The slides were placed on a hot plate (50–60 °C), covered with 500  $\mu$ L of 0.1 mM NaOH. After evaporation, NaOH solution formed a thin semitransparent film on the slides. Next, 250  $\mu$ L of 3-aminopropyltriethoxysilane (APTES - 440140, SIGMA ALDRICH) was added to the slides in the fume hood for 10 min. The slides were rinsed with distilled water at least three times for 5 min each, until the unreacted APTES was completely removed. The slides were covered with 0.5% glutaraldehyde (AGAR SCIENTIFIC, R1020) solution in PBS for 30 min. The slides were extensively washed with distilled water and air-dried. Different combinations of Aam and BIS-Aam were used to obtain different mechanical properties (from 17 kPa to 120 kPa).

400  $\mu$ l of Aam/BIS-ATTO ( $C_T$  11,8%,15% and 20% with 0,1mM ATTO) mixture were pipetted on the treated slid and another treated slide was placed upper the drop

to reach circa a 1 mm of sample thickness. The gel was polymerized for 15 min with an UV lamp Fig. 38.

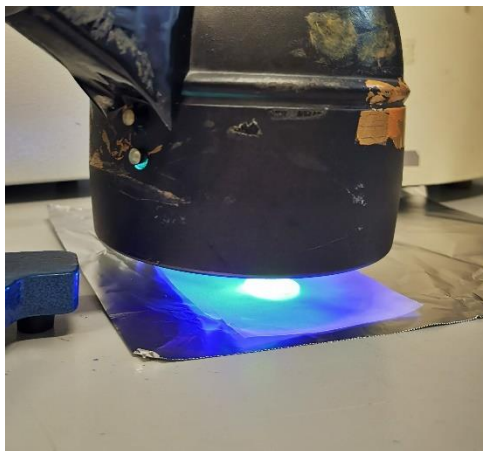


*Fig. 38 PA bulk polymerization under UV lamp.*

### ***3.10.4 Synthesis of functionalized microparticles***

Microparticles were synthesized using a microfluidic device for droplet generation bought from ELVEFLOW. The chip is a PDMS microfluidic device, which was designed for generating droplets with T-junction geometry. It consists of two inputs for the continuous and disperse phase, a narrow orifice where the two opposite channels converge, and an output (Fig. 40a). The dimensions of the channels are  $50\mu\text{m} \times 250\mu\text{m}$  (height  $\times$  width) and  $50\mu\text{m} \times 50\mu\text{m}$  (height  $\times$  width) for continuous phase channel and dispersed phase channel respectively, while the channel cross-section at junction is of  $50\mu\text{m} \times 30\mu\text{m}$  (height  $\times$  width) (Fig. 40b).

Microparticles were synthesized using LMO containing non-ionic surfactant Span 80 (5 v/v%) as a continuous phase and a water solution of Aam and BIS (11.8-15-20 wt% with photoinitiator darocur (0.5-1% v/v with respect to the total volume) as dispersed phase. In order to functionalize microparticles, ATTO maleimide was added in the dispersed phase to reach final concentration of 0.1mM into the water solution. The outlet tube passed through a closed tube in which a lamp UV (365 nm

wavelength at 2 power conditions: power lamp at 50% or 100%) were focused to polymerize the produced microgel. The distance between the UV source and the outlet tube was set to 2 cm, and the exposure time of each particle to UV light, depending on the imposed flow rates (6.5  $\mu\text{L}/\text{min}$  for the continuous phase, 0.5  $\mu\text{L}/\text{min}$  for the dispersed phase), was calculated to be circa 2.5 minutes. In Fig. 40b was reported our experimental set-up. Droplet emulsions were obtained adding in the first channel water solution and continuous phase in the other. Solutions were injected using a pressure pumps (ELVEFLOW Ob1 MK3+) to ensure stable flow and reproducibility. The outlet tube pass through a black iron tube in which UV-lamp (X-CITE 120PC Q) consent a particles polymerization (Fig. 40a). Afterwards, microparticles were collected in an Eppendorf tube and the exceeded oil phase was removed. Then particles were washed several times with different solvents (diethyl ether, ethanol and milliQ water-tween solution (0.05  $v/v\%$ )) to remove the residual oil. In Fig. 39 we show the diameter distribution of particles with 11,8%  $C_T$  and 0,1 mM ATTO (AAm 11,8%) and 15 %  $C_T$  and 0,1 mM ATTO(AAm15%), and fluorescence images of particle in water.

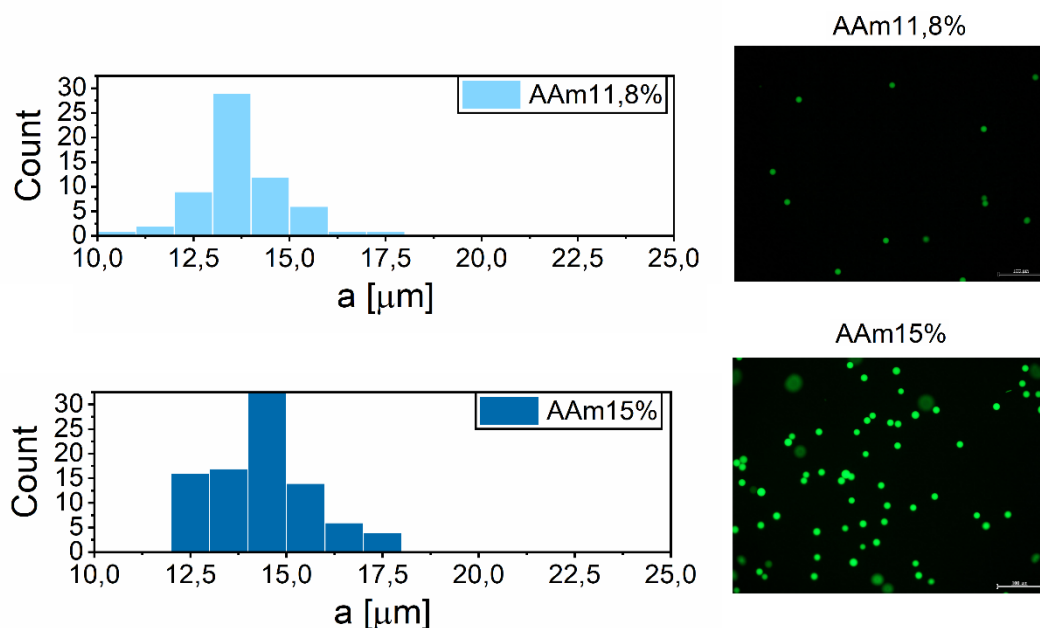


**Fig. 39** Diameter distribution of PA particles with two  $C_T$  concentration up 11,8% and down 15%.

After washing, microgels were stored at room temperature in buffer solutions until further use. This system was mounted on a straight microscope (BX 63 Olympus). The droplets formation was monitored using an objective with 4x magnification and recorded with a CCD camera THORLAB CS235MU that allow to record up to 40 frame per second.

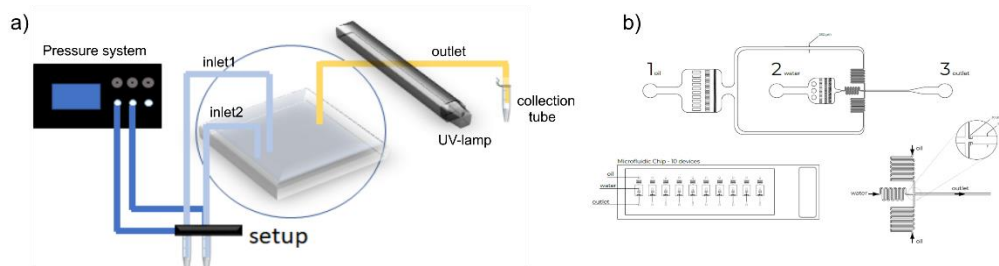


**Fig. 40** a) Schematic representation of microfluidic setup for droplet generation. b) schematic representation of microfluidic device for droplet generation.

### 3.10.5 Flow data collection and analysis

Droplet formation process was recorded and then analysed with ImageJ. Droplet size, frequency, spacing and velocity were measured at varying flow rates imposed. Fluorescence intensity was analysed with ImageJ and MATLAB routine.

### 3.10.6 Network properties of PA particles

Swelling characterization of hydrogels were carried out in order to calculate the volume fraction of cross-linked polymer in the equilibrium swollen gel (defined as the ratio of the most probable volume of a swollen particle to the volume per particle,  $v_2$ ). Therefore, we evaluated the particle diameter in flow ( $a_{oil}$ ) and particle diameter after swelling ( $a$ ) (swelling behavior is an intrinsic property of hydrogels, where the

microgels enlarge due to solvent penetration into the void space between the polymeric chain network). Then we calculate  $v_2$  as [133]:

$$v_2 = \frac{v_2^0}{V_{eq}} \quad \text{Eq. 3.10-3}$$

Where  $V_{eq} = (a/a_{oil})^3$  ( $a$  is the normalized volume of equilibrium swollen gel and  $v_2^0 = 10^{-3}C_0V_r$  is the volume fraction of crosslinked polymer after gel preparation,  $C_0$  is the initial monomer concentration and  $V_r = 52.6 \text{ ml mol}^{-1}$  is the molar volume of PA repeat units.[134] Eq. 3.10-4 predicts the molecular weight between crosslinks in a neutral hydrogel prepared in the presence of water ( $\bar{M}_c$ ):

$$\frac{1}{\bar{M}_c} = \frac{2}{\bar{M}_n} - \frac{\left(\frac{\bar{v}}{V_1}\right) [\ln(1 - v_2) + v_2 + \chi_1 v_2^2]}{(v_2^{1/3} - \frac{v_2}{2})} \quad \text{Eq. 3.10-4}$$

where  $\bar{M}_n$  is the molecular weight of the polymer chains prepared in the absence of a crosslinking agent,  $\chi_1$  is the polymer-solvent interaction parameter (0,494) [131],  $\bar{v}$  is the specific volume of the polymer, and  $V_1$  is the molar volume of water.

Since hydrogel is contained crosslinker, the molar mass of the polymer repeat unit,  $M_0$ , can be calculated by the following equation:

$$M_0 = \frac{n_{AAm} \times M_{AAm} + n_{CL} \times M_{CL}}{n_{AAm} + n_{CL}} \quad \text{Eq. 3.10-5}$$

Where  $n_{AAm}$  and  $n_{CL}$  are the mol number of Aam and BIS (mol) respectively, and  $M_{AAm}$  and  $M_{CL}$  are the molar mass of Aam and BIS respectively. Another important parameter of networks is gel pore size or mesh size ( $\xi$ ).[135] For determining this parameter, the end-to-end distance in the freely jointed state is determined as:

$$\bar{r}_f = l\sqrt{N} \quad \text{Eq. 3.10-6}$$

where  $l$  is the bond distance for C–C (1.54 Å) and the number of links,  $N = \lambda\bar{M}_c/M_0$  and  $\lambda = 2$ . The end-to-end distance in the unperturbed state is calculated through the characteristic ratio  $C_n = 6.32$ .

$$\bar{r}_0^2 = C_n \bar{r}_f^2 \quad \text{Eq. 3.10-7}$$

The end-to-end distance in the swollen state, equivalent to the mesh size,  $\xi$  (Å), is:

$$\xi = v_s^{-1/3} r_0 \quad \text{Eq. 3.10-8}$$

### 3.10.7 Swelling characterization

At first, we evaluated mass of bulk hydrogel measured in polymerizate, swollen and dry conditions. First, polymerized hydrogels were weighted ( $m_{\text{pol}}$ ) and then immersed in an excess of milli-Q water in order to remove the unreacted reagents. Afterwards, the water was changed several times for the next 24 h.. Resulting in a hydrogel swelling overnight at room temperature. As next step then bulk were gently wiped with a filter paper and weighted to obtain the mass of swollen hydrogel ( $m_{\text{swollen}}$ ). On the other side, in order to obtain a total dehydration of the sample, hydrogels were dehydrate in an oven at 40°C overnight, so the mass of dry samples were recovered ( $m_{\text{dry}}$ ) and subsequently weighted. Therefore, we were able to determine hydrogel bulk content of water in swollen state (mass fraction of water in the swollen condition,  $F_{\text{water}}$ ), using Eq. 3.10-9:

$$F_{\text{water}} = \frac{m_{\text{swollen}} - m_{\text{dry}}}{m_{\text{dry}}} \times 100 \quad \text{Eq. 3.10-9}$$

In the case of particles  $F_{\text{water}}$  is calculated from the diameter in dry conditions. Moreover, the percentage of swelling of PA particles, which represent the, were calculated using Eq. 3.10-10:

$$\% \text{swelling} = \frac{a - a_{\text{oil}}}{a_{\text{oil}}} \times 100 \quad \text{Eq. 3.10-10}$$

### 3.11 Holografy

A digital holography microscope (DHM) can generate, high resolution 3D digital images of a sample using the principle of holography. In such a case hologram are generated by combining a coherent reference wave with the wave received from a cell or particle. They are recorded by a camera and transmitted to a computer for real-time numerical reconstruction. In such a case the DHM computes the complete

wavefront emanating from an object (cell in our case) and provides, intensity images and phase images. The obtained phase image directly reveals the surface topography with a sub-nanometric vertical resolution. In transmission, the phase image reveals the phase shift induced by a transparent cell, which can be interpreted in terms of many underlying biological processes. In particular, optical aberrations, digital image focusing, and numerical compensation for sample tilt and environmental disturbances can be performed with a DHM technique [136].

## 4 Results

Our microfluidic device was fabricated according to the design concept developed in section 3.1. First, we investigated the channel geometries after fabrication using an optical surface profilometer (Dektak 150, Veeco), which showed following channel geometries  $C_B$  W 200  $\mu\text{m}$  H 135  $\mu\text{m}$ ,  $C_{C,\text{up}}$  W 200  $\mu\text{m}$  H 136  $\mu\text{m}$ ,  $C_{C,\text{down}}$  W 200  $\mu\text{m}$  H 141  $\mu\text{m}$ ,  $C_{D,\text{up}}$  W 900  $\mu\text{m}$  H 142  $\mu\text{m}$ ,  $C_{D,\text{down}}$  W 900  $\mu\text{m}$  H 138  $\mu\text{m}$  (see Fig. 41).

The CC up and down have about 5  $\mu\text{m}$  of difference in height. Furthermore, we have analysed CC up and down at different distance (0mm, 10 mm and 20mm) from the bifurcation. The height of CC\_up and CC\_down is not constant long the channel indeed the height increases of about 3  $\mu\text{m}$  and 5  $\mu\text{m}$ , respectively.

However, surface analyses show very precise fabrication stability in vertical direction (channel height), while in horizontal direction (channel width) some imprecision can be noticed due to the profilometer tip geometry (2.5  $\mu\text{m}$  tip radius with 45° cone shape).

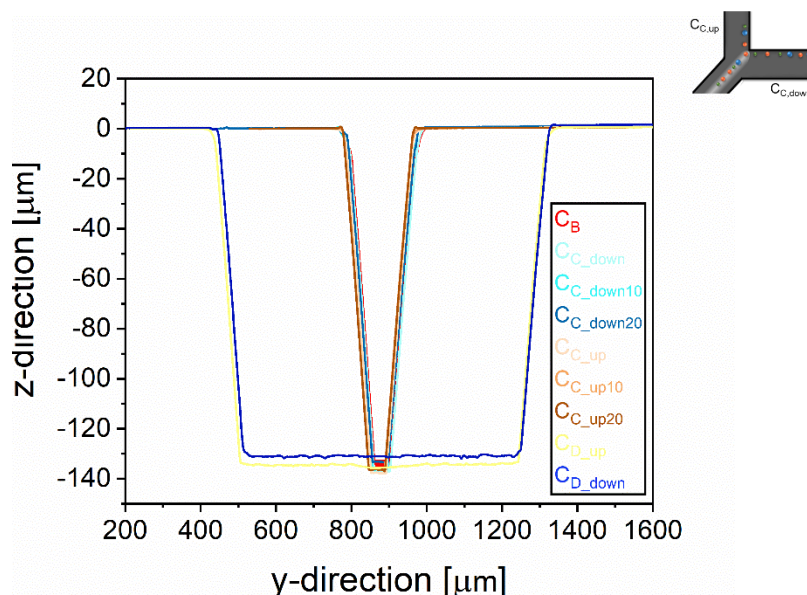


**Fig. 41** Optical surface profilometer (Dektak 150, Veeco) outcome of fabricated microfluidic chip sections. We designed the microfluidic sections of different nominal height and width ( $C_B=150 \times 200$ ,  $C_C=150 \times 200$ ,  $C_D=150 \times 900$ , respectively) and measured the sections at the beginning of each section in flow direction. Surface analyses show very precise fabrication stability in vertical direction (channel height), while in horizontal

direction (channel width) some imprecision can be noticed due to the profilometer tip geometry ( $2.5\ \mu\text{m}$  tip radius with  $45^\circ$  cone shape).

Next, we produced PDMS device as described in materials and methods section 3.2, assembled it with an input capillary and tested the device of possible fluid leakages. After intensive testing of device robustness with different applied fluid velocities and suspension fluids we started to test our fluid flow predictions with polystyrene particles (PSL) of different size.

#### 4.1 Device calibration and fluid flow testing

For simplicity, we reported the design of our microfluidic device in Fig. 42.

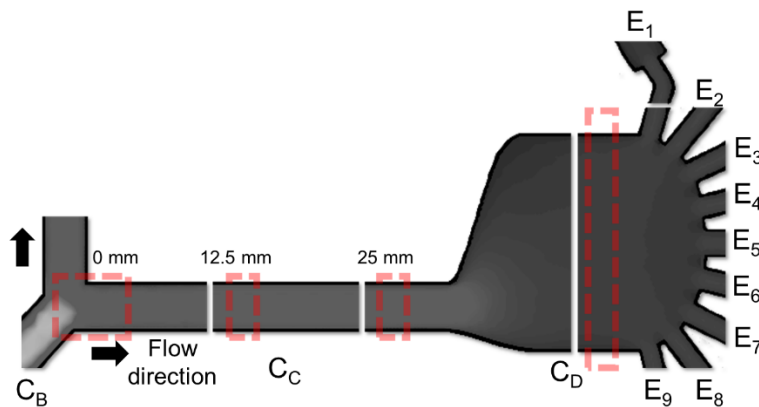


**Fig. 42** Schematic representation of microfluidic device, in red the zones the lateral displacements were analysed.

First, we measured the particle velocities in  $C_B$  section of our device and compared our outcomes with predictions shown in Table 3. Note that we used the maximum experimentally recorded particle velocity for comparisons because the particles are at the center of  $C_B$  and assume maximum velocity ( $V_{\max,B}$ ). Our first fluid investigations showed that the velocity measured are similar to that calculated so can assumed that particle and fluid velocities are equal.

**Table 3**  $V_{max,B}$  measured in  $C_B$  at different pressures applied in different PEO concentrations (PEO 0,2, PEO 0,3, PEO 0,4 and PEO 0,5).

<i>PEO 0,2</i>		<i>PEO 0,3</i>		<i>PEO 0,4</i>		<i>PEO 0,5</i>	
$\Delta P$	$V_{max,B}$						
[mbar]	[mm/s]	[mbar]	[mm/s]	[mbar]	[mm/s]	[mbar]	[mm/s]
150	12.0	200	10.7	370	9.2	600	9.3
200	15.7	370	14.0	620	15.4	1000	15.4
360	27.2	670	24.7	1000	25.2	1650	25.7
500	35.6	870	34.6	1500	37.1	2300	35.6
630	46.3	1240	47.0	2000	49.5	3200	49.5

Particles were observed for varying inlet pressure ( $\Delta P$ ) of the microfluidic device, with values ranging from 150 to 3200 mbar and PEO ranging from 0,2 to 0,5 wt%.

Such pressure variations correspond to different fluid velocities depending on the used rheological fluid properties. In Table 4 (PEO 0,2 wt%), Table 5 (PEO 0,3 wt%),

Table 6 (PEO 0,4 wt%) and Table 7 (PEO 0,5 wt%) the applied inlet pressure and corresponding average channel section velocities ( $V_{media}$ ), maximum channel section velocity ( $V_{max}$ ), calculated Re (using Eq. 2.1-1), Wi (using Eq. 2.1-4) and El (using Eq. 2.1-6) are reported for all microfluidic sections of our device. Afterwards, we investigated particle positions in  $C_D$  at the right side of the bifurcation. In more detail, the lateral displacement of particles (from wall<sub>1</sub> to wall<sub>2</sub>, see Fig. 25 in y-direction) for PSL7, PSL10, PSL15 and PSL20  $\mu m$ .

**Table 4** Pressure ( $\Delta P$ ) applied at the inlet of the microfluidic device correlates with average velocity ( $V_{\text{media}}$ ), maximum velocity ( $V_{\text{max}}$ ),  $Re$ ,  $Wi$  and  $El$  for channel  $C_A$ ,  $C_B$ ,  $C_C$  using PEO 0,2 is shown.

<i>Peo0.2</i>						
$\Delta P$ [mbar]	Channel	$V_{\text{media}}$ [mm/s]	$V_{\text{max}}$ [mm/s]	$Re$	$Wi$	$El$
150	$C_A$	5.95	11.91	1.72E-01	5.16E-03	2.99E-02
	$C_B$	5.53	11.07	1.25E-01	6.90E-03	5.50E-02
	$C_C$	1.75	3.50	5.28E-02	1.38E-03	2.62E-02
200	$C_A$	7.94	15.88	2.30E-01	6.88E-03	2.99E-02
	$C_B$	7.38	14.76	1.67E-01	9.20E-03	5.50E-02
	$C_C$	2.34	4.67	7.05E-02	1.85E-03	2.62E-02
360	$C_A$	14.29	28.58	4.14E-01	1.24E-02	2.99E-02
	$C_B$	13.28	26.56	3.01E-01	1.66E-02	5.50E-02
	$C_C$	4.21	8.41	1.27E-01	3.32E-03	2.62E-02
500	$C_A$	19.84	39.69	5.74E-01	1.72E-02	2.99E-02
	$C_B$	18.45	36.89	4.18E-01	2.30E-02	5.50E-02
	$C_C$	5.84	11.68	1.76E-01	4.61E-03	2.62E-02
630	$C_A$	25.00	50.01	7.24E-01	2.17E-02	2.99E-02
	$C_B$	23.24	46.49	5.27E-01	2.90E-02	5.50E-02
	$C_C$	7.36	14.72	2.22E-01	5.81E-03	2.62E-02

**Table 5** Pressure applied at the inlet of microfluidic device correlates with average velocity, max velocity,  $Re$ ,  $Wi$  and  $El$  for channel  $C_A$ ,  $C_B$ ,  $C_C$  using PEO 0,3.

<i>Peo0.3</i>						
$\Delta P$ [mbar]	Channel	$V_{\text{media}}$ [mm/s]	$V_{\text{max}}$ [mm/s]	$Re$	$Wi$	$El$
260	$C_A$	5.28	10.57	7.83E-02	9.05E-03	1.16E-01
	$C_B$	4.91	9.82	5.72E-02	1.22E-02	2.13E-01
	$C_C$	1.56	3.11	2.41E-02	2.44E-03	1.01E-01
370	$C_A$	7.52	15.04	7.83E-02	9.05E-03	1.16E-01
	$C_B$	6.99	13.98	5.72E-02	1.22E-02	2.13E-01
	$C_C$	2.21	4.43	2.41E-02	2.44E-03	1.01E-01
670	$C_A$	13.61	27.23	2.02E-01	2.33E-02	1.16E-01
	$C_B$	12.66	25.31	1.47E-01	3.13E-02	2.13E-01
	$C_C$	4.01	8.01	6.21E-02	6.28E-03	1.01E-01
870	$C_A$	17.68	35.35	2.62E-01	3.03E-02	1.16E-01
	$C_B$	16.43	32.87	1.91E-01	4.07E-02	2.13E-01
	$C_C$	5.20	10.41	8.06E-02	8.16E-03	1.01E-01
1240	$C_A$	25.20	50.39	3.73E-01	4.32E-02	1.16E-01
	$C_B$	23.42	46.84	2.73E-01	5.80E-02	2.13E-01
	$C_C$	7.42	14.83	1.15E-01	1.16E-02	1.01E-01

**Table 6** Pressure applied at the inlet of microfluidic device correlates with average velocity, max velocity,  $Re$ ,  $Wi$  and  $El$  for channel  $C_A$ ,  $C_B$ ,  $C_C$  using PEO 0,4.

<i>Peo0.4</i>						
$\Delta P$ [mbar]	Channel	$V_{media}$ [mm/s]	$V_{max}$ [mm/s]	$Re$	$Wi$	$El$
370	$C_A$	4.93	9.85	4.78E-02	1.27E-02	2.65E-01
	$C_B$	4.58	9.16	3.50E-02	1.71E-02	4.87E-01
	$C_C$	1.45	2.90	1.48E-02	3.42E-03	2.32E-01
620	$C_A$	8.25	16.51	8.01E-02	2.12E-02	2.65E-01
	$C_B$	7.67	15.35	5.87E-02	2.86E-02	4.87E-01
	$C_C$	2.43	4.86	2.47E-02	5.73E-03	2.32E-01
1000	$C_A$	13.31	26.62	1.29E-01	3.42E-02	2.65E-01
	$C_B$	12.38	24.75	9.47E-02	4.61E-02	4.87E-01
	$C_C$	3.92	7.84	3.99E-02	9.25E-03	2.32E-01
1500	$C_A$	19.97	39.94	1.94E-01	5.14E-02	2.65E-01
	$C_B$	18.56	37.13	1.42E-01	6.92E-02	4.87E-01
	$C_C$	5.88	11.76	5.98E-02	1.39E-02	2.32E-01
2000	$C_A$	26.62	53.25	2.59E-01	5.14E-02	2.65E-01
	$C_B$	24.75	49.50	1.89E-01	6.92E-02	4.87E-01
	$C_C$	7.84	15.68	7.98E-02	1.39E-02	2.32E-01

**Table 7** Pressure applied at the inlet of microfluidic device correlates with average velocity, max velocity,  $Re$ ,  $Wi$  and  $El$  for channel  $C_A$ ,  $C_B$ ,  $C_C$  using PEO 0,5.

<i>Peo0.5</i>						
$\Delta P$ [mbar]	Channel	$V_{media}$ [mm/s]	$V_{max}$ [mm/s]	$Re$	$Wi$	$El$
600	$C_A$	4.98	9.96	3.01E-02	2.06E-02	6.82E-01
	$C_B$	4.63	9.26	2.21E-02	2.78E-02	1.25E+00
	$C_C$	1.47	2.93	9.33E-03	5.57E-03	5.97E-01
1000	$C_A$	8.30	16.60	5.02E-02	3.43E-02	6.82E-01
	$C_B$	7.71	15.43	3.69E-02	4.63E-02	1.25E+00
	$C_C$	2.44	4.89	1.56E-02	9.28E-03	5.97E-01
1650	$C_A$	13.69	27.38	8.29E-02	5.65E-02	6.82E-01
	$C_B$	12.73	25.45	6.09E-02	7.64E-02	1.25E+00
	$C_C$	4.03	8.06	2.57E-02	1.53E-02	5.97E-01
2300	$C_A$	19.08	38.17	1.15E-01	7.88E-02	6.82E-01
	$C_B$	17.74	35.48	8.49E-02	1.06E-01	1.25E+00
	$C_C$	5.62	11.24	3.58E-02	2.13E-02	5.97E-01
3200	$C_A$	26.55	53.10	1.61E-01	1.10E-01	6.82E-01
	$C_B$	24.68	49.37	1.18E-01	1.48E-01	1.25E+00
	$C_C$	7.82	15.63	4.98E-02	2.97E-02	5.97E-01

Fig. 43 shows the mean value of the  $L_p$  of the previously mentioned PSL particles regarding different max velocities. Note that the indicated velocities are referred to the max velocity in  $C_B$ ,  $V_{\max,B}$ ). In more detail, PEO 0,2 wt% is shown in Fig. 43a, PEO 0,3 wt% is shown in Fig. 43b, PEO 0,4 wt% is shown in Fig. 43c, while PEO 0,5 wt% is shown in Fig. 43d). As already mentioned, the particle position in a microfluidic device is strongly influenced by the particle size, since the viscoelastic force acting on a particle depends on  $a^3$  (show in Eq. 2.2-3). In fact, in all fluid flow conditions PSL20 showed a higher lateral displacement from the wall<sub>1</sub> than smaller particles. Moreover, we can confirm that for increasing velocity, the particles displaced more from wall<sub>1</sub>. In addition, we can confirm that lateral particle displacement increases with higher viscoelastic polymer concentrations. For instance, for PEO 0,2 wt% (Fig. 43a) PSL7 and PSL10 cannot be separate in all velocity conditions, because the difference of dimension is around 3  $\mu\text{m}$  and therefore the viscoelastic force acting on the two different particle sizes is insufficient for a significant difference in lateral particle displacement. Indeed, the forces (see sec. 3.1) applied on PSL7 and PSL10 are of order of magnitude of  $10^{-10}\text{N}$  for PSL7 and PSL10 in PEO0,2 in all  $V_{\max,B}$  considered, while is of order of  $10^{-9}\text{N}$  using PEO 0,4 with a velocity  $> 15\text{mm/s}$ . While, when PEO concentration was increased the distance between different sizes of particles increase, due to increase of fluid relaxation time (see Table 2 and consequently the viscoelastic force increases).

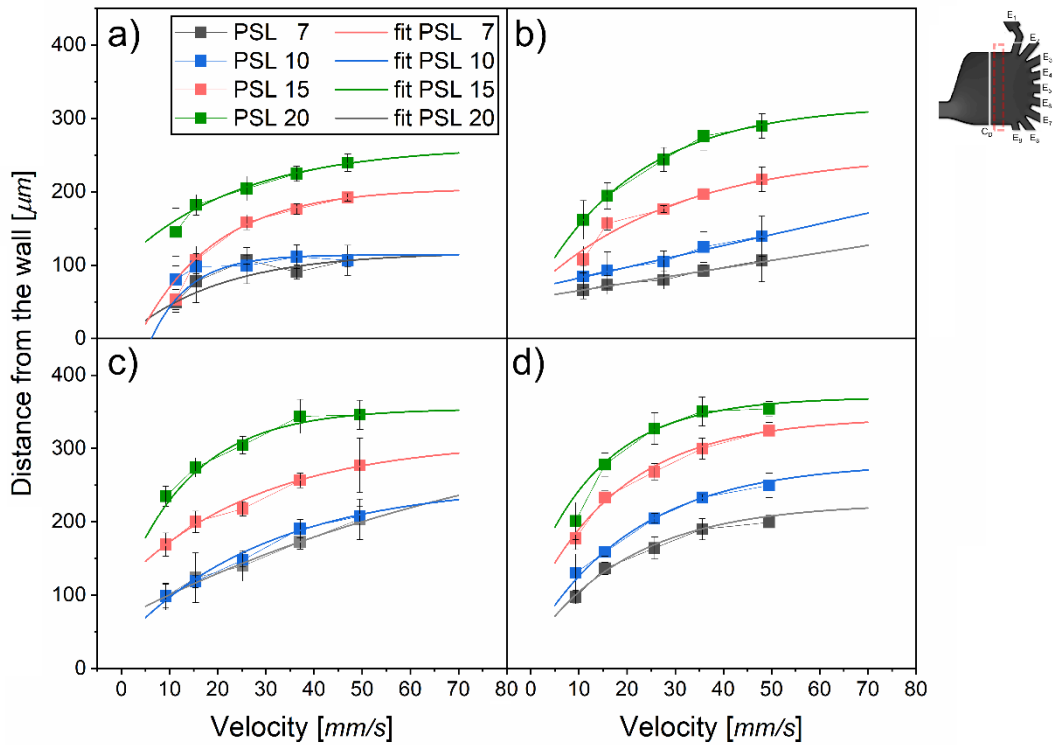


**Fig. 43** Average lateral displacement of PSL7 (grey), PSL10 (blue), PSL15 (pink) and PSL20 (green) with fitting curves for a) PEO 0,2, b) PEO 0,3 c) PEO 0,4 and d) PEO 0,5 in the range of  $v_{max,B}$  10-50 mm/s.

Then we used an asymptotic curve fit of the experimental data to achieve the lateral displacement of PSL in the range from 5 mm/s to 70 mm/s with 651 data points, so we have a description of particle lateral displacement for the whole suitable velocity range of the presented microfluidic device. To verify the distance between particles, fitting curves were compared subtracting point by point the curves. As showed in Fig. 44 in more detail. As expected, our outcomes indicate that higher differences of diameter as well as viscoelastic polymer concentrations result in higher distance from particles. In fact, for all PEO conditions the highest particle displacement difference can be noticed for PSL20 versus PSL7, which have a size difference of 13  $\mu\text{m}$ . It is important to highlight as group of particles with same difference in diameter (PSL20-PSL15 and PSL15-PSL10) present similar lateral displacement in PEO 0,3 and PEO 0,4 conditions, while this trend is not confirmed in PEO 0,2 and

PEO 0,5, where the difference between PSL15 versus PSL10 is higher than the difference between PSL 20 versus PSL15.

In both cases the particle difference is 5 $\mu\text{m}$ , but in the latter case the PSL 20 reached a plateau condition, which result in smaller displacement differences, while in the condition of PEO 0,2 the differences can be associated to insufficient displacement caused by the low viscoelastic forces.

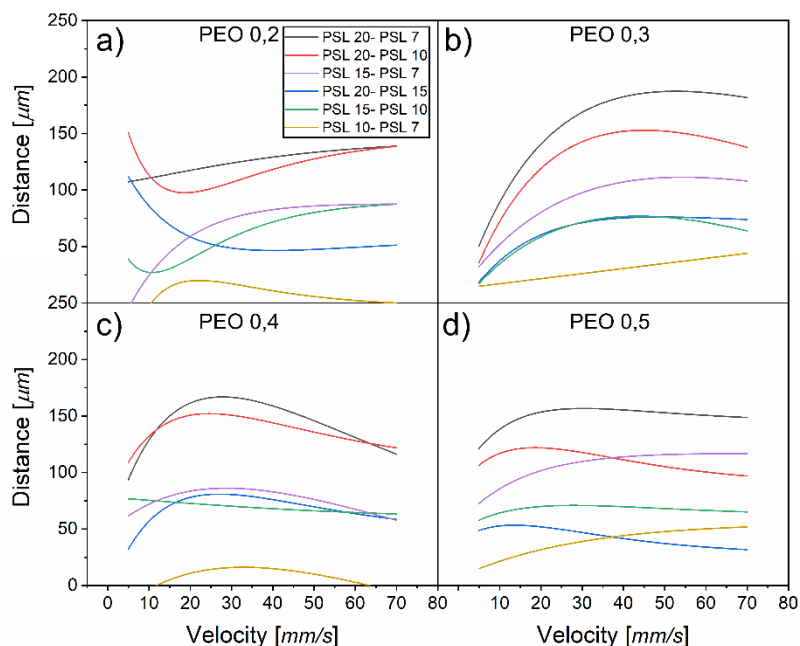


**Fig. 44** Difference of lateral displacement between particles (PSL7-PSL10 yellow curve, PSL15-PSL10 green curve, PSL20-PSL15 blue curve, PSL15-PSL7 purple curve, PSL20-PSL10 red curve, PSL7-PSL20 grey curve) in function of a) PEO 0,2, b) PEO 0,3 c) PEO 0,4 and d) PEO 0,5 in the range of  $v_{\max,B}$  10-50 mm/s.

The above-mentioned lateral particle displacements depend mainly on blockage ratio of particles in  $C_C$ , the length of channel C and viscoelastic forces (including PEO concentration and velocity) acting in channel C. In fact, the migration velocity in a PEO solution depends on the used polymer concentration, the size of particle and applied shear rate in the channel section position. Particles closer to wall<sub>1</sub> have a velocity of migration higher than particles that are closer to the centre of the channel with similar diameter depending on the different shear rate entities. In PEO 0,2 wt%

and PEO 0,5 wt% (Fig. 44) for  $V_{max,B} > 35 \text{ mm/s}$  PSL20 reach up before their plateau while PSL15 trend to reach up the PSL20, for PSL10 and PSL 15 this behaviour it is verify caused to low blockage ratio of PSL10.

Fig. 45 shows the lateral displacement between different particle sizes for varying PEO conditions. For PSL7 – PSL10 the highest differences are noticed for PEO 0,5, for PSL10 – PSL15 at higher velocity conditions the difference are constant, for

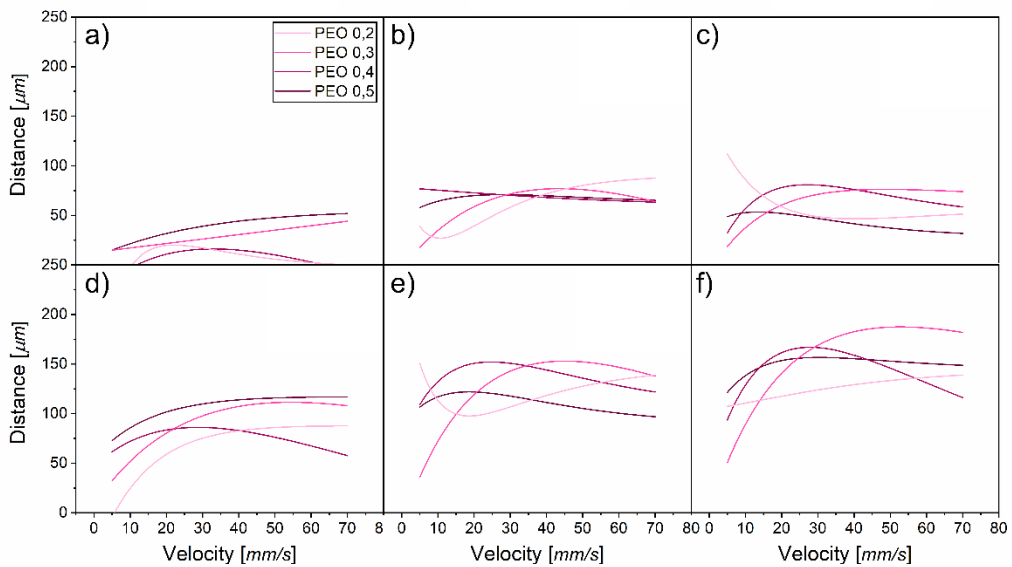


**Fig. 45** Difference of fitting curve of a) PSL7 with PSL10 b) PSL10 with PSL15 c) PSL15 with PSL20 d) PSL7 with PSL15 e) PSL10 with PSL20 and f) PSL7 with PSL20 changing PEO concentration (PEO 0,2 light pink, PEO 0,3 dark pink, PEO 0,4 light purple, and PEO 0,5 dark purple) in the range of  $V_{max,B}$  10-50  $\text{mm/s}$ .

PSL15- PSL20 at higher velocity and lower velocity the most significant lateral displacements are showed from PEO 0,4 and PEO 0,5 respectively, for PSL7 – PSL15 at higher velocity PEO 0,4 and PEO 0,5 are comparable, for PSL10 – PSL20 and PSL7 – PSL20 the higher distance is verified for PEO 0,4 and PEO 0,3 with low velocity and high velocity respectively.

To verify our particle observations for the microfluidic device calibration we tested our system for all PSL sizes in PEO 0,4. We obtained a purity of 99,1% in E2 with a efficiency of 93.10% and throughput of  $1,5 \times 10^4$  particles/h for PSL15 with  $V_{max,B}$  of 15  $\text{mm/s}$ .

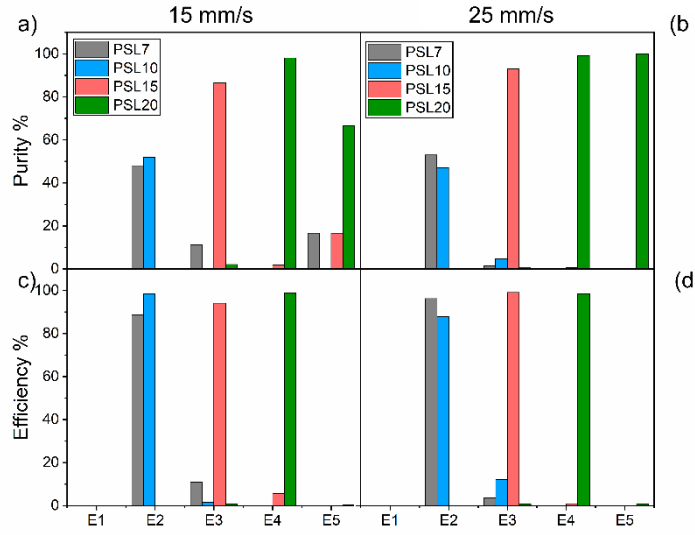


**Fig. 46** a),b) purity and efficiency of separation between PSL7, PSL10, PSL15 and PSL20 at the velocity of 15 mm/s. c),d) purity and efficiency of separation between PSL7, PSL10, PSL15 and PSL20 at the velocity of 25 mm/s. Both analyses are performed using PEO 0,4.

We confirm, that it is possible to separate particles of 7  $\mu\text{m}$  and 10  $\mu\text{m}$  from those of 15 and 20  $\mu\text{m}$  with a purity, efficiency and throughput of 97.62%, 100% and  $2 \times 10^5$  particles/h, respectively with a  $V_{max,B}$  of 25 mm/s (Fig. 46b,d). The separation of 20  $\mu\text{m}$  from the other particles was verified also at the velocity of  $V_{max,B}$  of 15 mm/s with a purity > 9% and with an efficiency of 98% (Fig. 46a,c). For the velocity of  $V_{max,b}$  is possible increase the throughput of separation at  $2 \times 10^5$  particles/h but the purity and efficiency decrease to 85% and 90%, respectively. In Fig. 47 the snapshot of separation between PSL7-PSL10-PSL15-PSL20 using PEO 0,4 at  $V_{max,B}$  25 mm/s was showed. In sec. S1 real image and video of particle flow into device are showed.

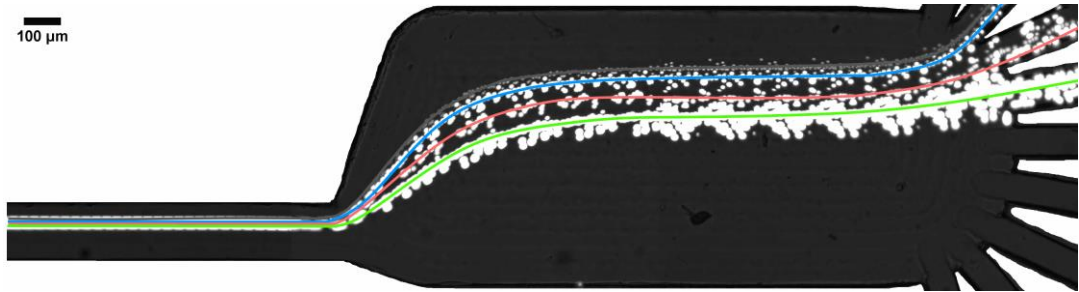


*Fig. 47 Snapshot of separation between PSL7-PSL10-PSL15 and PSL20 using PEO 0,4 at 25 mm/s in  $C_D$ .*

## **4.2 Glycerol Measurement**

To assure that the observed particle separation was not influenced mainly by inertial force, we measured the lateral displacement of particles in  $C_D$  using a Newtonian fluid, such as Gly 70 v/v% with similar viscosity properties of PEO 0.4 wt%, (0,016 Pa s and 0,0154 Pa s for Gly 70 v/v% and PEO 0,4, respectively). The small differences of fluid viscosity can be neglected for our further particle investigations. In Fig. 48a, the median lateral displacement positions of PSL7, PSL10, PSL15 and PSL 20 are shown for Gly 70 v/v%. In this experimental measurement case, the particles do not concentrate in a specific lateral position but are more spread over the full range of width in  $C_D$ , as clearly indicate from the large standard deviation presented in Fig. 48a.

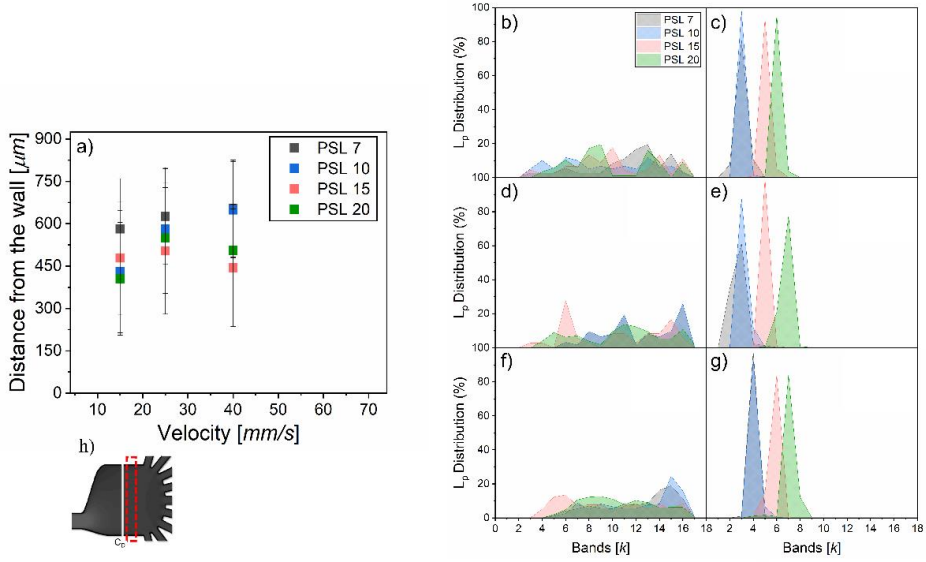


**Fig. 48** a) Average of lateral displacement in  $C_D$  of PSL7 (grey), PSL10 (blue), PSL15 (pink) and PSL 20 (green) using Gly 70% varying  $v_{\max,B}$  (15mm/s, 25 mm/s, 37mm/s). b) Normalized particle distribution in bands of PSL7 (light grey), PSL10 (light blue), PSL15 (light pink), PSL20 (light green) with a  $v_{\max,B}$  of 15 mm/s using Gly 70% in  $C_D$ . c) Normalized particle distribution in bands of PSL7 (light grey), PSL10 (light blue), PSL15 (light pink), PSL20 (light green) with a  $v_{\max,B}$  of 15 mm/s using PEO 0,4. d) Normalized particle distribution in bands of PSL7 (light grey), PSL10 (light blue), PSL15 (light pink), PSL20 (light green) with a  $v_{\max,B}$  of 25 mm/s using Gly 70% in  $C_D$ . e) Normalized particle distribution in bands of PSL7 (light grey), PSL10 (light blue), PSL15 (light pink), PSL20 (light green) with a  $v_{\max,B}$  of 25 mm/s using PEO 0,4 in  $C_D$ . f) Normalized particle distribution in bands of PSL7 (light grey), PSL10 (light blue), PSL15 (light pink), PSL20 (light green) with a  $v_{\max,B}$  of 37 mm/s using Gly 70% in  $C_D$ . g) Normalized particle distribution in bands of PSL7 (light grey), PSL10 (light blue), PSL15 (light pink), PSL20 (light green) with a  $v_{\max,B}$  of 37 mm/s using PEO 0,4 in  $C_D$ .

To compare the lateral distribution of particles in Gly 70 v/v% with the PEO 0,4 condition, the 900  $\mu\text{m}$  width channel  $C_D$  is divided into eighteen virtual segments (bands of 50  $\mu\text{m}$  width each). We normalized the particle number in each segment by the total number of particles traversing the entire section and present our outcome in Fig. 48b-g. The particle in Gly 70 v/v% are spread over the full range of width in  $C_D$  (Fig. 48b, d, f) while for PEO 0,4 the lateral displacement is clearly focused in a lower number of bands due to the viscoelastic effect of PEO solution (Fig. 48c, e, g). In sec. S2 are presents real image of particles into device.

### ***4.3 Particle investigation in channel C***

To verify particle separation, the lateral displacement of particles in  $C_C$  at 0, 5, 15, 25 mm from the bifurcation were analysed at different velocity using a PEO 0.4 wt% condition. The indicated PEO condition was used due to the highest lateral displacement differences measured in the previous section. For simplicity we show outcomes from the right part of the bifurcation. Notice that measurements of left part of the bifurcation show similar outcomes (data not presented). However, we used three different types of particles, PSL7, PSL15 and PSL20. As shown in Fig. 49 all particles at the bifurcation were next to the wall ( $wall_1$ ), and in  $C_C$  their distance from the inner wall increases downstream the channel. Furthermore, as expected the particle position is strongly influenced by the particle size. Indeed, the PSL20 moved more from the wall than smaller particles, such as PSL7, for example. For increasing velocity, the distance between different particles size increases. In particular, as showed in Fig. 48c, the distance between PSL15 and PSL20 was highest at velocity of  $V_{max,B}$  23mm/s than lower velocity 12 and 16 mm/s (PSL20-PSL15 distance 3,34  $\mu\text{m}$ , 5,3  $\mu\text{m}$  at the velocity of 12 and 16 mm/s and 18,3  $\mu\text{m}$  at the velocity of 23mm/s). At 12 mm/s the distance between PSL7 and PSL20 is similar to that at 23 mm/s (40  $\mu\text{m}$ ), this happen because at the higher velocity also PSL7 begins to migrate towards the centre of  $C_C$ .

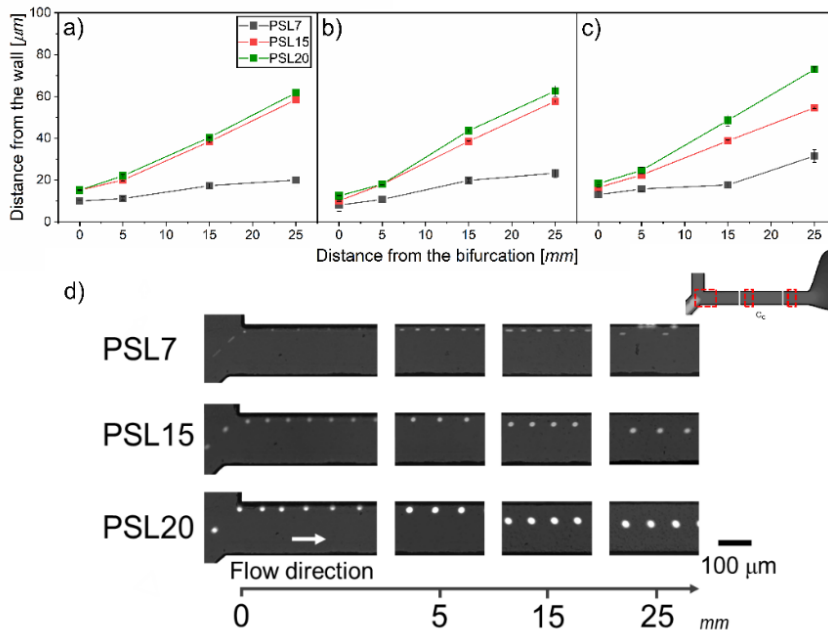


**Fig. 49** a),b),c) Lateral displacement of PSL7, PSL15 and PSL20 at the velocities of 12 mm/s, 16 mm/s and 23 mm/s, respectively using PEO 0.4. d) Snapshot of lateral displacement of PSL7, PSL15, PSL20 in  $C_c$ .

The particle separation on size verified in the previous paragraph (see sec.4.1 ) was an important result, showing the correct working of our device for different flow conditions. Indeed, the contemporary separation of four type of particles was realized in function of their dimension. At this point we want to test our device for separation of particles with different mechanical properties. For this reason, following paragraphs are concentrated on realization and characterization of microgel with different concentration of  $C_T$  (5,9% , 7,9%, 11,8%, 15% and 20%).

#### 4.4 Hydrogel Characterization

In order to optimize the experimental set-up for the hydrogel production regarding  $C_T$  (total monomer concentration) and ATTO concentrations, we evaluated the effect of lamp power and photoinitiator concentration on the final mesh size  $\xi$  (defined as the linear distance between two adjacent crosslinks [137] and is a key structural

parameter for hydrogel) of hydrogel. First, bulk hydrogel of different concentration of AAm and BIS were realized. We used a constant ratio between AAm and BIS of  $C=3.5\%$ , varied  $C_T$  from  $5.9\%$  to  $20\%$  (as showed in the Materials and Methods section 3.10). In more detail, we prepared bulk solution of  $100\ \mu\text{l}$  on a slide and weighted the slide after polymerization for drying and swelling conditions.

To verify the influence of DAROCUR concentration (photoinitiator) on the hydrogel preparation, we prepared for  $C_T=11.8\%$  two bulk samples with different concentration of photoinitiator  $0.5\%$  and  $1\%$  and compared the different swelling outcomes. As showed in Table 8, percentage of water is constant for both solutions, so we confirmed that for the mention DAROCUR concentration no significant influence on our sample properties occur.

**Table 8** Weight of hydrogel bulk ( $100\ \mu\text{l}$ ) with  $C_T=11.8\%$ , post-curing, swelled and dry and percentage water using two different DAROCUR concentrations ( $1\%$  and  $0.5\%$ ).

% DAROCUR	Weight [mg]			
	Post-curing	wet	dry	% water
1%	11.58	125.94	8.84	92.78%
0.50%	46.29	109.32	8.41	92.31%

Afterwards we produced hydrogel particles for the same two types of  $0.5\%$  and  $1\%$  DAROCUR concentration using a  $C_T=11.8\%$ . Also, in this case the percentage of swelling (%swelling) between both solutions is comparable (see Table 9).

**Table 9** Comparison of swelled diameter, in flow diameter (diameter measured during particle generation in microfluidic device),  $V_{eq}$  and percentage swelling of AAm particles  $11.8\%$  using two different DAROCUR concentrations ( $1\%$  and  $0.5\%$ ).

% DAROCUR	Swelled diameter	Dev std	CV	In flow diamater	Dev std	CV	$V_{eq}$	%swelling
1.0%	28.93	2.10	7.94%	19.10	0.93	4.87%	3.47	51.5%
0.5%	26.53	0.79	2.99%	17.60	0.59	3.03%	3.40	50.4%

The microfluidic polymerization is different from the bulk polymerization because the particles flow through the outlet channel with a specific velocity (which depends

on the applied velocity) and in such a condition only a small part of channel is irradiated, to investigate the complete polymerization of hydrogel particles in- flow we used two different lamp power settings (% lamp power 50% and 100%) and compared the %swelling. As showed in Table 10 the percentage of swelling using 100% lamp power is lower that 50%, this indicate that using the 50% lamp power the particles do not complete their polymerization.

**Table 10** Comparison of swelled diameter, in flow diameter,  $V_{eq}$  and percentage swelling of PA particles 11,8% using two different percentage lamp power, 100% and 50%.

% Lamp Power	Swelled diameter	Dev std	CV	in flow diameter	Dev std	CV	$V_{eq}$	%swelling
100%	25.95	1.93	7.5%	19.04	0.93	4.9%	2.53	36.3%
50%	26.99	2.27	8.4%	19.04	0.93	4.9%	2.85	41.7%

For these reasons, the parameters for the hydrogel production were set to 100% lamp power with DAROCUR 1%.

#### 4.5 Swelling characterization

Several hydrogel samples were prepared for swelling properties characterization using polymer concentrations of  $C_T$  5,9, 7,8, 11,8 15 and 20, in order to characterize different network structures. In particular, swelling parameters ( $v_{2,s}$ ,  $M_c$ ,  $\xi$ ) were calculated as shown in Table 11.

**Table 11** Comparison of  $v_{2,s}$ ,  $M_c$  and  $\xi$  of PA particles with different concentration of  $C_T$  (5,95%, 7,9%, 11,8%, 15% and 20%) using % lamp power 100%.

$C_T$	$v_2$	$M_c$	$\xi$ [nm]
5.95	1.09E-03	1.53E+05	12.15
7.90	1.85E-03	8.89E+04	9.39
11.80	4.32E-03	3.66E+04	6.27
15.00	6.41E-03	2.39E+04	5.23
20.00	9.94E-03	1.46E+04	4.31

As expected,  $F_{\text{water}}$  of calculate for bulk is compared to  $F_{\text{water}}$  calculate for particles at the same  $C_T$  concentration (Table 12 and Table 8) . In particular, changing the  $C_T$  concentration from 5,9% to 20%, polymer volume fraction in the range of 0.001-0.009 was obtained. The equilibrium-swelling ratio decreased from 90 to 36% with increasing  $C_T$  (see Table 12). With these recipes, mesh size in the range of 4,31-12,15 nm was achieved from  $C_T$  5,9% to 11,8% (see Fig. 50).

**Table 12** Comparison of  $V_{eq}$ , %swelling and %water of PA particles with different concentration of  $C_T$  (5,95%, 7,9%, 11,8%, 15% and 20%) using % lamp power 100%.

$C_T$	Swelled diameter	Dev std	CV	in flow diameter	dev std	CV	$V_{eq}$	%swelling	%water
5.95	33.32	6.14	18.43%	17.51	1.30	7.41%	6.89	90.2%	98.2%
7.90	31.29	1.31	4.19%	17.80	0.43	2.17%	5.43	75.8%	95.0%
11.80	28.93	2.10	7.94%	19.10	0.93	4.87%	3.47	51.5%	92.2%
15.00	27.78	1.78	6.33%	19.31	0.32	1.66%	2.98	43.9%	90.1%
20.00	27.53	1.52	5.53%	20.13	0.40	1.97%	2.56	36.8%	84.4%

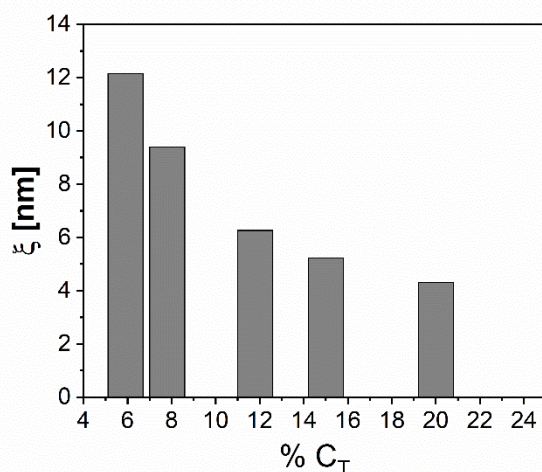


**Fig. 50** Mesh size of PA particles varying of  $C_T$ .

Next to decide the ATTO concentration we will use for our hydrogel production, we analysed the fluorescence intensity of microgel  $C_T=11,8\%$  (diameter of 15  $\mu\text{m}$ ) with

two different ATTO concentration, 0,05 mM and 0,1 mM. As showed in Fig. 51 microgel with 0,1 mM of ATTO have a significant higher fluorescence intensity signal compared to the one with 0.05 mM,  $5578 \pm 1316$  and  $2613 \pm 868$ , respectively.

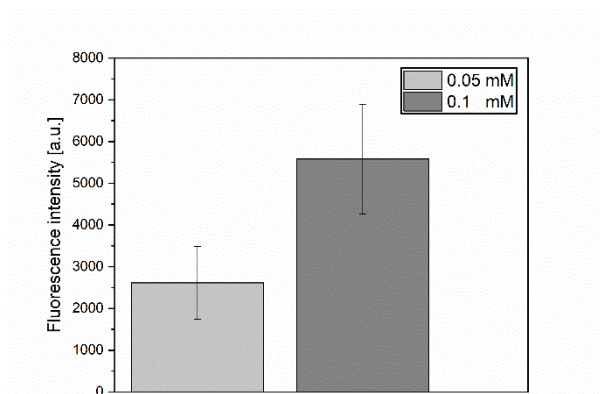


**Fig. 51** Fluorescence intensity of PA particles ( $C_T=11,8\%$ , 100% lamp power) using two different concentrations of ATTO 0,05 mM (light gray) and 0,1 mM (dark gray).

For these reasons, for subsequent analysis, functionalized hydrogel particles were synthesized using  $C_T$  11.8, 15%, 20% with 0,1 mM ATTO polymerizate with a %lamp power of 100%. In fact, results demonstrated that hydrogel with  $C_T$  lower than 11.8% were not realizable, probably this is due to presence of ATTO that do not consent the stable realization of particles, maybe they are too soft and not enough resistant to resist the washing procedure for batch purification.

#### **4.6 Rheological properties of hydrogel**

Different concentrations of  $C_T$  result in different mechanical properties to hydrogel particles. To test the young modulus of the used hydrogel setting, bulk samples with three different concentration of  $C_T$  11,8%, 15% and 20% with a 0.1mM of ATTO were prepared.

First a frequency test with a parallel plate geometry at room temperature was realized with a standard stress-controlled rheometer to obtain the searched for complex shear

modulus ( $G$ ). As showed in Fig. 52a, when the concentration of  $C_T$  increases the shear modulus increase. Out of this data we have calculated the Young modulus,  $E$ , from experimental measured shear modulus with follow relation:

$$E = 2G(1 - \nu) \quad \text{Eq. 4.6-1}$$

where  $\nu=0.5$  is the Poisson coefficient. As shown in Fig. 52b for  $C_T$  11,8% with a 0.1mM ATTO,  $E$  is 17 kPa for  $C_T$  15% with a 0.1mM ATTO  $E$  is 50 kPa while for  $C_T$  20% with a 0.1mM ATTO  $E$  is 110 kPa.

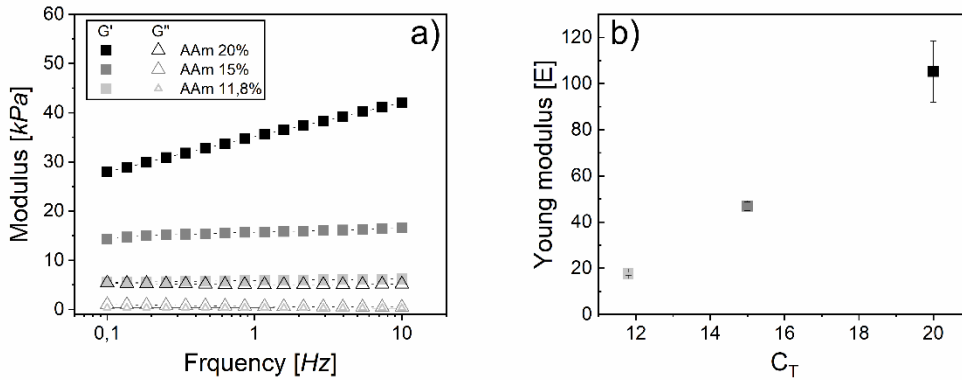


**Fig. 52** a) Storage ( $G'$ ) and loss ( $G''$ ) modulus of the complex shear modulus ( $G$ ) in function of frequency for PA bulk and b) Young modulus of PA with a  $C_T$  11,8% (light grey), 15% (dark grey) and 20% (black).

## 4.7 Hydrogel investigation channel C and D

To study the application of our microfluidic device for particles with different deformability we decided to test two different types of microgel  $C_T=15\%$  (AAm 15%) versus  $C_T=11,8\%$  (AAm11,8%) with similar size of  $15 \mu\text{m}$  of diameter at different measurement conditions. In more detail, we tested particles with PEO 0,2 and PEO 0,4 at different velocity from 10 to 50 mm/s.

First, we investigated the lateral displacement in  $C_D$  from wall<sub>1</sub> between Aam 15% and PSL 15. In this case a young modulus of 50 kPa for the Aam 15% is compared to a polystyrene particle with a Young modulus in the order of GPa at PEO 0,2 with a  $V_{max,B}$  from 10 to 50 mm/s. The different lateral displacement between particles do

not consent their separation in all velocity considered. In Fig. 53a, b the particle separation between microgel AAm 11,8% and PSL15 was showed for PEO 0,2. At the  $V_{max,B}$  of 35 mm/s the AAm 11,8% show a lateral displacement of 212.6  $\mu\text{m}$ , while AAm 15% indicate a lateral displacement of 180.9  $\mu\text{m}$ , the difference between them is of about 30  $\mu\text{m}$ . This is an important result, indeed AAm 11,8% ( $E=17,6\text{kPa}$ ) displace more from wall more than AAm 15% ( $E=46,9\text{kPa}$ ) particles.

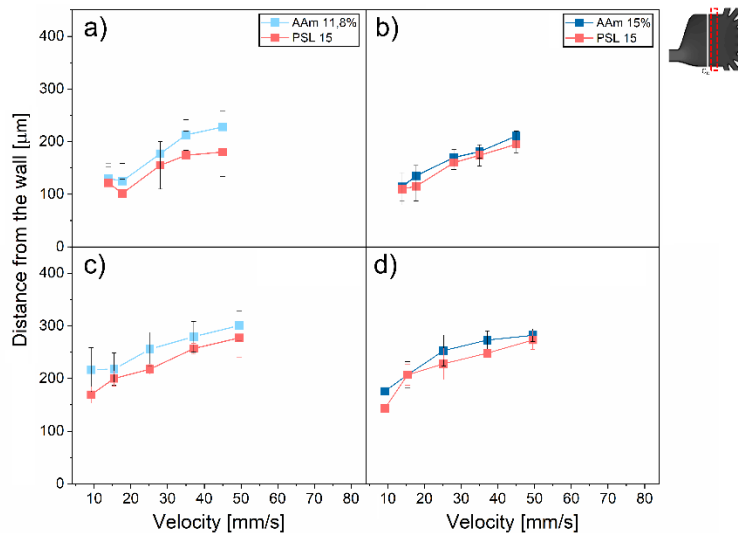


**Fig. 53** AAm 11,8% (light blue) and AAm 15% (dark blue) average lateral displacement compared to PSL15 average lateral displacement in  $C_D$  for a),b) PEO 0,2 and c),d) PEO 0,4 varying  $v_{max,B}$  from 10 mm/s to 50 mm/s.

Then we have compared lateral displacement of particles for PEO 0,4 (see Fig. 53c,d). In this case, AAm 15% and AAm 11,8% present similar lateral displacement for  $V_{max,B} < 49,5\text{mm/s}$  and the maximum distance of 28  $\mu\text{m}$  at the velocity of  $V_{max,B} = 49,6\text{ mm/s}$ .

For a deeper look inside of the presented phenomena, the lateral displacement in  $C_C$  was verified for three distinct fluid velocities 15, 25 and 33 mm/s using PEO 0,2 and PEO 0,4 (at  $V_{max,B} > 33\text{ mm/s}$  in  $C_C$  a blurring effect occur and therefore was excluded from our analysis) at three different distances from the bifurcation (right side) 0, 12,5 and 25 mm (see Fig. 54).

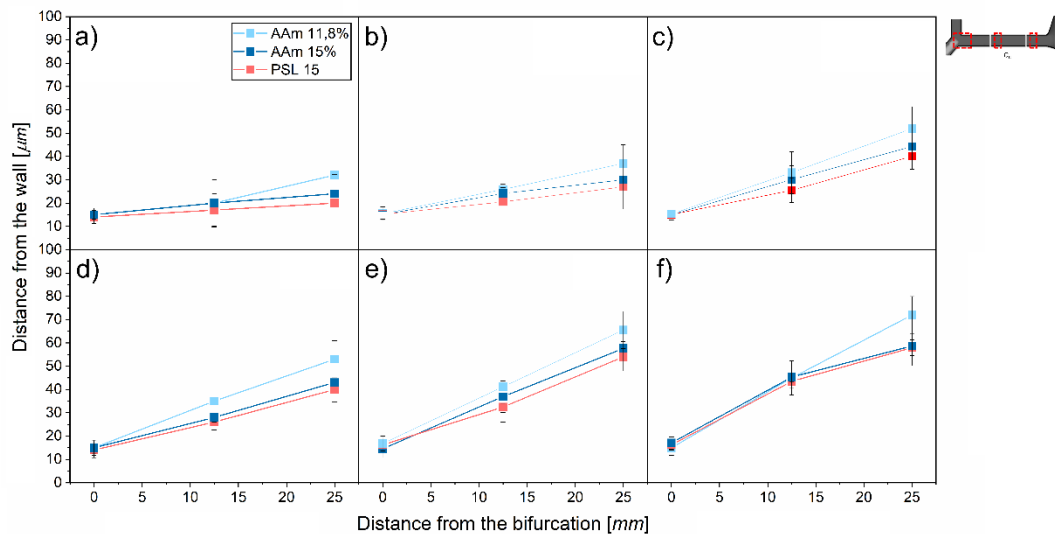


**Fig. 54** AAm 11,8% (light blue) and AAm 15% (dark blue) average lateral displacement compared to PSL15 average lateral displacement in  $C_C$  for a), b), c) PEO 0,2 at the  $v_{max,B}$  of 15, 25 and 35 mm/s, respectively, and for d), e), f) PEO 0,4 varying  $v_{max,B}$  from 10 mm/s to 50 mm/s.

In Fig. 54a,b,c the  $V_{max,B}$  15, 25, 33 mm/s respectively are presented for PEO 0,2. At the bifurcation (distance = 0mm) all particles are in close to wall<sub>1</sub>, afterwards they move towards the center of  $C_C$ . At the velocity of  $V_{max,B}=33\text{mm/s}$  the AAm 11,8% show the highest lateral displacement between the presented velocities compared to the lateral displacement of AAm 15% and PSL 15.

In Fig. 54d,e,f, the distance between AAm 11,8% and PEO 0,4 at  $V_{max,B}$  of 15, 25, 33 mm/s was analysed. Also in this case, the increase of velocity gives a higher lateral displacement of particles and AAm 11,8% compared to AAm 15% and PSL15. This confirm that there is an important influence of deformability on lateral displacement in the channel C of our microfluidic device.

## 4.8 Cell separation

In general, each type of cell line presents different diameters and mechanical cell properties. In particular, we have used MDA-MB-231, MCF-7 and MCF-10a cell

lines for our studies. In Table 13 we show the experimental obtained size according to static cell investigations indicated in material and methods section 3.8, while in Fig. 55 we present mechanical properties of the investigated cell lines from literature research [138], [139]. .

**Table 13** MCF10a, MDA, MCF7 diameters measured with an optical microscope with a magnification 100x.

	<i>Dim</i>	<i>Dev std</i>
<b>MCF10a</b>	18.12	1.90
<b>MDA</b>	17.97	2.90
<b>MCF7</b>	17.75	1.73

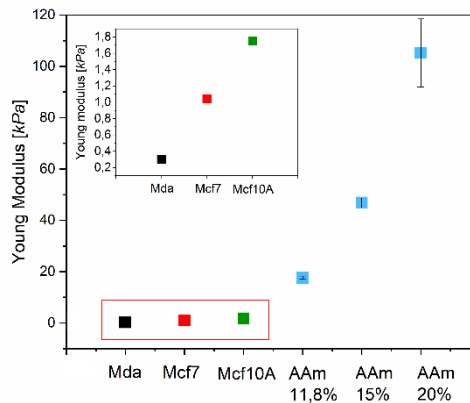


**Fig. 55** Young modulus of AAm 11,8%, AAm 15%, AAm20% (light blue), MDA (black) [108], MCF10a (green) [108] and MCF7 (red) [109].

The MDA-MB-231 cell line is a highly aggressive and invasive epithelial, human breast cancer cell line, and its Young modulus is of  $E=0,3$  kPa, which is significant lower compare to the other investigated cell line [138]. MCF-7 is a non-invasive breast cancer cell line ( $E=1,04$ kPa) [139], which shows an intermediate Young modulus compare to the third investigated cell line the MCF-10a, which is a non-tumorigenic human mammary epithelial cell line ( $E=1,75$ kPa) [138]. It is well known in literature that tumoral cells have a lower Young modulus compared to their healthy counterparts [140], which can allow a microfluidic based cell type separation

regarding their deformability properties. We tested the mentioned cell lines with two different PEO concentrations (PEO 0,2 and PEO 0,4) for varying fluid velocity  $V_{max,B}$  in a range of 10 mm/s-50 mm/s in  $C_D$ .

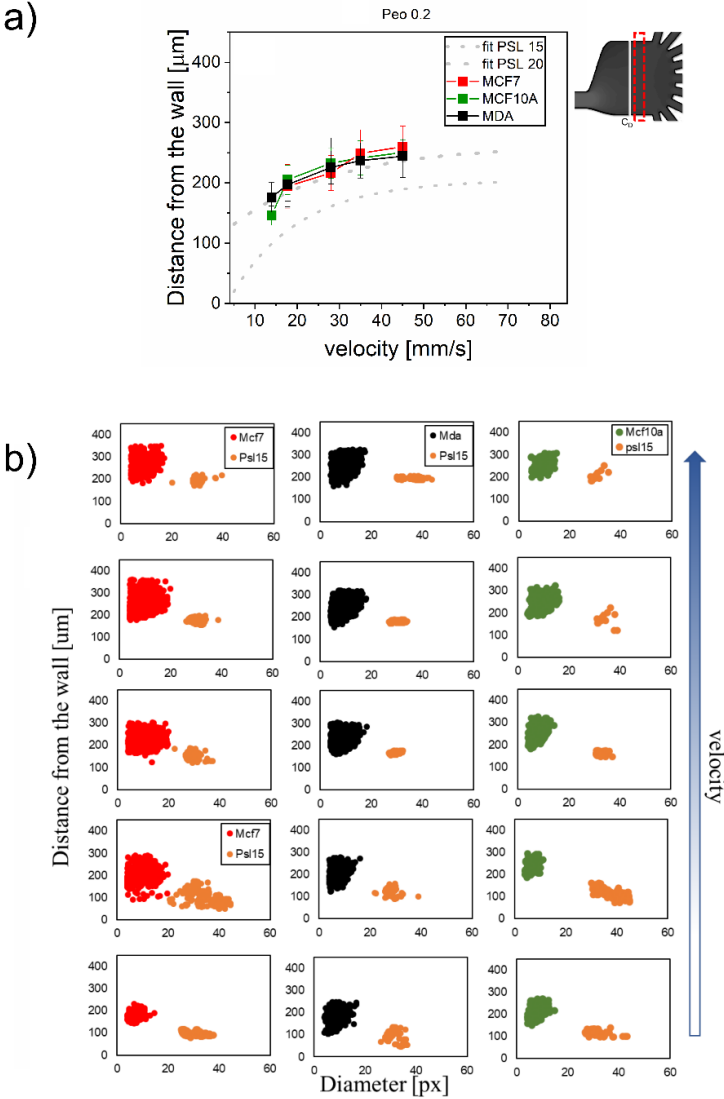


**Fig. 56** a) Average lateral displacement of MCF7 (red), MCF10a (green) and MDA (black) and fitting curves of PSL15 (thin dot line) and PSL20 (fat dot line) using PEO 0,2 with  $v_{max,B}$  from 10 mm/s to 50mm/s. b) scatterplot of lateral displacement of MDA, MCF7 and MCF10a in function of dimension in pixel varying velocity using PEO 0,2 with  $v_{max,B}$  from 10 mm/s to 50mm/s.

For PEO 0,2 condition (see Fig. 56a), all three cell lines presents a lateral displacement higher than PSL15 for all investigated  $V_{max,B}$  conditions, but it is not possible distinguish different cell lines in function of lateral displacement. In this case indeed, the viscoelastic force does not consent to distinguish the cell lines with similar size. In PEO 0,4 instead, the lateral displacement of cell lines is significantly different. MDA-MB-231 cells show a higher lateral displacement compared to MCF-7 and MCF-10a cells for all range of considered velocities. In particular, at  $V_{max,B} = 10\text{mm/s}$  the distance between MDA-MB-231 and MCF-7 is of around  $80\ \mu\text{m}$ , while that one between MDA-MB-231 and MCF-10a is of about  $47\ \mu\text{m}$ . At  $V_{max,B}$  of  $25\ \text{mm/s}$ ,  $70\ \mu\text{m}$  and  $35\ \mu\text{m}$  are the distance between MDA-MB-231 versus MCF-7 and MDA-MB-231 versus MCF-10a respectively. For increasing velocity, the distance between cell lines decreases, this is due to the increase of viscoelastic effect that consent to all cells to approach next to the center of  $C_C$ .

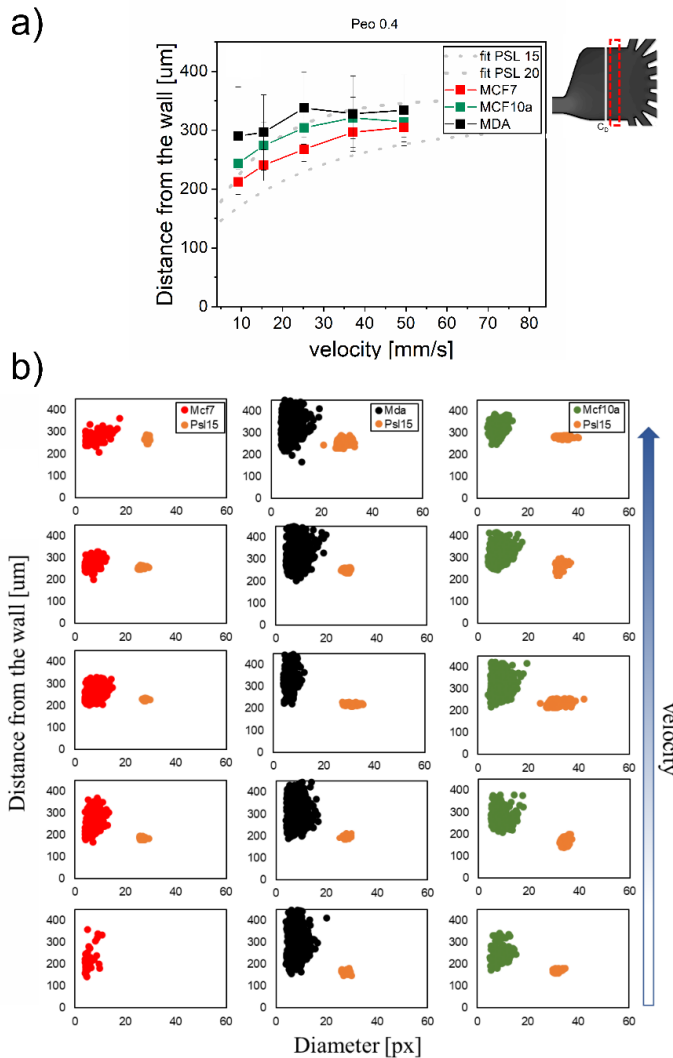


**Fig. 57** a) Average lateral displacement of MCF7 (red), MCF10a (green) and MDA (black) and fitting curves of PSL15 (thin dot line) and PSL20 (fat dot line) using PEO 0,4 with  $v_{max,B}$  from 10 mm/s to 50mm/s. b) scatterplot of lateral displacement of MDA, MCF7 and MCF10a in function of dimension in pixel varying velocity, using PEO 0,4 with  $v_{max,B}$  from 10 mm/s to 50mm/s.

To confirm these results, we have analysed the lateral displacement in  $C_c$  (0, 12,5, 25 mm from the right bifurcation) at the velocity of  $V_{max,B}=25\text{mm/s}$  for PEO 0,2 and PEO 0,4. Our data confirmed the results presented in Fig. 56 and

Fig. 57, where the PEO 0,2 distance are similar, while in PEO 0,4 MDA-MB-231 show higher lateral displacement than MCF-7 and MCF-10a.

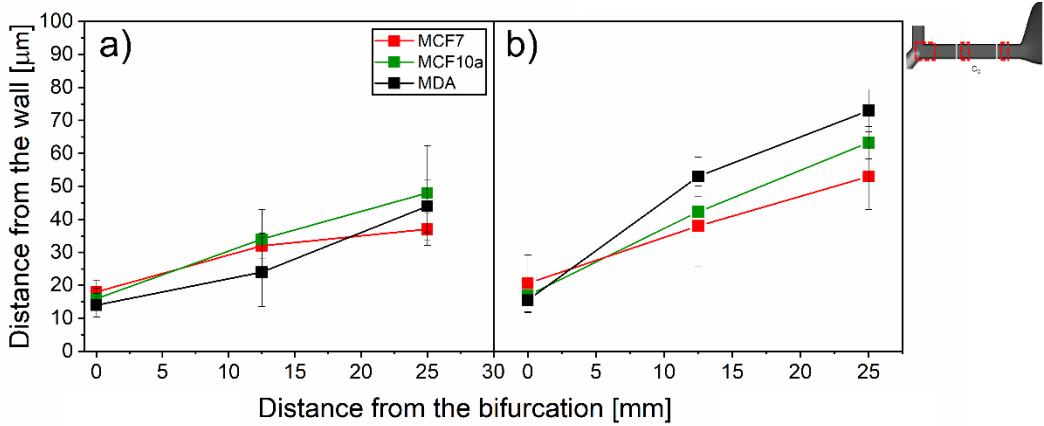


Fig. 58 Average lateral displacement of MCF7, MCF10a, MDA in  $C_c$  at the  $v_{max,B}$  of 25 mm/s using a) PEO 0,2 and b) PEO 0,4.

To verify our separation outcome, MCF10a, MCF7 and MDA cell measurement were performed using PEO 0,4 at the  $V_{max,B}=25\text{mm/s}$ . The purity and efficiency obtained are of 86,72% and 70,25% respectively with throughput of  $2 \times 10^4$  cell/h.

#### 4.9 AR analysis of cell lines

To better understand the physical phenomena for the previously observed cell line separation in  $C_C$  we performed high speed camera measurements in  $C_B$ , in different measurement points in  $C_C$  (0, 12,5 and 25mm from the right bifurcation) and in  $C_D$  for a  $V_{max,B}$  of 25 mm/s at PEO 0,2 and PEO 0,4.

In Table 14 the AR of such biophysical cell investigations in PEO 0,2 are shown, where MCF7 presents similar AR in all section of our microfluidic device. So, we can conclude that the applied fluid flow condition does not significantly deform

MCF7 cells. MCF10a showed a light deformation in  $C_B$  ( $AR=0.89\pm0.05$ ) and at 0 mm of  $C_C$  ( $AR=0.88\pm0.08$ ), which are not statistically significant.

Instead, MDA presented a light deformation in  $C_C$  at 0 ( $AR=0.88\pm0.08$ ) that is statistically significant ( $p\text{-value}<0.05$ ) compared to AR outcomes in  $C_D$  ( $AR=0.92\pm0.05$ ). This light deformation is recovered long  $C_C$  showing no statistically relevant differences at 12,5 mm, 25 mm compared to  $C_D$ . In Fig. 59 snapshot of cell inflow in PEO 0,2 are showed a 0mm (Fig. 59a), 2mm (Fig. 59b), 12,5 mm (Fig. 59c) and 25mm of  $C_C$  (Fig. 59d).

**Table 14** Aspect ratio of MCF7, MDA and MCF10a in  $C_B$ , at 0 mm, 12,5 mm and 25mm of  $C_C$  and  $C_D$  using PEO 0,2 at the velocity of 25 mm/s.

	$C_B$		$C_C$						$C_D$	
	AR	Dev std	0 [mm]		12,5 [mm]		25 [mm]		AR	Dev std
			AR	Dev std	AR	Dev std	AR	Dev std		
MCF7	0.93	0.05	0.92	0.05	0.94	0.04	0.92	0.06	0.92	0.05
MDA	0.86	0.08	0.86	0.10	0.88	0.08	0.88	0.07	0.92	0.05
MCF10a	0.89	0.05	0.88	0.08	0.96	0.02	0.93	0.03	0.95	0.04

In Table 15 Aspect ratio of MCF7, MDA and MCF10a in  $C_B$ , at 0 mm, 12,5 mm and 25mm of  $C_C$  and  $C_D$  using PEO 0,4 at the velocity of 25 mm/s., the data of AR outcomes for PEO 0,4 are shown for a velocity of  $V_{max,B}=25\text{mm/s}$  for MDA, MCF7 and MCF10a. For this measurement condition MCF7 and MCF10a do not present statistically significant difference for AR outcomes in all section considering ( $C_B$ ,  $C_C$  and  $C_D$ ). Instead, MDA presented a statistically relevant difference between AR measured in  $C_B$  ( $AR=0.94\pm0.03$ ) and the one measured in  $C_C$  at 0 mm ( $AR=0.85\pm0.075$ ). Differently to PEO 0.2 MDA, the light deformation is not recovered in  $C_C$  at 12,5 mm but in  $C_C$  at 25 mm.

**Table 15** Aspect ratio of MCF7, MDA and MCF10a in  $C_B$ , at 0 mm, 12,5 mm and 25mm of  $C_C$  and  $C_D$  using PEO 0,4 at the velocity of 25 mm/s.

	$C_B$		$C_C$						$C_D$	
	C <sub>B</sub>	Dev std	0 [mm]		12,5 [mm]		25 [mm]		C <sub>D</sub>	Dev std
			Dev std		Dev std		Dev std			
MCF7	0.921	0.037	0.899	0.060	0.912	0.039	0.924	0.039	0.911	0.067
MDA	0.940	0.031	0.853	0.075	0.843	0.064	0.908	0.029	0.925	0.056
MCF10a	0.930	0.050	0.868	0.082	0.914	0.051	0.925	0.021	0.951	0.014

In function of this results, in PEO 0.2 viscoelastic force were not sufficient to deform MF7 and MCF10a using a  $V_{max,B}=25\text{mm/s}$ , while for MDA only the maximum force presents near the wall were sufficient to give a light deformation that diminish downstream in  $C_C$  when cell migrates toward centre of the channel. For this reason, for PEO 0,2 we did not determine different lateral displacement between cell lines in  $C_D$  and in  $C_C$  (see Fig. 58a). In Fig. 60 snapshot of cell inflow in PEO 0,4 are showed a 0mm (Fig. 60a), 2mm (Fig. 60b), 12,5 mm (Fig. 60c) and 25mm of  $C_C$  (Fig. 60d).

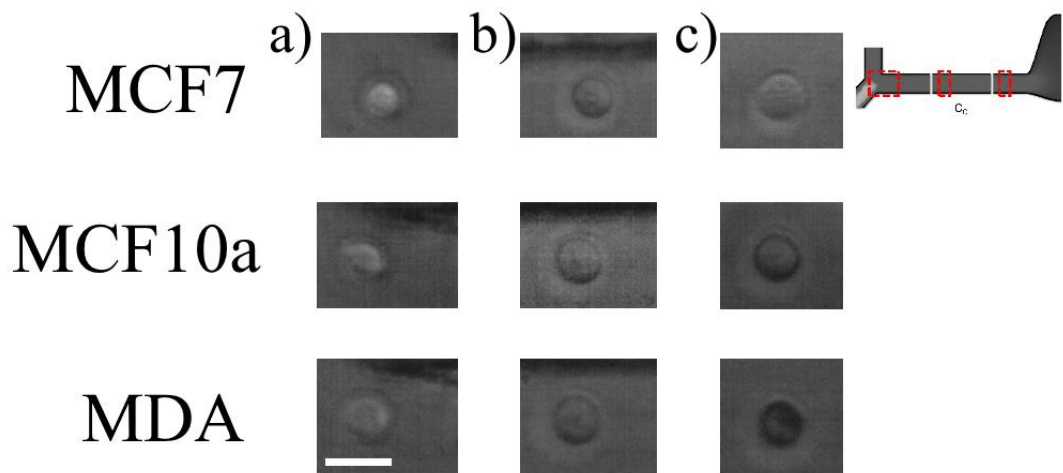


**Fig. 59** Snapshot of MDA, MCF7, MCF10a in PEO 0,2 using highspeed camera in a) 0mm, b) 12,5 mm and c) 25mm of  $C_C$ . Scale bar is 20  $\mu\text{m}$  width.

In PEO 0,4, the viscoelastic force is higher than that one of PEO 0,2, but it is sufficient to generate a light deformation only in MDA cell line in  $C_C$  at 0 mm and

12,5 mm. Indeed, as showed in Fig. 58b, MDA presents a lateral displacement higher than MCF7 and MCF10a in  $C_C$  and  $C_D$ .

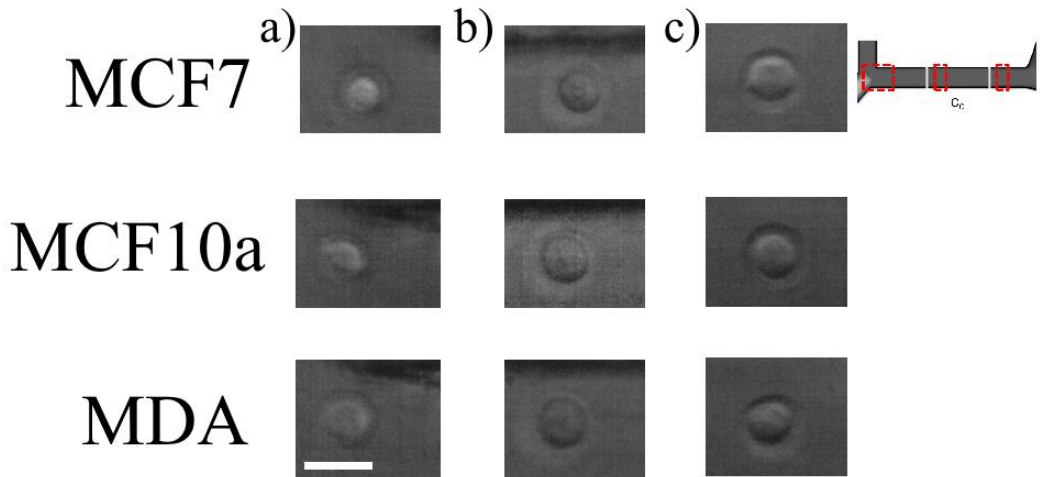


**Fig. 60** Snapshot of MDA, MCF7, MCF10a in PEO 0,4 using highspeed camera in a) 0mm, b) 2mm, c) 12,5 mm and d) 25mm of  $C_C$ . Scale bar is 20  $\mu\text{m}$  width.

#### ***4.10 Peripheral blood cell investigations***

To test our microfluidic device for real world application scenarios we investigated the separation performance between blood cells, such as RBC, neutrophils (Neutr), monocytes (Monoc) and lymphocytes (Lymph). First each different blood cell type was extracted from whole blood following the procedure described in the material and methods section 3.5 and subsequently mixed with known cell concentration for the following experimental measurements.

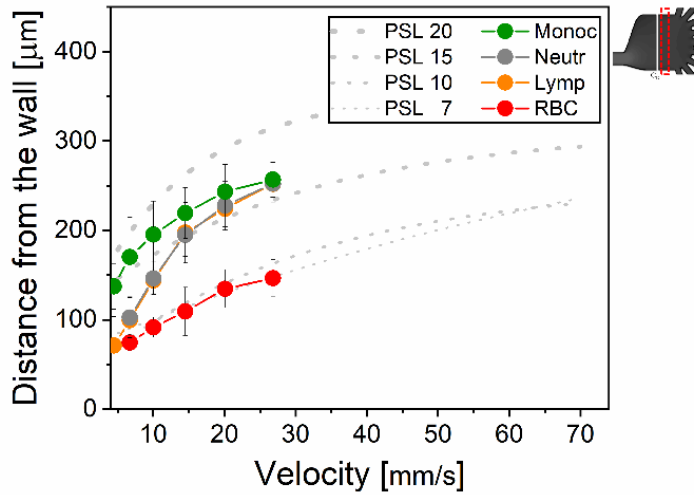


**Fig. 61** Average lateral displacement of RBC (red), Lymp (orange), Neutr (grey) and Monoc (green) in  $C_D$  using PEO 0,4 at  $v_{max,B}$  from 4 mm/s to 30 mm/s.

In Fig. 61, average values of lateral displacement of cell lines using PEO 0,4 in a range of  $V_{max,B}$  4–30 mm/s are shown. Also in this case, cell with bigger dimensions displace stronger from wall<sub>1</sub> than smaller ones. For instance, RBC (that have a dimension of circa 8  $\mu\text{m}$ ) moves from wall<sub>1</sub> similar as PSL 7 and therefore they can be simply separated from other blood cell types. When velocity increase the lateral displacement of Neutr and Lymp increase more than one of PSL10. In particular way, the difference between lateral displacement of Neutr or Lymp ( $a= 11,3\pm 0,45 \mu\text{m}$   $8,2 \pm 0,5$ , respectively) with PSL10 ( $a= 11,3\pm 0,45$ ) is of about 70  $\mu\text{m}$ . Probably, this different lateral displacement between PSL 10 and Neutr and Lymp is due to an effect of wall repulsion. In a particular way, we have performed the separation between RBC and Neutr for  $V_{max,B}$  equal to 20 mm/s resulting in a purity and efficiency with 99% and 89%, respectively for RBC (Fig. 62a,c). The lower purity of E3 is due to higher concentration of RBC than Neutr. Next, we performed the separation between Lymp and Mon for  $V_{max,B}$  of 15mm/s in this case the purity and efficiency are 95% and 93%, respectively for Lymp (Fig. 62b,d). In supporting, S3 image and video of two separations are showed.

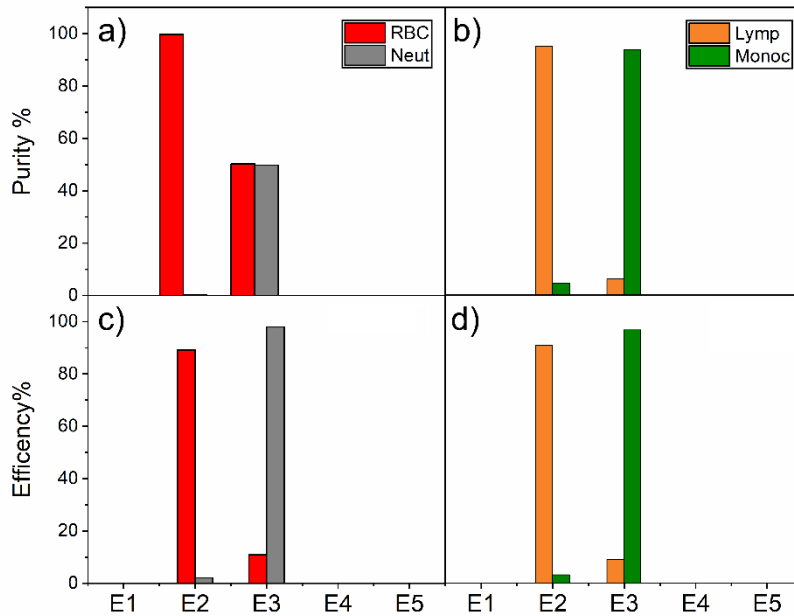


**Fig. 62** Purity and efficiency of separation between a,c) RBC and Neutr ( $V_{max,B}=20mm/s$ ) and b,d) Lymph and Monoc ( $V_{max,B}=15mm/s$ ), respectively using PEO 0,4.

To verify the deformability effect on blood cell, the lateral displacements of Lymph, Monoc and Neutr live were compared with that one with Lymph, Monoc and Neutr treated with Paf 4%. (that have a young modulus higher than live cells [141]) using PEO 0,4 in a range of  $V_{max,B}$  of 4-30 mm/s. RBC analysis were not performed due to using Paf 4% their form was lost. As showed in

Fig. 63, there are not differences in lateral displacement. The forces present in  $C_C$  are not sufficient to deform cells.

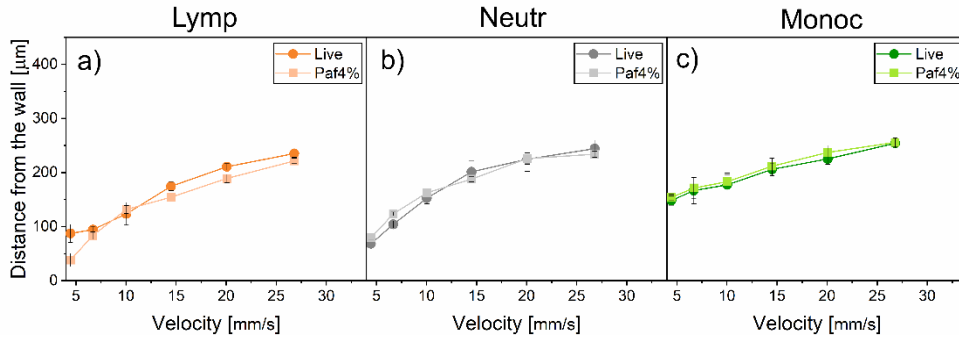


**Fig. 63** Comparison of the lateral displacement of a) Lymp live and Lymp fixed with Paf4%, b) Neutr live and Neutr with Paf 4% and c) monoc live and monoc with Paf4%, using PEO 0,4 at varying of velocity  $V_{max,B}$  from 4 mm/s to 30 mm/s.

#### 4.11 Digital holography microscope outcomes

We performed DHM using a camera module (CH-1014 DHM-Camera - LYNCEE) combined with an inverted microscope (IX71 - OLYMPUS), which record holograms produced by the interference between a reference wave and a wave emanating from the specimen (PBMC cells in our case). The captured image -40X objective full screen configuration of the camera module was transmitted to a computer. In our case the DHM was retrieved from an optical topography information recorded in a single image grab, without any scanning. Fig. 64 shows the preliminary results of the phase map intensity of all investigated cell types and also for a PSL 15 particle.

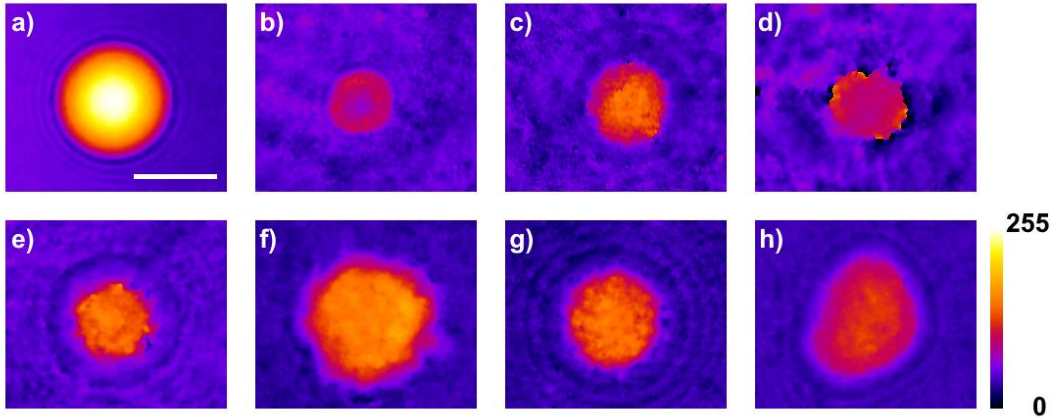


**Fig. 64** Phase map intensity for investigated cell and particles as followed: a) PSL15 particle, b) RBC, c) Lymph, d) Monoc, e) Neutr, f) MCF10a, g) MCF7 and h) MDA-MB-231. Length of scale bar is 10  $\mu\text{m}$ .

Fig. 64 Phase map intensity for investigated cell and particles as followed: a) PSL 15 particle, b) RBC, c) lymphocyte, d) monocyte, e) neutrophil, f) MCF-10A, g) MCF-7 and h) MDA-MB-231. Length of scale bar is 10  $\mu\text{m}$ . When light passes through an object with the optical path length  $s = h \times n$ , where  $h$  is the thickness and  $n$  the refractive index (RI) of the object, it experiences a phase shift  $\Delta\phi$  compared to light that does not pass this object.

$$\Delta\phi = \frac{2\pi}{\lambda_h} \Delta s \quad \text{Eq. 4.11-1}$$

where  $\Delta s$  is the optical path difference between these two light paths and  $\lambda_h$  is the wavelength of light in vacuum. In DHM measurements, the phase shift due to the cell  $\Delta\phi(x,y)$  is the quantity of interest. To measure this phase shift, the cell with an axially averaged RI distribution  $n_c(x,y)$ , an effective axial thickness profile  $h_c(x,y)$ , and a diameter  $d$  is suspended in a medium with a known RI  $n_m$  and is introduced into the object path of the setup. Hence, subtracting the phase shift of the background image from the phase shift measured with the cell in the field of view yields the cell specific phase shift  $\Delta\phi_c$ . Rewriting this difference results in an expression for the axially average RI of the cell at each lateral position:

$$n_c = n_m + \frac{\Delta\varphi_c \lambda_h}{2\pi h_c} \quad \text{Eq. 4.11-2}$$

Where  $h_c$  is the cell thickness. Knowing the thickness of the cell at each position, the integral RI for each pixel within the cell can be calculated. The RI value is proportional to mass density, so in general, the higher the phase map intensity corresponding to higher IR and the higher the phase shift. Therefore, we can correlate our outcomes directly with a higher optical density, which implies also a higher structural density[142]. The presented preliminary data do not calculate IR value and mass density. However, PSL 15 (see Fig. 64a) indicate the highest optical density as expected from literature. RBC which are illustrated in Fig. 64b shows the typical concave shape and the lowest phase map intensity (we can note the reduced phase intensity in the centre of the cell) from all investigated objects. Note that hydrogel investigations were not possible due to the insufficient signal to noise ratio for this kind of sample. However, we noticed significant high structural density for lymphocytes (see Fig. 64c) and also neutrophils (see Fig. 64e), which is in good agreement with our outcome. On the other side monocytes (see Fig. 64d) showed a significant lower structural complexity.

Furthermore, we measured the cell lines we investigate in this work. In such a case MCF-10a (see Fig. 64f) show the highest structural density, while MDA-MB-231 (see Fig. 64h) illustrated the lowest internal complexity. MCF-7 (see Fig. 64g) on the other side shows an intermediate optical structure. Such outcomes are in line with Youngs modulus values presented in this work and with microfluidic flow observations for cell separation presented with our device.

## ***5 Conclusions and future perspectives***

In our work, several contributions to the area of microfluidic cell sorting technology were made, utilizing inherent physical or mechanical cell properties. In particular, the variation of size and deformability in different cell types associated with fluid property changes were used to develop a novel cell sorting platform.

Briefly, a microfluidic device with specific cross-sections for cell as well as particle separation was designed and fabricated to first investigate particle separation mechanism in different viscoelastic flow conditions (fluid forces and velocities ranging from 10-50 mm/s) and afterwards applied our findings for cell type separation. Hereby the particles and cell positions were studied after 3D- fluid flow focusing ( $C_B$  section of the device), during the impact with a side-channel wall after bifurcation, following the particle migration to the centre line in downstream direction ( $C_C$  section of the device) and exploring the final channel position in a subsequent expansion region ( $C_D$  section of the device) before particle or cells are collected in distinct reservoir exits.

Our first results indicate that in  $C_B$  particles occupy an equilibrium position near to the centre of the microfluidic channel, while along  $C_C$  particle assume different lateral displacement positions in function of their size and the applied fluid flow condition. This result confirms previous assumptions [107, 124, 125] on straight microfluidic channel using similar suspension medium.

As previously mentioned, when particles or cells arrive at the bifurcation, they converge near to the inner wall in function of their biophysical properties. Afterwards according to the applied fluid condition cells migrate towards the centre of  $C_C$  with different migration velocities, which can be used to study the mechanical properties of them. In general, when viscoelastic fluid concentration increase, also the lateral displacement of particles or cells from the wall increase. Indeed, viscoelastic forces depend on relaxation time of viscoelastic fluid that increase with used PEO concentration. Moreover, acting fluid forces are maximized near to the

wall and decrease towards the centre promoting a well-defined migration of particles as well as cells. The hereby observed lateral displacement obtained in  $C_C$  of our microfluidic device was amplified in the subsequent expansion channel  $C_D$  to better investigate arising separation effects related to distinct particle or cell properties and moreover to separate them in flow.

Our results show a separation of PSL7, PSL10, PSL15 and PSL20 (number indicate nominal diameter of polystyrene beads) with a throughput of circa  $2 \times 10^5$  cell/h and purity over 97% using PEO 0,4 solution. Such outcome, to the best of our knowledge, is the highest throughput and efficiency among the current state of the art microfluidic particle separation methods to separate four types of particles simultaneously. We believe that, with further optimization of geometrical device parameters, channel ARs and PEO concentrations, our separation device would meet the requirements of high-throughput size-based separations for many biomedical and other applications. Compared with membrane filtration [126, 127], a major advantage of our device is that our platform does not suffer from clogging issue. But it shares the same limitation with other microfluidic technology [46, 128, 129] on the volume concentration. Therefore, in the current state our system is not applicable for sample concentration over  $2 \times 10^5$  particles/ml. The reason for this limitation is that high concentrate sample result in significant particle-particle interactions, which will interrupt the flow field in the microfluidic channel, and therefore the separation principle could be compromised [149].

As first application, our microfluidic device was utilized for the investigation of size-deformability based sorting. We measured the lateral displacement of epithelial, human breast cell lines (tumoral and benign) in  $C_C$  and  $C_D$  using MDA-MB-231, MCF-7 and MCF-10a and two significant PEO concentrations (PEO 0,2 and PEO 0,4) at five different velocities. Results indicated that for a  $V_{max,B}$  of 25 mm/s with PEO 0,4 we separate MDA-MB-231 from MCF-10a and MCF-7 obtaining a purity of 86,72% of MDA-MB-231 with an efficiency of 70,25%. We performed an analysis of AR of cells in  $C_B$ ,  $C_C$  (0 mm, 12,5mm and 25mm from the bifurcation)

and  $C_D$  and we found small MDA-MB-231 deformation was present in  $C_C$  using PEO 0,4, which was not present for MCF-7 and MCF-10a cells. Our results are in line with former reports that MCF-10a and MCF-7 cells are stiffer than MDA-MB-231 cells by analysing their magnitude of the Young's modulus [108],[109].

Furthermore, we studied in more detail the influence of particle deformability on the lateral displacement. For such experimental investigations, we produced hydrogel particles of different stiffness and analysed their lateral displacement for changing fluid flow conditions. Our preliminary results show that hydrogel particles with higher stiffness respond different to higher fluid flow forces allowing a separation of objects with different stiffness but similar size.

Next, we proofed the workability of our microfluidic platform for human blood cell type separation. Here our device achieved a RBC versus neutrophils separation efficiency of circa 90% as well as 78% for lymphocyte versus monocyte. At the best of our knowledge, this is the first time that in a microfluidic channel lymphocytes and monocytes are separated. Note that the efficiency of separation significantly drops down to 70% as soon as the cell concentration increase up to values of  $20 \times 10^5$  cell/ml.

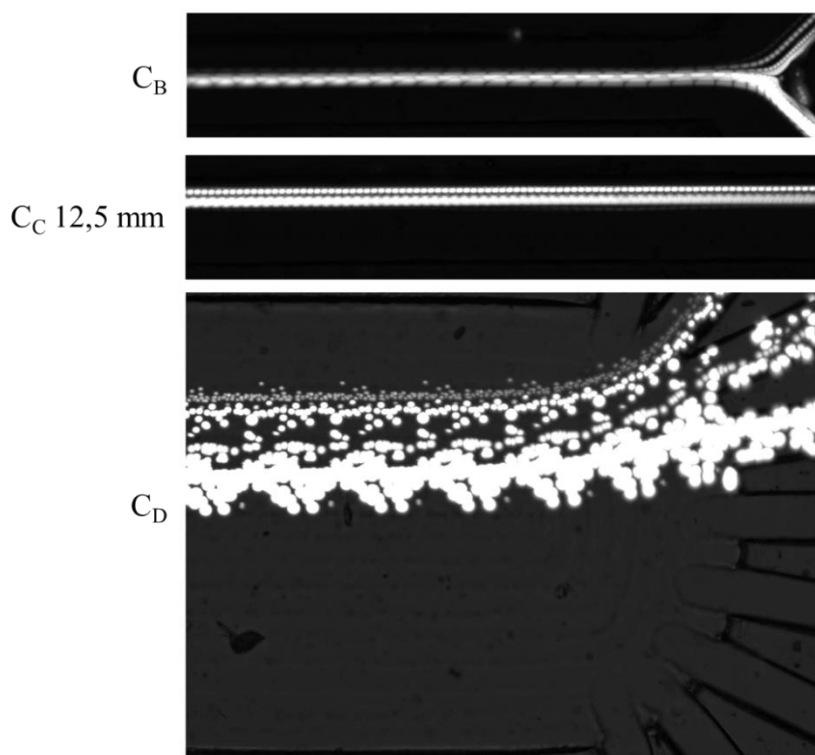
There are several factors that can affect the throughput, the purity and the efficiency of cell or particle separation as a non-homogeneity of dimension and mechanical properties in the same cell line, PEO concentration or applied velocity. Therefore, we showed preliminary outcomes of structural complexity of the investigated cells and particles using a digital holography approach. Our outcomes confirm that the structural complexity of an object significantly contribute to the lateral displacement of objects. Further investigations with non-spherical objects, different viscoelastic fluid conditions as well as different channel dimensions could even further improve our separation performance and final cell throughput. In addition, we believe that our microfluidic separation platform can be from significant interest for circulating tumour cell separation.



## *Supplementary materials*

### *Figure S 1*

Image of particles in microfluidic device  $C_B$ ,  $C_C$  at 0mm and 12,5 mm,  $C_D$  using PEO 0,4 at the velocity of 25 mm/s.



### *Video SICB*

*Polystyrene latex with different dimension ( $7\mu\text{m}$ ,  $10\mu\text{m}$ ,  $15\mu\text{m}$  and  $20\mu\text{m}$ ) in flow in  $C_B$  using PEO 0,4 at  $V_{\text{max},B}=25\text{mm/s}$ .*

<https://www.dropbox.com/s/tgd91pkrk7qgs4b/SICB.avi?dl=0>

### *Video SICC*

*Polystyrene latex with different dimension ( $7\mu\text{m}$ ,  $10\mu\text{m}$ ,  $15\mu\text{m}$  and  $20\mu\text{m}$ ) in flow in  $C_C$  (12,5 mm) using PEO 0,4 at  $V_{\text{max},B}=25\text{mm/s}$ .*

<https://www.dropbox.com/s/6fxm2deaf1wug9g/SICC.avi?dl=0>

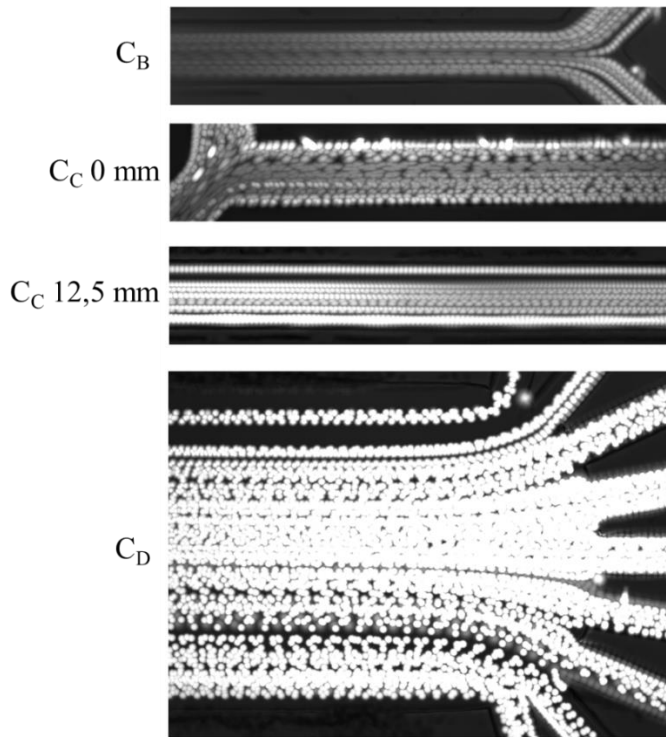
### *Video SICD*

*Polystyrene latex with different dimension (7 $\mu$ m, 10 $\mu$ m, 15 $\mu$ m and 20  $\mu$ m) in flow in  $C_D$  using PEO 0,4 at  $V_{max,B}=25$ mm/s.*

<https://www.dropbox.com/s/gnauq4p8h8qd1yj/S1CD.avi?dl=0>

### **Figure S 2**

Image of particles in microfluidic device  $C_B$ ,  $C_C$  at 0mm and 12,5 mm,  $C_D$  using Gly70% at the velocity of 40mm/s.



### **Video S2CB**

*Polystyrene latex with different dimension (7 $\mu$ m, 10 $\mu$ m, 15 $\mu$ m and 20  $\mu$ m) in flow in  $C_B$  using Gly70% at  $V_{max,B}=40$ mm/s.*

<https://www.dropbox.com/s/52rkm6vviamrxf/S2CB.avi?dl=0>

### **Video S2CC**

*Polystyrene latex with different dimension (7 $\mu$ m, 10 $\mu$ m, 15 $\mu$ m and 20  $\mu$ m) in flow in  $C_C$  (12,5mm) using Gly70% at  $V_{max,B}=40$ mm/s.*

<https://www.dropbox.com/s/caik03r7l9visuk/S2CC.avi?dl=0>

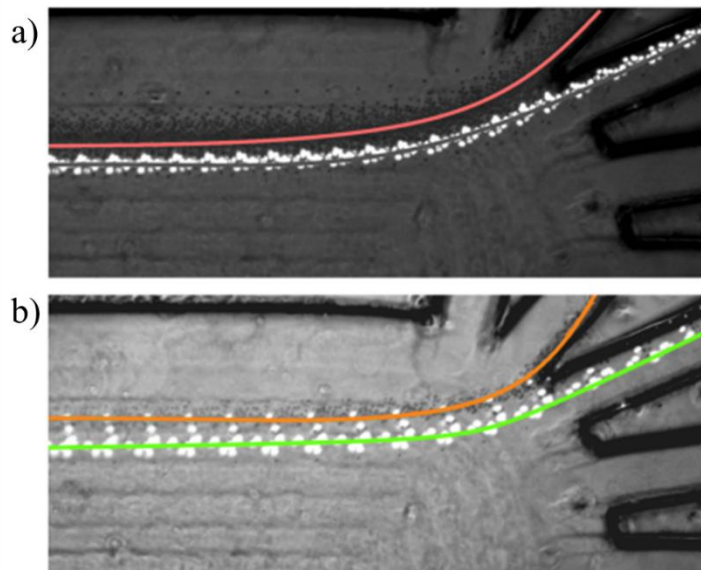
**Video S2CD**

Polystyrene latex with different dimension ( $7\mu\text{m}$ ,  $10\mu\text{m}$ ,  $15\mu\text{m}$  and  $20\mu\text{m}$ ) in flow in  $C_D$  using Gly70% at  $V_{\text{max},B}=40\text{mm/s}$ .

[https://www.dropbox.com/s/zlp74sxn6a2ih3/S2\\_CD.avi?dl=0](https://www.dropbox.com/s/zlp74sxn6a2ih3/S2_CD.avi?dl=0)

**Figure S3**

Image of separation between a) RBC (red) and Neutr (grey), and b) Monoc (green) and Lymp (orange) in  $C_D$  using PEO 0,4. In a) and b) the  $V_{\text{max},B}$  are 20 mm/s and 15 mm/s respectively.



**Video S3a**

RBC-Neutr separation using PEO 0,4 at  $V_{\text{max},B}$  20 mm/s.

<https://www.dropbox.com/s/s1ecqtac0nfxcdr/S3a.avi?dl=0>

**Video S3b**

Lymp-Monoc separation using PEO 0,4 at  $V_{\text{max},B}$  15 mm/s

<https://www.dropbox.com/s/6lc23ymlvixmb73/S3b.avi?dl=0>

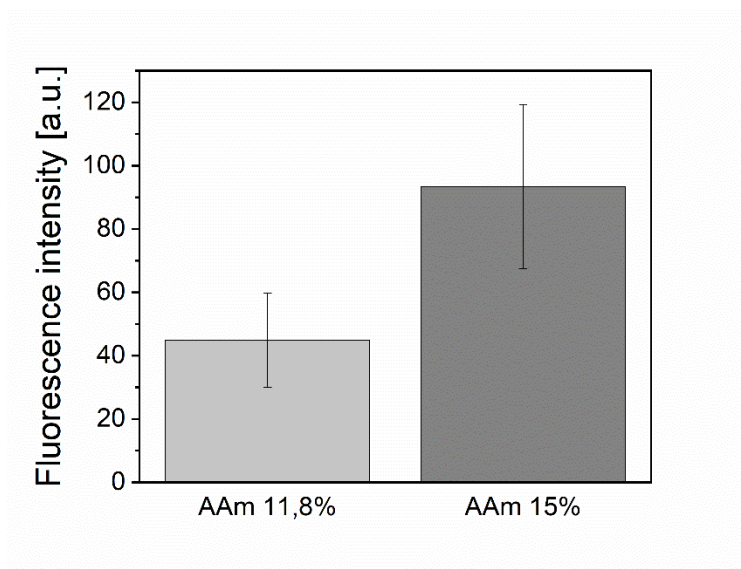
### ***Video droplet generation***

At follow link it is possible see the droplet generation of particles  $C_T$  11,8% with a diameter in flow of 10  $\mu\text{m}$  and swelled diameter of 14,3  $\mu\text{m}$ .

Link: [https://www.dropbox.com/s/juzqnjqueys0fz2/Droplet\\_generation\\_.avi?dl=0](https://www.dropbox.com/s/juzqnjqueys0fz2/Droplet_generation_.avi?dl=0)

### ***Figure S 4***

Fluorescence intensity of AAm 11,8% and AAm 15% with similar diameter. AAm 15% shows a higher fluorescence intensity then AAm11,8% because more quantitative of AAm which binds at the ATTO.



### ***Video S5\_CC\_0***

At follow link it is possible see the PSL15-cell flow in  $C_C$  at 0 mm at  $V_{\text{max},B}$  of 25 mm/s.

[https://www.dropbox.com/s/9wna2ldhw1ay9rc/S5\\_CC\\_0mm.avi?dl=0](https://www.dropbox.com/s/9wna2ldhw1ay9rc/S5_CC_0mm.avi?dl=0)

### ***Video S5\_CC\_12mm***

At follow link it is possible see the PSL15-cell flow in  $C_C$  at 12,5 mm at  $V_{\max,B}$  of 25 mm/s.

[https://www.dropbox.com/s/qqk787a1uifhdzc/S5\\_CC\\_12mm.avi?dl=0](https://www.dropbox.com/s/qqk787a1uifhdzc/S5_CC_12mm.avi?dl=0)

### ***Video S5\_CC\_25mm***

At follow link it is possible see the PSL15-cell flow in  $C_C$  at 25 mm at  $V_{\max,B}$  of 25 mm/s.

[https://www.dropbox.com/s/grnm8dx27kcewg8/S5\\_CC\\_25mm.avi?dl=0](https://www.dropbox.com/s/grnm8dx27kcewg8/S5_CC_25mm.avi?dl=0)

## Reference

- [1] D. Di Carlo and L. P. Lee, "Dynamic single-cell analysis for quantitative biology," *Analytical Chemistry*, vol. 78, no. 23. American Chemical Society, pp. 7918–7925, Dec. 01, 2006, doi: 10.1021/ac069490p.
- [2] D. Anselmetti, *Single Cell Analysis: Technologies and Applications*. Wiley-VCH, 2009.
- [3] D. G. Iorgulescu and G. K. Kiroff, "Minimal Residual Marrow Disease: Detection and significance of isolated tumour cells in bone marrow," *ANZ Journal of Surgery*, vol. 71, no. 6. Blackwell Publishing, pp. 365–376, Jun. 08, 2001, doi: 10.1046/j.1440-1622.2001.02110.x.
- [4] F. A. Vlems, T. Wobbes, C. J. A. Punt, and G. N. P. Van Muijen, "Detection and clinical relevance of tumor cells in blood and bone marrow of patients with colorectal cancer," *Anticancer Research*, vol. 23, no. 1 B. pp. 523–530, Jan. 01, 2003, Accessed: Jun. 16, 2021. [Online]. Available: <https://europepmc.org/article/med/12680140>.
- [5] M. J. Stuart and R. L. Nagel, "Sickle-cell disease," in *Lancet*, Oct. 2004, vol. 364, no. 9442, pp. 1343–1360, doi: 10.1016/S0140-6736(04)17192-4.
- [6] C. W. Rinker-Schaeffer, A. W. Partin, W. B. Isaacs, D. S. Coffey, and J. T. Isaacs, "Molecular and cellular changes associated with the acquisition of metastatic ability by prostatic cancer cells," *Prostate*, vol. 25, no. 5, pp. 249–265, 1994, doi: 10.1002/pros.2990250505.
- [7] K. J. Pienta and D. S. Coffey, "Nuclear-Cytoskeletal interactions: Evidence for physical connections between the nucleus and cell periphery and their alteration by transformation," *J. Cell. Biochem.*, vol. 49, no. 4, pp. 357–365, 1992, doi: 10.1002/jcb.240490406.
- [8] "Nuclear dreams: The malignant alteration of nuclear architecture." <https://onlinelibrary.wiley.com/doi/epdf/10.1002/%28SICI%291097-4644%2819980801%2970%3A2%3C172%3A%3AAID-JCB3%3E3.0.CO%3B2-L> (accessed Jun. 16, 2021).
- [9] G. Pawlak and D. M. Helfman, "Cytoskeletal changes in cell transformation and tumorigenesis," *Current Opinion in Genetics and Development*, vol. 11, no. 1. Elsevier Ltd, pp. 41–47, Feb. 01, 2001, doi: 10.1016/S0959-437X(00)00154-4.
- [10] B. R. Konety and R. H. Getzenberg, "Nuclear Structural Proteins as Biomarkers of Cancer," 1999. doi: 10.1002/(SICI)1097-4644(1999)75:32.
- [11] D. L. Polla *et al.*, "Microdevices in medicine," *Annu. Rev. Biomed. Eng.*, vol. 2, no. 2000, pp. 551–576, 2000, doi: 10.1146/annurev.bioeng.2.1.551.
- [12] "Sorting biomolecules with microdevices - Lunds universitet." [https://portal.research.lu.se/portal/sv/publications/sorting-biomolecules-with-microdevices\(5b577569-7706-4bf5-8d74-d039bb93f155\)/export.html](https://portal.research.lu.se/portal/sv/publications/sorting-biomolecules-with-microdevices(5b577569-7706-4bf5-8d74-d039bb93f155)/export.html) (accessed Jun. 16, 2021).
- [13] T. M. H. Lee, I. M. Hsing, A. I. K. Lao, and M. C. Carles, "A miniaturized DNA amplifier: Its application in traditional Chinese medicine," *Anal. Chem.*, vol. 72, no. 17, pp. 4242–4247, Sep. 2000, doi: 10.1021/ac000384b.
- [14] J. L. Simpson and S. Elias, "Isolating Fetal Cells From Maternal Blood: Advances in Prenatal Diagnosis Through Molecular Technology," *JAMA J. Am. Med. Assoc.*,

- vol. 270, no. 19, pp. 2357–2361, Nov. 1993, doi: 10.1001/jama.1993.03510190113036.
- [15] R. M. McCormick, R. J. Nelson, M. G. Alonso-Amigo, D. J. Benvegna, and H. H. Hooper, “Microchannel Electrophoretic Separations of DNA in Injection-Molded Plastic Substrates,” *Anal. Chem.*, vol. 69, no. 14, pp. 2626–2630, Jul. 1997, doi: 10.1021/ac9701997.
- [16] E. T. Lagally, I. Medintz, and R. A. Mathies, “Single-molecule DNA amplification and analysis in an integrated microfluidic device,” *Anal. Chem.*, vol. 73, no. 3, pp. 565–570, Feb. 2001, doi: 10.1021/ac001026b.
- [17] J. J. Chalmers, M. Zborowski, L. Sun, and L. Moore, “Flow through, immunomagnetic cell separation,” *Biotechnol. Prog.*, vol. 14, no. 1, pp. 141–148, 1998, doi: 10.1021/bp970140l.
- [18] S. Basu, H. M. Campbell, B. N. Dittel, and A. Ray, “Purification of specific cell population by fluorescence activated cell sorting (FACS),” *J. Vis. Exp.*, no. 41, pp. 3–6, 2010, doi: 10.3791/1546.
- [19] S. Technique, “Density Gradient Centrifugation : Isolation of ( Z-3-Octanol from American Oil of,” vol. 341, no. 4, pp. 1847–1848, 1951.
- [20] H. Elispot, *ELISPO Handbook*. .
- [21] R. G. Miller and R. A. Phillips, “Separation of cells by velocity sedimentation,” *J. Cell. Physiol.*, vol. 73, no. 3, pp. 191–201, 1969, doi: 10.1002/jcp.1040730305.
- [22] C. D. Helgason and C. Miller, *Basic Cell Culture Protocols*. 2004.
- [23] C. Wyatt Shields Iv, C. D. Reyes, and G. P. López, “Microfluidic cell sorting: A review of the advances in the separation of cells from debulking to rare cell isolation,” *Lab Chip*, vol. 15, no. 5, pp. 1230–1249, 2015, doi: 10.1039/c4lc01246a.
- [24] F. Del Giudice, G. Romeo, G. D’Avino, F. Greco, P. A. Netti, and P. L. Maffettone, “Particle alignment in a viscoelastic liquid flowing in a square-shaped microchannel,” *Lab Chip*, vol. 13, no. 21, pp. 4263–4271, 2013, doi: 10.1039/c3lc50679g.
- [25] C. Liberale *et al.*, “Integrated microfluidic device for single-cell trapping and spectroscopy,” *Sci. Rep.*, vol. 3, 2013, doi: 10.1038/srep01258.
- [26] C. Church, J. Zhu, G. Huang, T. R. Tzeng, and X. Xuan, “Integrated electrical concentration and lysis of cells in a microfluidic chip,” *Biomicrofluidics*, vol. 4, no. 4, 2010, doi: 10.1063/1.3496358.
- [27] J. P. Beech, S. H. Holm, K. Adolfsson, and J. O. Tegenfeldt, “Sorting cells by size, shape and deformability,” *Lab Chip*, vol. 12, no. 6, pp. 1048–1051, 2012, doi: 10.1039/c2lc21083e.
- [28] C. M. Yousuff, E. T. W. Ho, K. Ismail Hussain, and N. H. B. Hamid, “Microfluidic platform for cell isolation and manipulation based on cell properties,” *Micromachines*, vol. 8, no. 1, 2017, doi: 10.3390/mi8010015.
- [29] L. Zeng, S. Balachandar, and P. Fischer, “Wall-induced forces on a rigid sphere at finite Reynolds number,” *J. Fluid Mech.*, vol. 536, pp. 1–25, Aug. 2005, doi: 10.1017/S0022112005004738.
- [30] L. Zeng, F. Najjar, S. Balachandar, and P. Fischer, “Forces on a finite-sized particle located close to a wall in a linear shear flow,” *Phys. Fluids*, vol. 21, no. 3, p. 033302, Mar. 2009, doi: 10.1063/1.3082232.
- [31] D. Di Carlo, “Inertial microfluidics,” *Lab on a Chip*, vol. 9, no. 21. Royal Society of Chemistry, pp. 3038–3046, Nov. 07, 2009, doi: 10.1039/b912547g.

- [32] J. M. Martel and M. Toner, "Inertial focusing in microfluidics," *Annual Review of Biomedical Engineering*, vol. 16. Annual Reviews Inc., pp. 371–396, Jul. 11, 2014, doi: 10.1146/annurev-bioeng-121813-120704.
- [33] J. Zhang *et al.*, "Fundamentals and applications of inertial microfluidics: A review," *Lab Chip*, vol. 16, no. 1, pp. 10–34, 2016, doi: 10.1039/c5lc01159k.
- [34] E. S. Asmolov, "The inertial lift on a spherical particle in a plane poiseuille flow at large channel Reynolds number," *J. Fluid Mech.*, vol. 381, no. 1, pp. 63–87, Feb. 1999, doi: 10.1017/S0022112098003474.
- [35] J. Zhou and I. Papautsky, "Viscoelastic microfluidics: progress and challenges," *Microsystems Nanoeng.*, vol. 6, no. 1, 2020, doi: 10.1038/s41378-020-00218-x.
- [36] S. S. Kuntaegowdanahalli, A. A. S. Bhagat, G. Kumar, and I. Papautsky, "Inertial microfluidics for continuous particle separation in spiral microchannels," *Lab Chip*, vol. 9, no. 20, pp. 2973–2980, 2009, doi: 10.1039/b908271a.
- [37] T. Petersson, Filip; Aberg, Lena; Sward-Nilsson, Ann-Margret; Laurell, "Free Flow Acoustophoresis: Microfluidic-Based Mode of Particle and Cell Separation," *Anal. Chem.*, vol. 79, 2007.
- [38] S. Gupta, D. L. Feke, and I. Manas-Zloczower, "Fractionation of mixed particulate solids according to compressibility using ultrasonic standing wave fields," *Chem. Eng. Sci.*, vol. 50, no. 20, pp. 3275–3284, 1995, doi: 10.1016/0009-2509(95)00154-W.
- [39] J. Shi, H. Huang, Z. Stratton, Y. Huang, and T. J. Huang, "Continuous particle separation in a microfluidic channel via standing surface acoustic waves (SSAW)," *Lab Chip*, vol. 9, no. 23, pp. 3354–3359, 2009, doi: 10.1039/b915113c.
- [40] D. A. Johnson and D. L. Feke, "Methodology for fractionating suspended particles using ultrasonic standing wave and divided flow fields," *Sep. Technol.*, vol. 5, no. 4, pp. 251–258, 1995, doi: 10.1016/0956-9618(95)00130-1.
- [41] H. A. Pohl, "The motion and precipitation of suspensoids in divergent electric fields," *J. Appl. Phys.*, vol. 22, no. 7, pp. 869–871, 1951, doi: 10.1063/1.1700065.
- [42] D. Flow-, D. Holmes, and N. G. Green, "Microdevices for," no. December, pp. 85–90, 2003.
- [43] J. Gascoyne, Peter R. C.; Vykoukal, "Particle separation by dielectrophoresis," *Electrophoresis*, 2002.
- [44] D. W. Inglis, R. Riehn, J. C. Sturm, and R. H. Austin, "Microfluidic high gradient magnetic cell separation," *J. Appl. Phys.*, vol. 99, no. 8, pp. 2004–2007, 2006, doi: 10.1063/1.2165782.
- [45] K. H. Han and A. Bruno Frazier, "Continuous magnetophoretic separation of blood cells in microdevice format," *J. Appl. Phys.*, vol. 96, no. 10, pp. 5797–5802, 2004, doi: 10.1063/1.1803628.
- [46] K. Y. Castillo-Torres, E. S. McLamore, and D. P. Arnold, "A high-throughput microfluidic magnetic separation ( $\mu$ FMS) platform for water quality monitoring," *Micromachines*, vol. 11, no. 1, pp. 1–13, 2020, doi: 10.3390/mi11010016.
- [47] M. P. MacDonald, G. C. Spalding, and K. Dholakia, "Microfluidic sorting in an optical lattice," *Nature*, vol. 426, no. 6965, pp. 421–424, 2003, doi: 10.1038/nature02144.
- [48] H. Tsutsui and C. M. Ho, "Cell separation by non-inertial force fields in microfluidic systems," *Mech. Res. Commun.*, vol. 36, no. 1, pp. 92–103, 2009, doi: 10.1016/j.mechrescom.2008.08.006.

- [49] D. Di Carlo, D. Irimia, R. G. Tompkins, and M. Toner, "Continuous inertial focusing, ordering, and separation of particles in microchannels," *Proc. Natl. Acad. Sci. U. S. A.*, vol. 104, no. 48, pp. 18892–18897, 2007, doi: 10.1073/pnas.0704958104.
- [50] J. Zhou and I. Papautsky, "Fundamentals of inertial focusing in microchannels," *Lab Chip*, vol. 13, no. 6, pp. 1121–1132, 2013, doi: 10.1039/c2lc41248a.
- [51] G. Silberber. A. Segré, "Radial particle displacement in Poiseuille flow of suspension," *Nature*, vol. 189, 1961.
- [52] J. P. Matas, J. F. Morris, and É. Guazzelli, "Inertial migration of rigid spherical particles in Poiseuille flow," *J. Fluid Mech.*, vol. 515, pp. 171–195, 2004, doi: 10.1017/S0022112004000254.
- [53] Y. S. Choi, K. W. Seo, and S. J. Lee, "Lateral and cross-lateral focusing of spherical particles in a square microchannel," *Lab Chip*, vol. 11, no. 3, pp. 460–465, 2011, doi: 10.1039/c0lc00212g.
- [54] A. J. Chung, D. R. Gossett, and D. Di Carlo, "Three dimensional, sheathless, and high-throughput microparticle inertial focusing through geometry-induced secondary flows," *Small*, vol. 9, no. 5, pp. 685–690, 2013, doi: 10.1002/smll.201202413.
- [55] A. J. Mach and D. di Carlo, "Continuous scalable blood filtration device using inertial microfluidics," *Biotechnol. Bioeng.*, vol. 107, no. 2, pp. 302–311, 2010, doi: 10.1002/bit.22833.
- [56] S. C. Hur, T. Z. Brinckerhoff, C. M. Walthers, J. C. Y. Dunn, and D. Di Carlo, "Label-Free Enrichment of Adrenal Cortical Progenitor Cells Using Inertial Microfluidics," *PLoS One*, vol. 7, no. 10, 2012, doi: 10.1371/journal.pone.0046550.
- [57] J. Zhou, P. V. Giridhar, S. Kasper, and I. Papautsky, "Modulation of aspect ratio for complete separation in an inertial microfluidic channel," *Lab Chip*, vol. 13, no. 10, pp. 1919–1929, 2013, doi: 10.1039/c3lc50101a.
- [58] D. Di Carlo, "Inertial microfluidics," *Lab Chip*, vol. 9, no. 21, pp. 3038–3046, 2009, doi: 10.1039/b912547g.
- [59] A. A. S. Bhagat, S. S. Kuntaegowdanahalli, and I. Papautsky, "Continuous particle separation in spiral microchannels using dean flows and differential migration," *Lab Chip*, vol. 8, no. 11, pp. 1906–1914, 2008, doi: 10.1039/b807107a.
- [60] H. W. Hou *et al.*, "Isolation and retrieval of circulating tumor cells using centrifugal forces," *Sci. Rep.*, vol. 3, pp. 1–8, 2013, doi: 10.1038/srep01259.
- [61] C. Mohamed Yousuff, N. H. B Hamid, I. H. Kamal Basha, and E. T. Wei Ho, "Output channel design for collecting closely-spaced particle streams from spiral inertial separation devices," *AIP Adv.*, vol. 7, no. 8, 2017, doi: 10.1063/1.4986617.
- [62] F. Ghadami, Sepehr; Kowsari-Esfahan, Reza; Saidi, Mohammad Said ; Keykhosrow, "Spiral microchannel with stair-like cross section for size-based," *Microfluid Nanofluid*, 2017.
- [63] H. Chen, "A Triplet Parallelizing Spiral Microfluidic Chip for Continuous Separation of Tumor Cells," *Sci. Rep.*, vol. 8, no. 1, pp. 1–8, 2018, doi: 10.1038/s41598-018-22348-z.
- [64] J. Son, A. R. Jafek, D. T. Carrell, J. M. Hotaling, and B. K. Gale, "Sperm-like-particle (SLP) behavior in curved microfluidic channels," *Microfluid. Nanofluidics*, vol. 23, no. 1, pp. 1–13, 2019, doi: 10.1007/s10404-018-2170-1.
- [65] D. Yuan *et al.*, "Dean-flow-coupled elasto-inertial particle and cell focusing in

- symmetric serpentine microchannels,” *Microfluid. Nanofluidics*, vol. 23, no. 3, pp. 1–9, 2019, doi: 10.1007/s10404-019-2204-3.
- [66] M. G. Lee, S. Choi, and J. K. Park, “Inertial separation in a contraction-expansion array microchannel,” *J. Chromatogr. A*, vol. 1218, no. 27, pp. 4138–4143, 2011, doi: 10.1016/j.chroma.2010.11.081.
- [67] M. G. Lee *et al.*, “Inertial blood plasma separation in a contraction-expansion array microchannel,” *Appl. Phys. Lett.*, vol. 98, no. 25, pp. 2012–2015, 2011, doi: 10.1063/1.3601745.
- [68] M. G. Lee, J. H. Shin, C. Y. Bae, S. Choi, and J. K. Park, “Label-free cancer cell separation from human whole blood using inertial microfluidics at low shear stress,” *Anal. Chem.*, vol. 85, no. 13, pp. 6213–6218, 2013, doi: 10.1021/ac4006149.
- [69] J. S. Park, S. H. Song, and H. Il Jung, “Continuous focusing of microparticles using inertial lift force and vorticity via multi-orifice microfluidic channels,” *Lab Chip*, vol. 9, no. 7, pp. 939–948, Apr. 2009, doi: 10.1039/b813952k.
- [70] L. Liu, L. Han, X. Shi, W. Tan, W. Cao, and G. Zhu, “Hydrodynamic separation by changing equilibrium positions in contraction–expansion array channels,” *Microfluid. Nanofluidics*, vol. 23, no. 4, pp. 1–12, 2019, doi: 10.1007/s10404-019-2219-9.
- [71] H. S. Moon *et al.*, “Continuous separation of breast cancer cells from blood samples using multi-orifice flow fractionation (MOFF) and dielectrophoresis (DEP),” in *Lab on a Chip*, Mar. 2011, vol. 11, no. 6, pp. 1118–1125, doi: 10.1039/c0lc00345j.
- [72] B. Kwak *et al.*, “Hydrodynamic blood cell separation using fishbone shaped microchannel for circulating tumor cells enrichment,” *Sensors Actuators, B Chem.*, vol. 261, pp. 38–43, 2018, doi: 10.1016/j.snb.2018.01.135.
- [73] L. Zhao, Qianbin; Yuan, Dan; Yan, Sheng; Zhang, Jun; Du, Haiping; Alici, Gursel; Weihua, “Flow rate-insensitive microparticle separation and filtration using a microchannel with arc-shaped groove arrays,” *Microfluid Nanofluid*, 2017.
- [74] B. P. Ho and L. G. Leal, “Migration of rigid spheres in a two-dimensional unidirectional shear flow of a second-order fluid,” *J. Fluid Mech.*, vol. 76, no. 4, pp. 783–799, 1976, doi: 10.1017/S002211207600089X.
- [75] P. Y. Huang, J. Feng, H. H. Hu, and D. D. Joseph, “Direct simulation of the motion of solid particles in Couette and Poiseuille flows of viscoelastic fluids,” *J. Fluid Mech.*, vol. 343, pp. 73–94, 1997, doi: 10.1017/S0022112097005764.
- [76] K. Kang, S. S. Lee, K. Hyun, S. J. Lee, and J. M. Kim, “DNA-based highly tunable particle focuser,” *Nat. Commun.*, vol. 4, no. 1, pp. 1–8, Oct. 2013, doi: 10.1038/ncomms3567.
- [77] S. Yang, J. Y. Kim, S. J. Lee, S. S. Lee, and J. M. Kim, “Sheathless elasto-inertial particle focusing and continuous separation in a straight rectangular microchannel,” *Lab Chip*, vol. 11, no. 2, pp. 266–273, 2011, doi: 10.1039/c0lc00102c.
- [78] E. J. Lim *et al.*, “Inertio-elastic focusing of bioparticles in microchannels at high throughput,” *Nat. Commun.*, vol. 5, no. May, 2014, doi: 10.1038/ncomms5120.
- [79] J. Nam, H. Lim, D. Kim, H. Jung, and S. Shin, “Continuous separation of microparticles in a microfluidic channel via the elasto-inertial effect of non-Newtonian fluid,” *Lab Chip*, vol. 12, no. 7, pp. 1347–1354, 2012, doi: 10.1039/c2lc21304d.

- [80] H. Lim, J. Nam, and S. Shin, "Lateral migration of particles suspended in viscoelastic fluids in a microchannel flow," *Microfluid. Nanofluidics*, vol. 17, no. 4, pp. 683–692, 2014, doi: 10.1007/s10404-014-1353-7.
- [81] M. Yamada, M. Nakashima, and M. Seki, "Pinched flow fractionation: Continuous size separation of particles utilizing a laminar flow profile in a pinched microchannel," *Anal. Chem.*, vol. 76, no. 18, pp. 5465–5471, 2004, doi: 10.1021/ac049863r.
- [82] X. Lu and X. Xuan, "Continuous Microfluidic Particle Separation via Elasto-Inertial Pinched Flow Fractionation," *Anal. Chem.*, vol. 87, no. 12, pp. 6389–6396, 2015, doi: 10.1021/acs.analchem.5b01432.
- [83] S. W. Ahn, S. S. Lee, S. J. Lee, and J. M. Kim, "Microfluidic particle separator utilizing sheathless elasto-inertial focusing," *Chem. Eng. Sci.*, vol. 126, pp. 237–243, 2015, doi: 10.1016/j.ces.2014.12.019.
- [84] J. Nam *et al.*, "Microfluidic device for sheathless particle focusing and separation using a viscoelastic fluid," *J. Chromatogr. A*, vol. 1406, pp. 244–250, 2015, doi: 10.1016/j.chroma.2015.06.029.
- [85] J. Nam *et al.*, "Hybrid capillary-inserted microfluidic device for sheathless particle focusing and separation in viscoelastic flow," *Biomicrofluidics*, vol. 9, no. 6, 2015, doi: 10.1063/1.4938389.
- [86] J. Nam, Y. Shin, J. K. S. Tan, Y. B. Lim, C. T. Lim, and S. Kim, "High-throughput malaria parasite separation using a viscoelastic fluid for ultrasensitive PCR detection," *Lab Chip*, vol. 16, no. 11, pp. 2086–2092, 2016, doi: 10.1039/c6lc00162a.
- [87] X. Lu and X. Xuan, "Elasto-Inertial Pinched Flow Fractionation for Continuous Shape-Based Particle Separation," *Anal. Chem.*, vol. 87, no. 22, pp. 11523–11530, 2015, doi: 10.1021/acs.analchem.5b03321.
- [88] S. Yang *et al.*, "Deformability-selective particle entrainment and separation in a rectangular microchannel using medium viscoelasticity," *Soft Matter*, vol. 8, no. 18, pp. 5011–5019, 2012, doi: 10.1039/c2sm07469a.
- [89] M. Yamada and M. Seki, "Hydrodynamic filtration for on-chip particle concentration and classification utilizing microfluidics," *Lab Chip*, vol. 5, no. 11, pp. 1233–1239, 2005, doi: 10.1039/b509386d.
- [90] P. Sajeesh and A. K. Sen, "Particle separation and sorting in microfluidic devices: A review," *Microfluid. Nanofluidics*, vol. 17, no. 1, pp. 1–52, 2014, doi: 10.1007/s10404-013-1291-9.
- [91] Y. Y. Chiu, C. K. Huang, and Y. W. Lu, "Enhancement of microfluidic particle separation using cross-flow filters with hydrodynamic focusing," *Biomicrofluidics*, vol. 10, no. 1, pp. 1–13, 2016, doi: 10.1063/1.4939944.
- [92] M. Kersaudy-Kerhoas, R. Dhariwal, M. P. Y. Desmulliez, and L. Jouvét, "Hydrodynamic blood plasma separation in microfluidic channels," *Microfluid. Nanofluidics*, vol. 8, no. 1, pp. 105–114, 2010, doi: 10.1007/s10404-009-0450-5.
- [93] M. Matsuda, M. Yamada, and M. Seki, "Blood cell classification utilizing hydrodynamic filtration," *Electron. Commun. Japan*, vol. 94, no. 1, pp. 1–6, 2011, doi: 10.1002/ecj.10281.
- [94] M. Mizuno, M. Yamada, R. Mitamura, K. Ike, K. Toyama, and M. Seki, "Magnetophoresis-integrated hydrodynamic filtration system for size-and surface marker-based two-dimensional cell sorting," *Anal. Chem.*, vol. 85, no. 16, pp.

- 7666–7673, 2013, doi: 10.1021/ac303336f.
- [95] V. Kumar and P. Rezai, “Magneto-Hydrodynamic Fractionation (MHF) for continuous and sheathless sorting of high-concentration paramagnetic microparticles,” *Biomed. Microdevices*, vol. 19, no. 2, 2017, doi: 10.1007/s10544-017-0178-z.
- [96] S. Choi and J. K. Park, “Continuous hydrophoretic separation and sizing of microparticles using slanted obstacles in a microchannel,” *Lab Chip*, vol. 7, no. 7, pp. 890–897, 2007, doi: 10.1039/b701227f.
- [97] S. Choi, S. Song, C. Choi, and J. K. Park, “Continuous blood cell separation by hydrophoretic filtration,” *Lab Chip*, vol. 7, no. 11, pp. 1532–1538, 2007, doi: 10.1039/b705203k.
- [98] D. W. Inglis, J. A. Davis, R. H. Austin, and J. C. Sturm, “Critical particle size for fractionation by deterministic lateral displacement,” *Lab Chip*, vol. 6, no. 5, pp. 655–658, 2006, doi: 10.1039/b515371a.
- [99] L. R. Huang, E. C. Cox, R. H. Austin, and J. C. Sturm, “Continuous Particle Separation Through Deterministic Lateral Displacement,” *Science (80-. )*, vol. 304, no. 5673, pp. 987–990, 2004, doi: 10.1126/science.1094567.
- [100] J. A. Davis *et al.*, “Deterministic hydrodynamics: Taking blood apart,” *Proc. Natl. Acad. Sci. U. S. A.*, vol. 103, no. 40, pp. 14779–14784, 2006, doi: 10.1073/pnas.0605967103.
- [101] Z. Liu *et al.*, “Rapid isolation of cancer cells using microfluidic deterministic lateral displacement structure,” *Biomicrofluidics*, vol. 7, no. 1, pp. 1–10, 2013, doi: 10.1063/1.4774308.
- [102] K. Louthback, K. S. Chou, J. Newman, J. Puchalla, R. H. Austin, and J. C. Sturm, “Improved performance of deterministic lateral displacement arrays with triangular posts,” *Microfluid. Nanofluidics*, vol. 9, no. 6, pp. 1143–1149, 2010, doi: 10.1007/s10404-010-0635-y.
- [103] B. M. Dincau, A. Aghilinejad, X. Chen, S. Y. Moon, and J. H. Kim, “Vortex-free high-Reynolds deterministic lateral displacement (DLD) via airfoil pillars,” *Microfluid. Nanofluidics*, vol. 22, no. 12, pp. 1–9, 2018, doi: 10.1007/s10404-018-2160-3.
- [104] K. K. Zeming, S. Ranjan, and Y. Zhang, “Rotational separation of non-spherical bioparticles using I-shaped pillar arrays in a microfluidic device,” *Nat. Commun.*, vol. 4, pp. 1–8, 2013, doi: 10.1038/ncomms2653.
- [105] S. Ranjan, K. K. Zeming, R. Jureen, D. Fisher, and Y. Zhang, “DLD pillar shape design for efficient separation of spherical and non-spherical bioparticles,” *Lab Chip*, vol. 14, no. 21, pp. 4250–4262, 2014, doi: 10.1039/c4lc00578c.
- [106] S. H. Au *et al.*, “Microfluidic isolation of circulating tumor cell clusters by size and asymmetry,” *Sci. Rep.*, vol. 7, no. 1, pp. 1–10, 2017, doi: 10.1038/s41598-017-01150-3.
- [107] J. chul Hyun, J. Hyun, S. Wang, and S. Yang, “Improved pillar shape for deterministic lateral displacement separation method to maintain separation efficiency over a long period of time,” *Sep. Purif. Technol.*, vol. 172, pp. 258–267, 2017, doi: 10.1016/j.seppur.2016.08.023.
- [108] Z. Zhang, E. Henry, G. Gompper, and D. A. Fedosov, “Behavior of rigid and deformable particles in deterministic lateral displacement devices with different post shapes,” *J. Chem. Phys.*, vol. 143, no. 24, 2015, doi: 10.1063/1.4937171.

- [109] T. Dong *et al.*, “Integratable non-clogging microconcentrator based on counter-flow principle for continuous enrichment of CaSki cells sample,” *Microfluid. Nanofluidics*, vol. 10, no. 4, pp. 855–865, 2011, doi: 10.1007/s10404-010-0717-x.
- [110] B. K. Hønsvall, D. Altin, and L. J. Robertson, “Continuous harvesting of microalgae by new microfluidic technology for particle separation,” *Bioresour. Technol.*, vol. 200, pp. 360–365, 2016, doi: 10.1016/j.biortech.2015.10.046.
- [111] E. J. Mossige, A. Jensen, and M. M. Mielnik, “An experimental characterization of a tunable separation device,” *Microfluid. Nanofluidics*, vol. 20, no. 12, pp. 1–10, 2016, doi: 10.1007/s10404-016-1826-y.
- [112] E. J. Mossige, A. Jensen, and M. M. Mielnik, “Separation and Concentration without Clogging Using a High-Throughput Tunable Filter,” *Phys. Rev. Appl.*, vol. 9, no. 5, p. 54007, 2018, doi: 10.1103/PhysRevApplied.9.054007.
- [113] E. J. Mossige, B. Edvardsen, A. Jensen, and M. M. Mielnik, “A tunable, microfluidic filter for clog-free concentration and separation of complex algal cells,” *Microfluidics and Nanofluidics*, vol. 23, no. 4. 2019, doi: 10.1007/s10404-019-2209-y.
- [114] T. F. Didar and M. Tabrizian, “Adhesion based detection, sorting and enrichment of cells in microfluidic Lab-on-Chip devices,” *Lab Chip*, vol. 10, no. 22, pp. 3043–3053, 2010, doi: 10.1039/c0lc00130a.
- [115] C. H. Lee, S. Bose, K. J. van Vliet, J. M. Karp, and R. Karnik, “Studying cell rolling trajectories on asymmetric receptor patterns,” *J. Vis. Exp.*, no. 48, pp. 10–12, 2010, doi: 10.3791/2640.
- [116] S. Bose *et al.*, “Affinity flow fractionation of cells via transient interactions with asymmetric molecular patterns,” *Sci. Rep.*, vol. 3, pp. 1–8, 2013, doi: 10.1038/srep02329.
- [117] S. Choi, J. M. Karp, and R. Karnik, “Cell sorting by deterministic cell rolling,” *Lab Chip*, vol. 12, no. 8, pp. 1427–1430, 2012, doi: 10.1039/c2lc21225k.
- [118] R. Choi, Sungyoung; Levyc, Oren ; Mónica B. Coelho; M.S.Cabrald, Joaquim; Karp, Jeffrey M.; Karnik, “A cell rolling cytometer reveals the correlation between mesenchymal stem cell dynamic adhesion and differentiation state,” *Lab Chip*, 2014.
- [119] M. M. Baran, D. M. Allen, S. R. Russell, M. E. Scheetz, and J. F. Monthony, “Cell sorting using a universally applicable affinity chromatography matrix: Solid-phase anti-fluorescein isothiocyanate antibody,” *J. Immunol. Methods*, vol. 53, no. 3, pp. 321–334, Sep. 1982, doi: 10.1016/0022-1759(82)90179-X.
- [120] C. M. Hertz, D. J. Graves, D. A. Lauffenburger, and F. T. Serota, “Use of cell affinity chromatography for separation of lymphocyte subpopulations,” *Biotechnol. Bioeng.*, vol. 27, no. 5, pp. 603–612, 1985, doi: 10.1002/bit.260270509.
- [121] A. Kumar and A. Srivastava, “Cell separation using cryogel-based affinity chromatography,” *Nat. Protoc.*, vol. 5, no. 11, pp. 1737–1747, Oct. 2010, doi: 10.1038/nprot.2010.135.
- [122] X. Cheng *et al.*, “A microfluidic device for practical label-free CD4+ T cell counting of HIV-infected subjects,” *Lab Chip*, vol. 7, no. 2, pp. 170–178, 2007, doi: 10.1039/b612966h.
- [123] P. Li, Y. Gao, and D. Pappas, “Multiparameter cell affinity chromatography: Separation and analysis in a single microfluidic channel,” *Anal. Chem.*, vol. 84, no. 19, pp. 8140–8148, Oct. 2012, doi: 10.1021/ac302002a.

- [124] K. A. Hyun, T. Y. Lee, and H. Il Jung, "Negative enrichment of circulating tumor cells using a geometrically activated surface interaction chip," *Anal. Chem.*, vol. 85, no. 9, pp. 4439–4445, May 2013, doi: 10.1021/ac3037766.
- [125] G. Romeo, G. D'Avino, F. Greco, P. A. Netti, and P. L. Maffettone, "Viscoelastic flow-focusing in microchannels: Scaling properties of the particle radial distributions," *Lab Chip*, vol. 13, no. 14, pp. 2802–2807, 2013, doi: 10.1039/c3lc50257k.
- [126] K. Yoon, H. W. Jung, and M. S. Chun, "Secondary flow behavior of electrolytic viscous fluids with Bird-Carreau model in curved microchannels," *Rheol. Acta*, vol. 56, no. 11, pp. 915–926, Nov. 2017, doi: 10.1007/s00397-017-1033-0.
- [127] Y. Lu, S. Ahmed, F. Harari, and M. Vahter, "Impact of Ficoll density gradient centrifugation on major and trace element concentrations in erythrocytes and blood plasma," *J. Trace Elem. Med. Biol.*, vol. 29, pp. 249–254, Jan. 2015, doi: 10.1016/j.jtemb.2014.08.012.
- [128] A. Bøyum, "Separation of Blood Leucocytes, Granulocytes and Lymphocytes," *Tissue Antigens*, vol. 4, no. 3, pp. 269–274, May 1974, doi: 10.1111/j.1399-0039.1974.tb00252.x.
- [129] T. B. Casale and M. Kaliner, "A rapid method for isolation of human mononuclear cells free of significant platelet contamination," *J. Immunol. Methods*, vol. 55, no. 3, pp. 347–353, Dec. 1982, doi: 10.1016/0022-1759(82)90094-1.
- [130] C. OH, N. OH, O. CO, C. NHCO, C. OH, and O. CO, "PURIFICATION OF MONONUCLEAR CELLS, MONOCYTES AND POLYMORPHONUCLEAR LEUKOCYTES M I N I R E V I E W." Accessed: Jun. 15, 2021. [Online]. Available: [https://biolynx.ca/tech/articles/axs\\_cells.pdf](https://biolynx.ca/tech/articles/axs_cells.pdf).
- [131] D. Saraydin, E. Karadağ, Y. Işikver, N. Şahiner, and O. Güven, "The Influence of Preparation Methods on the Swelling and Network Properties of Acrylamide Hydrogels with Crosslinkers," *J. Macromol. Sci. - Pure Appl. Chem.*, vol. 41, no. 4, pp. 419–431, 2004, doi: 10.1081/MA-120028476.
- [132] W. Megone, N. Roohpour, and J. E. Gautrot, "Impact of surface adhesion and sample heterogeneity on the multiscale mechanical characterisation of soft biomaterials," *Sci. Rep.*, vol. 8, no. 1, Dec. 2018, doi: 10.1038/s41598-018-24671-x.
- [133] S. Girardo *et al.*, "Standardized microgel beads as elastic cell mechanical probes," *bioRxiv*, pp. 1–8, 2018, doi: 10.1101/290569.
- [134] O. Okay and S. Durmaz, "Charge density dependence of elastic modulus of strong polyelectrolyte hydrogels," Jan. 2002, doi: 10.81043/APERTA.95927.
- [135] D. Hariharan and N. A. Peppas, "Characterization, dynamic swelling behaviour and solute transport in cationic networks with applications to the development of swelling-controlled release systems," *Polymer (Guildf.)*, vol. 37, no. 1, pp. 149–161, Jan. 1996, doi: 10.1016/0032-3861(96)81610-7.
- [136] P. Jourdain *et al.*, "Simultaneous Optical Recording in Multiple Cells by Digital Holographic Microscopy of Chloride Current Associated to Activation of the Ligand-Gated Chloride Channel GABAA Receptor," *PLoS One*, vol. 7, no. 12, p. 51041, Dec. 2012, doi: 10.1371/journal.pone.0051041.
- [137] N. A. Peppas, P. Bures, W. Leobandung, and H. Ichikawa, "Hydrogels in pharmaceutical formulations," *European Journal of Pharmaceutics and Biopharmaceutics*, vol. 50, no. 1. Eur J Pharm Biopharm, pp. 27–46, Jul. 03, 2000,

- doi: 10.1016/S0939-6411(00)00090-4.
- [138] D. B. Agus *et al.*, “A physical sciences network characterization of non-tumorigenic and metastatic cells,” *Sci. Rep.*, vol. 3, no. 1, pp. 1–12, Apr. 2013, doi: 10.1038/srep01449.
- [139] R. Omidvar, M. Tafazzoli-shadpour, M. A. Shokrgozar, and M. Rostami, “Atomic force microscope-based single cell force spectroscopy of breast cancer cell lines: An approach for evaluating cellular invasion,” *J. Biomech.*, vol. 47, no. 13, pp. 3373–3379, Oct. 2014, doi: 10.1016/j.jbiomech.2014.08.002.
- [140] W. Xu, R. Mezencev, B. Kim, L. Wang, J. McDonald, and T. Sulchek, “Cell Stiffness Is a Biomarker of the Metastatic Potential of Ovarian Cancer Cells,” *PLoS One*, vol. 7, no. 10, 2012, doi: 10.1371/journal.pone.0046609.
- [141] S. O. Kim, J. Kim, T. Okajima, and N. J. Cho, “Mechanical properties of paraformaldehyde-treated individual cells investigated by atomic force microscopy and scanning ion conductance microscopy,” *Nano Converg.*, vol. 4, no. 1, p. 5, Dec. 2017, doi: 10.1186/s40580-017-0099-9.
- [142] M. Schürmann *et al.*, “Refractive index measurements of single, spherical cells using digital holographic microscopy,” *Methods Cell Biol.*, vol. 125, pp. 143–159, 2015, doi: 10.1016/bs.mcb.2014.10.016.
- [143] M. M. Villone, F. Greco, M. A. Hulsen, and P. L. Maffettone, “Numerical simulations of deformable particle lateral migration in tube flow of Newtonian and viscoelastic media,” *J. Nonnewton. Fluid Mech.*, vol. 234, pp. 105–113, 2016, doi: 10.1016/j.jnnfm.2016.05.006.
- [144] D. Yuan *et al.*, “Recent progress of particle migration in viscoelastic fluids,” *Lab Chip*, vol. 18, no. 4, pp. 551–567, 2018, doi: 10.1039/c7lc01076a.
- [145] H. Wei *et al.*, “Particle sorting using a porous membrane in a microfluidic device †,” *pubs.rsc.org*, doi: 10.1039/c0lc00121j.
- [146] H. M. Ji, V. Samper, Y. Chen, C. K. Heng, T. M. Lim, and L. Yobas, “Silicon-based microfilters for whole blood cell separation,” *Biomed. Microdevices*, vol. 10, no. 2, pp. 251–257, 2008, doi: 10.1007/s10544-007-9131-x.
- [147] K. Kwon, T. Sim, H.-S. Moon, J.-G. Lee, J. Chan Park, and H.-I. Jung, *A NOVEL PARTICLE SEPARATION METHOD USING MULTI-STAGE MULTI-ORIFICE FLOW FRACTIONATION (MS-MOFF)*. .
- [148] A. Mach, J. Kim, A. Arshi, S. Hur, D. D. C.-L. on a Chip, and undefined 2011, “Automated cellular sample preparation using a Centrifuge-on-a-Chip,” *pubs.rsc.org*, Accessed: Jun. 14, 2021. [Online]. Available: [https://pubs.rsc.org/en/content/articlehtml/2011/lc/c1lc20330d?casa\\_token=2w2\\_ff42yZQAAAAA:cwaJZ5-T0yTiqoi8Xun1m8lMYNtKrS-O97eqgX3a1pyxoIGveFw2WTzE0A-gKBjOoe\\_sz\\_Q33eRmk8E](https://pubs.rsc.org/en/content/articlehtml/2011/lc/c1lc20330d?casa_token=2w2_ff42yZQAAAAA:cwaJZ5-T0yTiqoi8Xun1m8lMYNtKrS-O97eqgX3a1pyxoIGveFw2WTzE0A-gKBjOoe_sz_Q33eRmk8E).
- [149] F. Del Giudice, “Viscoelastic focusing of polydisperse particle suspensions in a straight circular microchannel,” *Microfluid. Nanofluidics*, vol. 23, no. 7, p. 95, Jul. 2019, doi: 10.1007/s10404-019-2263-5.